Precambrian Research 377 (2022) 106676

Contents lists available at ScienceDirect

Precambrian Research

journal homepage: www.elsevier.com/locate/precamres

An authigenic response to Ediacaran surface oxidation: Remarkable micron-scale isotopic heterogeneity revealed by SIMS

Huan Cui [a,b,c,d,*], Kouki Kitajima [d], Ian J. Orland [d,e], Jean-Marc Baele [f], Shuhai Xiao [g], Alan J. Kaufman [h], Adam Denny [d,i], Michael J. Spicuzza [d], John H. Fournelle [d], John W. Valley [c,d]

[a] Equipe Géomicrobiologie, Institut de Physique du Globe de Paris (IPGP), Université Paris Cité, 75005 Paris, France
[b] Stable Isotope Laboratory, Department of Earth Sciences, University of Toronto, Toronto, ON M5S 3B1, Canada
[c] NASA Astrobiology Institute, University of Wisconsin–Madison, Madison, WI 53706, USA
[d] Department of Geoscience, University of Wisconsin–Madison, Madison, WI 53706, USA
[e] Wisconsin Geological and Natural History Survey, University of Wisconsin–Madison, Madison, WI 53705, USA
[f] Department of Geology, Faculty of Engineering, University of Mons, 7000 Mons, Belgium
[g] Department of Geosciences, Virginia Tech, Blacksburg, VA 24061, USA
[h] Department of Geology and Earth System Science Interdisciplinary Center, University of Maryland, College Park, MD 20742, USA
[i] Pacific Northwest National Laboratory, Richland, WA 99354, USA

ARTICLE INFO

Keywords:
Shuram excursion
Secondary ion mass spectrometry
Microbial sulfate reduction
Anaerobic oxidation of methane
Carbon isotopes
Authigenic carbonate
Deep-time carbon cycle

ABSTRACT

The Ediacaran Shuram excursion (SE) records a global decrease in carbonate carbon isotope ($\delta^{13}C_{carb}$) values from +6‰ down to ca. –10‰, representing the largest $\delta^{13}C_{carb}$ negative anomaly in Earth history. While the SE is widely recorded in the upper Doushantuo Formation of South China, it shows highly variable $\delta^{13}C_{carb}$ profiles among correlative sections. This inconsistent expression of the SE challenges the conventional view of a homogeneous marine dissolved inorganic carbon (DIC) reservoir. A potential process that could explain $\delta^{13}C_{carb}$ variability is local mineralization of isotopically distinct authigenic carbonates near the sediment–water interface during early diagenesis. However, a direct test of such authigenic carbonates is still limited. Here, following a recent study on the SE in an intra-shelf environment, we revisited an outer-shelf section, identified and analyzed μm-scale, *syn*-depositional authigenic calcite cements via integrated cathodoluminescence (CL), micro-X-ray fluorescence (μXRF), scanning electron microscope (SEM), energy-dispersive spectroscopy (EDS), and secondary ion mass spectrometry (SIMS). Our new SIMS results reveal remarkable micron-scale heterogeneity of $\delta^{13}C_{carb}$ in authigenic calcite cements, including extremely negative values down to –37.5‰ (VPDB). We interpret these calcite cements as methane-derived authigenic calcite (MDAC) resulting from microbial sulfate reduction (MSR) and anaerobic oxidation of methane (AOM) during early diagenesis. Based on the new results, we propose that the heterogeneous SE in South China — manifest on micrometer, centimeter, and basinal scales — was modulated by methane oxidation under variable local redox and water depth conditions. The SE, therefore, was coupled with different degrees of methane oxidation in individual basins, and globally triggered by enhanced seawater sulfate during an atmospheric oxygenation event. In light of this study, the potential role of redox variability in methane oxidation during the SE may have been underestimated. Our study demonstrates that integrated SIMS-SEM analysis can distinguish different generations of isotopically distinct carbonates otherwise undetected by conventional analysis, and is thus an effective approach to assess the origin and diagenetic history of $\delta^{13}C_{carb}$ anomalies in the sedimentary record.

Abbreviations: AOM, anaerobic oxidation of methane; BSE, backscattered electron; Cal, calcite; CL, cathodoluminescence; CAS, carbonate-associated sulfate; DIC, dissolved inorganic carbon; DOC, dissolved organic carbon; Dol, dolomite; DOUNCE, Doushantuo negative carbon isotope excursion; EDS, energy dispersive spectroscopy; EN, Ediacaran negative excursion; EP, Ediacaran positive excursion; EPMA, electron probe microanalysis; GS-IRMS, gas source-isotope ratio mass spectrometry; IMF, instrumental mass fractionation; MDAC, methane-derived authigenic calcite; MSR, microbial sulfate reduction; PPL, plane polarized light; Qz, quartz; ROI, region of interest; SE in text, Shuram excursion; SE in SEM images, secondary electron; SEM, scanning electron microscope; SIMS, secondary ion mass spectrometry; SWI, sediment–water interface; μXRF, micro-X-ray fluorescence; VCDT, Vienna Canyon Diablo Troilite; VPDB, Vienna Pee Dee Belemnite; XRD, X-ray diffraction.

* Corresponding author at: IPGP, Université Paris Cité, Paris, France.
E-mail address: Huan.Cui@ipgp.fr (H. Cui).

https://doi.org/10.1016/j.precamres.2022.106676
Received 15 May 2021; Received in revised form 4 March 2022; Accepted 5 April 2022
Available online 31 May 2022

1. Introduction

The Neoproterozoic Era (i.e., 1000 to ca. 539 million years ago) witnessed profound changes in the Earth-life system, including a prominent rise of complex multicellular eukaryotes (Butterfield, 2015; Xiao et al., 2016; Xiao and Narbonne, 2020; Tang et al., 2022) and dramatic fluctuation of carbonate carbon isotope compositions ($\delta^{13}C_{carb}$) (Kaufman et al., 1997; Halverson et al., 2005; Saltzman and Thomas, 2012). Notably, the Ediacaran Shuram Excursion (SE, Fig. 1A) — named after the Shuram Formation in Oman — shows $\delta^{13}C_{carb}$ values down to ca. –10‰ (VPDB) on a global scale, including Oman (Burns and Matter, 1993; Fike et al., 2006; Le Guerroué, 2006; Le Guerroué et al., 2006a; Le Guerroué et al., 2006b; Le Guerroué et al., 2006c; Grotzinger et al., 2011), South Australia (Calver, 2000; Husson et al., 2012; Husson et al., 2015), western USA (Kaufman et al., 2007; Bergmann et al., 2011; Bergmann et al., 2013b), northwestern Mexico (Loyd et al., 2012; Loyd et al., 2013), southeastern and central Siberia (Pokrovskii et al., 2006; Melezhik et al., 2009; Pokrovsky and Bujakaite, 2015; Pokrovsky et al., 2021), western Canada (Macdonald et al., 2013; Moynihan et al., 2019), southwestern Peru (Hodgin, 2020; Busch et al., 2022), and northern

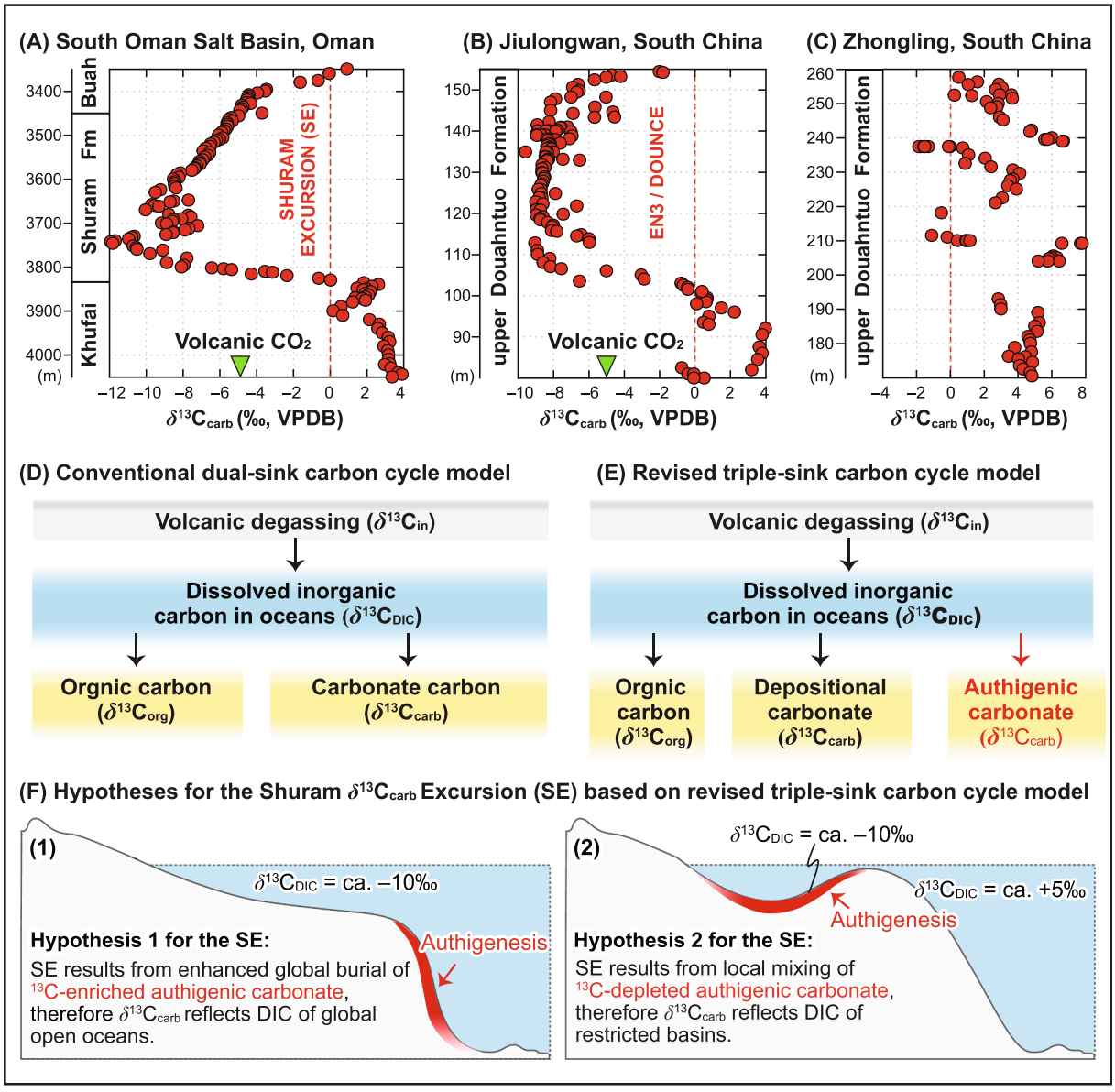

Fig. 1. Ediacaran Shuram $\delta^{13}C_{carb}$ excursion (SE), carbon cycle models, and predictable hypotheses for the SE. **(A)** SE in the Shuram Formation of Oman. Note that the $\delta^{13}C_{carb}$ values during the SE are significantly lower than the input value (i.e., $\delta^{13}C_{in} = -5‰$, shown as green triangle) from volcanic CO_2 degassing, which can hardly be explained by the conventional carbon cycle mode in steady state. Data source (Fike et al., 2006). **(B)** $\delta^{13}C_{carb}$ profile of the EN3/DOUNCE interval, upper Doushantuo Formation, Jiulongwan section, South China. Data source (Jiang et al., 2007; McFadden et al., 2008). **(C)** $\delta^{13}C_{carb}$ profile of the upper Doushantuo Formation, Zhongling section, South China. Data source (Cui et al., 2017). **(D)** Conventional carbon cycle model with one volcanic CO_2 source and dual carbon sinks. The two carbon sinks of dissolved inorganic carbon (DIC) in oceans are carbonate carbon and organic carbon. Details of this model can be found in published papers (Summons and Hayes, 1992; Kump and Arthur, 1999). **(E)** Revised carbon cycle model with authigenic carbonates as the third carbon sink. See section 2 and Schrag et al. (2013) for detailed description. **(F)** Two predictable hypotheses within the framework of the revised carbon cycle model. Hypothesis 1 proposes that the SE results from a global increase in the burial of ^{13}C-enriched authigenic carbonate, therefore representing DIC signals of global open oceans (Laakso and Schrag, 2020). Hypothesis 2 proposes that the SE results from local-scale mixing of ^{13}C-depleted authigenic carbonate, representing local DIC signals of individual sedimentary basins (Schrag et al., 2013). Red-colored zones represent region with active carbonate authigenesis near the sediment–water interface. See Section 2 for a detailed description. Abbreviations used: DOUNCE, Doushantuo negative carbon isotope excursion; DIC, dissolved inorganic carbon; EN, Ediacaran negative excursion; SE, Shuram excursion.

Table 1
A summary of SIMS spots during WiscSIMS session 2018–02-05. SIMS analyses were grouped in "domains" identified by SEM and CL imaging. The domains are numbered sequentially and referenced in both the appendix images and supplemental data table. All SIMS data are new in this study (Appendices 1, 2, 4). The samples were collected from the upper Doushantuo Formation, Zhongling section, South China. Detailed geological background of the samples can be found in Section 3.

SIMS mount	SIMS domain	SIMS spot ID	SEM-CL-SIMS results	μXRF panorama	SEM panorama	Lithology
12ZL-49.8a (Fig. 4B)	#1	@182–221	Fig. 9; Supplement 1	Fig. 4D	Fig. A1	Upper half: almost pure dolomicrite;
	#2	@226–265	Fig. 10; Supplement 1			Lower half: dolomicrite partially replaced or cemented by ^{13}C-depleted authigenic calcite and a trace amount of authigenic quartz
12ZL-49.8b (Fig. 4C)	#3	@498–527	Fig. 11; Supplement 2	Fig. 4E	Fig. A2	

India (Kaufman et al., 2006). Similar and perhaps time-equivalent negative $\delta^{13}C_{carb}$ excursions have also been widely reported from the upper Doushantuo Formation in South China (Fig. 1B, C)(Jiang et al., 2007; McFadden et al., 2008; Wang et al., 2012; Zhou et al., 2012; Lu et al., 2013; Zhu et al., 2013; Zhou et al., 2017; Gao et al., 2018; Lan et al., 2019; Wang et al., 2020; Cui et al., 2022; Li et al., 2022).

It is notable that published $\delta^{13}C_{carb}$ profiles of the SE in South China reveal highly variable patterns among correlative sections (Zhu et al., 2007b; Lu et al., 2013; Zhu et al., 2013; Cui et al., 2015; Wang et al., 2016; Li et al., 2017; Zhou et al., 2017; Gao et al., 2018; Lan et al., 2019; Wang et al., 2020; Li et al., 2022). The SE is most typical in the Yangtze Gorges area and is characterized by consistently negative $\delta^{13}C_{carb}$ values of ca. –9‰ (Fig. 1B), which is also commonly referred to as EN3 (Zhou and Xiao, 2007; McFadden et al., 2008; Zhou et al., 2012) or DOUNCE (Zhu et al., 2007a; Lu et al., 2013; Zhu et al., 2013) in the published literature. In contrast, the upper Doushantuo Formation at outer-shelf sections (Macouin et al., 2004; Ader et al., 2009; Kunimitsu et al., 2011; Cui et al., 2015; Furuyama et al., 2016; Cui et al., 2017) and slope sections (Wang et al., 2016; Li et al., 2017) show highly variable, albeit commonly negative, $\delta^{13}C_{carb}$ values. Given that the residence time (~100 kyr) of dissolved inorganic carbon (DIC) in the ocean is much longer than the seawater mixing time (Wallmann and Aloisi, 2012), shallow marine $\delta^{13}C_{DIC}$ is expected to be homogeneous across contemporaneous platforms. Therefore, the strong heterogeneity in SE-equivalent sections in South China presents a challenge to the conventional view that the SE carbonates record a homogeneous marine DIC reservoir.

One solution that can potentially explain this enigma postulates that isotopically distinct authigenic (i.e., formed in situ) carbonates, which are typically precipitated along the sediment–water interface (SWI) during *syn*-deposition and/or early diagenesis, may have played a significant role in causing the variable $\delta^{13}C_{carb}$ excursions in deep time (Schrag et al., 2013; Husson et al., 2015; Cui et al., 2017; Cao et al., 2020). Based on this hypothesis, progressive *syn*-deposition of isotopically distinct authigenic carbonate that formed around the SWI could lead to continuous expressions of $\delta^{13}C_{carb}$ excursion in stratigraphy; and various proportions of isotopically distinct authigenic carbonate may have caused the strong basin-scale heterogeneity in bulk $\delta^{13}C_{carb}$ values. In this study, two hypotheses that invoke authigenic carbonate have been evaluated, which are described in detail in Section 2.

It is important to recognize that most of the published studies on Neoproterozoic $\delta^{13}C_{carb}$ excursions in South China are based on analyses of either bulk or micro-drilled powders (e.g., Jiang et al., 2007; Zhou and Xiao, 2007; Zhu et al., 2007b; McFadden et al., 2008; Lu et al., 2013; Tahata et al., 2013; Zhu et al., 2013; Zhou et al., 2017). However, carbonate cements are typically tens to hundreds μm in size, which are considerably smaller than the micro-drill pits that are normally 800 μm or even larger in diameter. Therefore, the micro-drilling technique does not sufficiently separate different generations of carbonates. Consequently, the previously published $\delta^{13}C_{carb}$ data of micro-drilled powders likely reflect homogenized signals from multiple stages of carbonate precipitation. Studies that focus on carbonate cements of the SE on a micron scale remain limited (Bergmann et al., 2013a; Husson et al., 2020; Cui et al., 2021).

In recent years, in situ analysis of sedimentary carbonates by secondary ion mass spectrometer (SIMS) has emerged to be a powerful tool in unravelling detailed diagenetic histories and their corresponding $\delta^{13}C_{carb}$ signals of deep-time carbonate records (Bergmann et al., 2013a; Śliwiński et al., 2016b; Andrieu et al., 2017; Denny et al., 2017; Liu et al., 2017; Śliwiński et al., 2017; Cui et al., 2019; Denny et al., 2020; Husson et al., 2020; Xiao et al., 2020; Cui et al., 2021). Compared with traditional bulk-rock analysis, in situ analysis can offer texture-specific geochemical perspectives in detailed petrographic context and unprecedented spatial resolution. Following our recent SIMS investigation of the SE in the upper Doushantuo Formation at the intra-shelf Jiulongwan section (Fig. 1B) (Cui et al., 2021), here we expand our view towards the outer-shelf shoal environment by revisiting the upper Doushantuo Formation at Zhongling and Yangjiaping (Fig. 1C, 2, 3).

In this study, two samples from the upper Zhongling section were newly analyzed using integrated techniques, including optical microscopy, micro-X-ray fluorescence (μXRF), cathodoluminescence (CL), scanning electron microscopy (SEM), energy-dispersive spectroscopy (EDS), and secondary ion mass spectrometry (SIMS). These two samples (i.e., 12ZL-49.8a and 12ZL-49.8b; Figs. 4, A1, A2; Table 1) show abundant authigenic calcite cements that have previously been studied via micro-drilling techniques (Cui et al., 2017), and remain to be quantitatively characterized at a higher spatial resolution (i.e., micron scale). In this study, we investigated these authigenic calcite cements via multiple techniques and measured $\delta^{13}C_{carb}$ in situ. The main goals of this study are (1) to further investigate the SE at an outer-shelf region with μm-scale spatial resolution; (2) to compare the SIMS $\delta^{13}C_{carb}$ results between the intra-shelf Jiulongwan section and the outer-shelf shoal Zhongling section; (3) to formulate a unifying biogeochemical model for the variable SE in South China; and finally (4) to infer the origin of the SE on a global scale.

2. Motivation: Carbon cycle models and predictable hypotheses

In this study, we aim at testing the role of authigenic carbonate in ancient carbon cycles, particularly during the Ediacaran SE. The main hypotheses to be focused on have been proposed based on a revised carbon cycle model (Schrag et al., 2013; Laakso and Schrag, 2020), which postulates that authigenic carbonate may have played a previously overlooked — but potentially significant — role in deep-time carbon cycles. Before we introduce the hypotheses in detail, an overview of the traditional and the revised carbon cycle models is needed.

2.1. Traditional dual-sink carbon cycle model

Traditional carbon cycle model of the marine environment largely includes one source and two major sinks (Fig. 1D) (Summons and Hayes, 1992; Kump and Arthur, 1999). The source is mainly from volcanic CO_2 degassing and chemical weathering, which have an average input ($\delta^{13}C_{in}$) value of –5‰. The two sinks of dissolved inorganic carbon (DIC)

reservoir in the ocean are the burial of carbonate carbon and organic carbon, with the latter typically strongly depleted in ^{13}C mainly due to the fractionation induced by photosynthesis (Hayes, 1993; Hayes et al., 1999). Based on a simple mass balance view, the relationship between the source and sinks can be expressed as the following:

$$\delta^{13}C_{in} = \delta^{13}C_{carb}{*}f_{carb} + \delta^{13}C_{org}{*}f_{org} \quad (1)$$

where f_{org} and f_{carb} represent the proportional burial of carbonate carbon and organic carbon, respectively, and the sum of these two equals to one (i.e., $f_{carb} + f_{org} = 1$).

The offset (i.e., C isotope fractionation, ε_p) between carbonate carbon and organic carbon isotopes can be expressed as $\varepsilon_p = \delta^{13}C_{carb} - \delta^{13}C_{org}$. Thus, Eq. (1) can be rearranged with $\delta^{13}C_{carb}$ and $\delta^{13}C_{org}$ as the subject, respectively:

$$\delta^{13}C_{carb} = \delta^{13}C_{in} + \varepsilon_p{*}f_{org} \quad (2)$$

$$\delta^{13}C_{org} = \delta^{13}C_{carb} - \varepsilon_p \quad (3)$$

Based on the above equations, one can infer the fractional burial rate of organic carbon (f_{org}) for specific $\delta^{13}C_{carb}$ excursions, assuming that $\delta^{13}C_{in}$ and ε_p remain largely invariant. Within this framework, positive $\delta^{13}C_{carb}$ excursions have typically been interpreted as resulting from a higher rate of organic carbon burial, therefore representing an atmospheric oxygenation event (Broecker, 1970; Scholle and Arthur, 1980; Veizer et al., 1980; Knoll et al., 1986; Baker and Fallick, 1989; Kaufman et al., 1991; Des Marais et al., 1992; Karhu, 1993; Karhu and Holland, 1996; Kaufman et al., 1997; Shields, 1997; Shields et al., 1997; Cui et al., 2018); conversely, negative $\delta^{13}C_{carb}$ excursions have often been interpreted as resulting from a lower rate of organic carbon burial and/or enhanced oxidative weathering event (Kaufman et al., 2007; Kump et al., 2011).

However, this conventional carbon cycle model also faces major challenges in explaining many deep-time $\delta^{13}C_{carb}$ anomalies. For example, many negative $\delta^{13}C_{carb}$ excursions in Earth history show $\delta^{13}C_{carb}$ much lower than the canonical mantle value of –5‰, which can hardly be explained by the traditional carbon cycle model in steady state (Melezhik et al., 2005). In addition, the availability of oxidant budget for prolonged negative $\delta^{13}C_{carb}$ excursions also appears problematic (Bristow and Kennedy, 2008). When interpreting many positive $\delta^{13}C_{carb}$ excursions, corresponding geological evidence for the invoked extremely high rate of organic carbon burial is often lacking (Melezhik and Fallick, 1996; Cui et al., 2020b). Moreover, facies- and/or depth-dependent pattern and lateral gradient have also been reported from many positive (Giddings and Wallace, 2009; Bold et al., 2016; Cui et al., 2018; Hoffman and Lamothe, 2019; Rose et al., 2019; Bakakas Mayika et al., 2020; Jones et al., 2020; Prave et al., 2022) and negative $\delta^{13}C_{carb}$ excursions (Jiang et al., 2007; Ader et al., 2009; Busch et al., 2022), which can hardly be explained using the conventional carbon cycle model. These problems indicate that the conventional carbon cycle model bears major flaws when interpreting ancient $\delta^{13}C_{carb}$ anomalies.

2.2. Revised triple-sink carbon cycle model

Modified from the above dual-sink carbon cycle model (Fig. 1D), a revised model with authigenic carbonate as the third sink has been proposed (Fig. 1E) (Schrag et al., 2013). "Authigenic carbonate" refers to carbonate mineral that precipitated inorganically in situ within sediments; and "authigenesis" refers to the process whereby authigenic minerals form (Berner, 1981; Kastner, 1999; Glenn et al., 2000; McMurtry, 2009; Fantle et al., 2020).

It is important to recognize that the term "authigenic carbonate" per se does not bear any information about the timing of authigenesis; therefore, authigenic carbonate can refer to any carbonate that forms during *syn*-deposition, early diagenesis, or very late diagenesis, as long as this carbonate formed in situ. In studies of chemostratigraphy, evaluating the impact of post-depositional diagenesis is essential when investigating the credibility of measured $\delta^{13}C_{carb}$ values (Derry, 2010; Bristow et al., 2011; Črne et al., 2014; Higgins et al., 2018; Kreitsmann et al., 2019; Kreitsmann et al., 2020; Xiao et al., 2020; Zhao et al., 2020; Cui et al., 2021). Indeed, a tremendous amount of effort has been paid to evaluate the origin of carbonates with anomalous $\delta^{13}C_{carb}$ signals in this study (see Sections 3.5 and 3.6 for details). However, given that late diagenetic carbonate does not bear any link to contemporaneous marine carbon cycling, Schrag et al. (2013) and our study only focus on *early* authigenic carbonate that formed around the sediment–water interface when discussing the role of authigenesis in marine carbon cycles.

Authigenic carbonates in modern marine or lacustrine environments often show anomalous isotopic signatures. Both strongly positive (>10‰) and extremely negative (<–30‰) $\delta^{13}C_{carb}$ values have been reported from authigenic carbonates, which largely result from the occurrence of methanogenesis (leading to higher $\delta^{13}C_{carb}$) and methane oxidation (leading to lower $\delta^{13}C_{carb}$), respectively (Talbot and Kelts, 1986; Meister et al., 2007; Birgel et al., 2015; Pierre et al., 2016). Compared with ^{13}C-depleted authigenic carbonate, highly ^{13}C-enriched authigenic carbonate is less common due to the fact that methanogenesis does not produce alkalinity, and upward diffusion of methanogenic DIC is often balanced by ^{13}C-depleted methane-derived alkalinity.

In Schrag et al. (2013)'s revised carbon cycle model, the carbon sinks include carbonate carbon, organic carbon, and early authigenic carbonate that precipitated near the sediment–water interface (Fig. 1E). Based on a mass balance view, the relationship between source and sinks can be expressed as the following:

$$\delta^{13}C_{in} = (\delta^{13}C_{DIC} - \varepsilon_p)f_{org} + (1 - f_{org})[(\delta^{13}C_{DIC} - \varepsilon_{ac})f_{ac} + (\delta^{13}C_{DIC} - \varepsilon_{mc})(1 - f_{ac})] \quad (4)$$

or solving for $\delta^{13}C_{DIC}$ as:

$$\delta^{13}C_{DIC} = \delta^{13}C_{in} + f_{org}[\varepsilon_p - \varepsilon_{mc} - f_{ac}(\varepsilon_{ac} - \varepsilon_{mc})] + f_{ac}(\varepsilon_{ac} - \varepsilon_{mc}) \quad (5)$$

where $\delta^{13}C_{in}$ and $\delta^{13}C_{DIC}$ represent the carbon isotope composition of the carbon source and dissolved inorganic carbon (DIC), respectively; ε_p, ε_{ac} and ε_{mc} represent different $\delta^{13}C$ fractionation factors between seawater DIC and organic carbon (ε_p), authigenic carbonate (ε_{ac}) and normal marine carbonate (ε_{mc}), respectively; f_{org} and f_{ac} represent the burial proportion of carbon as organic carbon and authigenic carbonates, respectively.

By adding authigenic carbonate as the third carbon sink to the carbon cycle model (Fig. 1E), many deep-time $\delta^{13}C_{carb}$ excursions can then be re-interpreted as a secular change in the size of authigenic carbonate reservoir (Schrag et al., 2013). The revised model predicts that negative $\delta^{13}C_{carb}$ excursions could also be caused by enhanced burial of ^{13}C-enriched authigenic carbonate in global open-oceans, or local-scale mixing of ^{13}C-depleted authigenic carbonate; conversely, positive $\delta^{13}C_{carb}$ excursions could be caused by enhanced burial of ^{13}C-depleted authigenic carbonate in global open-oceans, or local-scale mixing of ^{13}C-enriched authigenic carbonate. This model has recently been evaluated for the middle Bambuí carbon cycle anomaly with a sustained $\delta^{13}C_{carb}$ plateau of ca. +15‰ (Cui et al., 2020b). Below we will introduce two published hypotheses that have invoked authigenic carbonate for the Ediacaran SE.

2.3. Predictable hypotheses based on revised carbon cycle model

In this study, we evaluate the potential role of authigenic carbonate during the SE by testing two hypotheses (Fig. 1F). These two hypotheses have been predicted based on the revised carbon cycle model with authigenic carbonate as a major sink in the ocean.

2.3.1. Hypothesis 1: Global authigenesis of ^{13}C-enriched carbonate

The first hypothesis invokes a large ^{13}C-enriched authigenic carbonate reservoir, and suggests that the SE results from a *global* increase

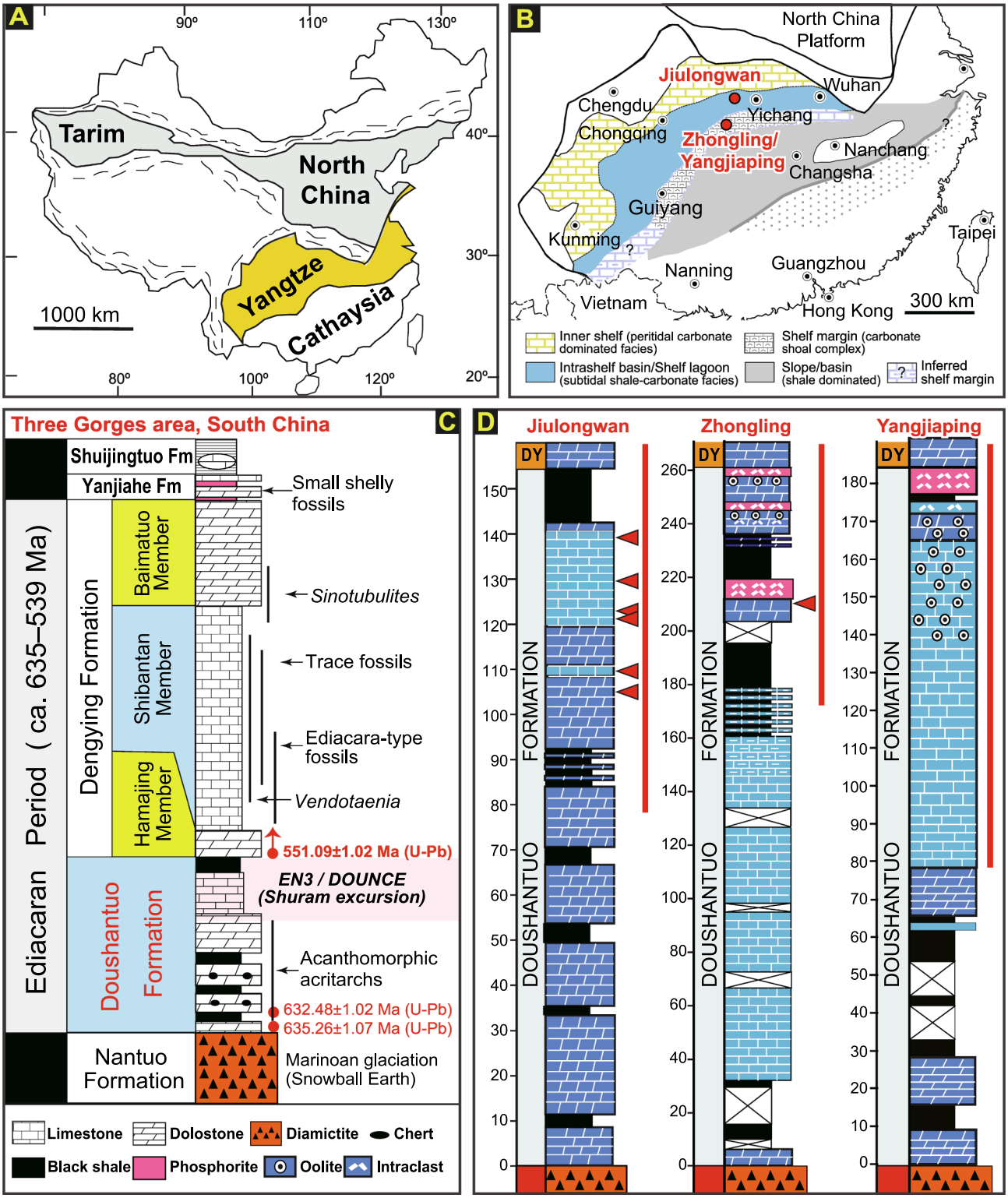

Fig. 2. Maps and stratigraphic columns. **(A)** Geological map of China, with the Yangtze Craton in yellow. **(B)** Reconstructed Ediacaran depositional environments on the Yangtze Craton (Jiang et al., 2011). Red dots indicate the locations of the Jiulongwan (intra-shelf) and Zhongling/Yangjiaping (outer-shelf shoal) sections. **(C)** Simplified litho-, bio-, and chrono-stratigraphy of the Ediacaran Doushantuo and Dengying formations in the Three Gorges area of South China. The SE is commonly referred to as EN3 (Zhou and Xiao, 2007; McFadden et al., 2008) or DOUNCE (Zhu et al., 2007a; Lu et al., 2013; Zhu et al., 2013) in South China. Thickness is not to scale. Note that the 551 Ma age was initially placed at the Doushantuo–Dengying boundary (Condon et al., 2005; Yang et al., 2021), but has also been re-assigned to the Shibantan Member of the Dengying Formation based on a chemostratigraphic study (An et al., 2015), and still remains a matter of debate (Zhou et al., 2017). Figure modified from Chen et al. (2013) and Cui et al. (2017). **(D)** Lithological columns of the Doushantuo Formation at the intra-shelf Jiulongwan section and the outer-shelf shoal Zhongling and Yangjiaping sections. Red triangles represent horizons analyzed by SIMS (Cui et al., 2021; this study). Red bars represent the intervals shown in Fig. 3. Radiometric ages from Condon et al. (2005) and Schmitz (2012). Abbreviations used: Cam, Cambrian; Cryo, Cryogenian; DOUNCE, Doushantuo negative carbon isotope excursion; DY, Dengying; NT, Nantuo.

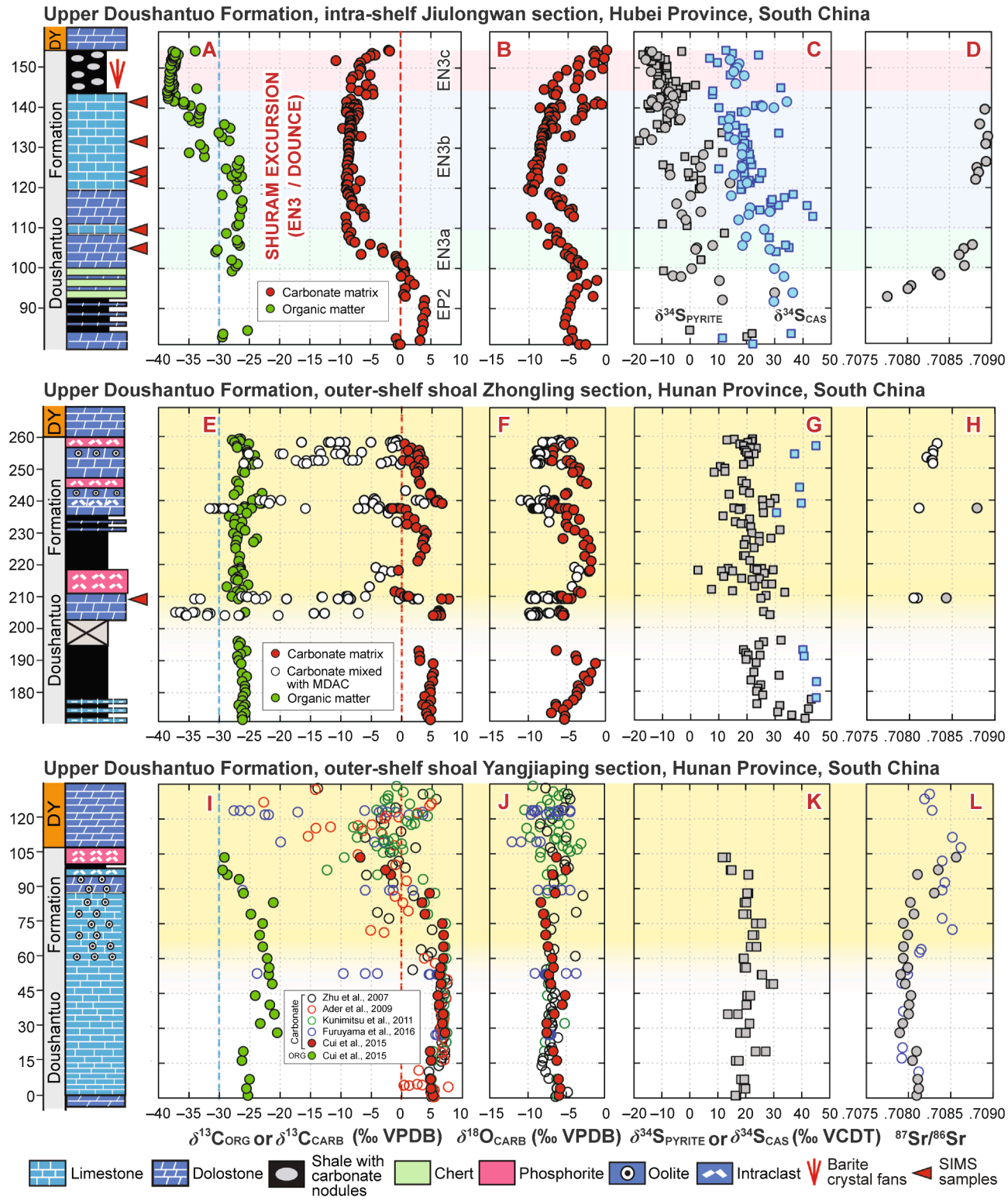

(caption on next page)

Fig. 3. Chemostratigraphic profiles of the upper Doushantuo Formation at the intra-shelf Jiulongwan section and the outer-shelf shoal Zhongling and Yangjiaping sections. All plotted data were measured by conventional gas-source isotope ratio mass spectrometer (GS-IRMS) based on micro-drilled powders (for $\delta^{13}C_{carb}$, $\delta^{18}O_{carb}$, and $^{87}Sr/^{86}Sr_{carb}$ analyses) or bulk powders (for $\delta^{13}C_{org}$ and $\delta^{34}S$ analyses). Red triangles alongside the lithological columns of the Jiulongwan and Zhongling sections represent the horizons investigated by SIMS (Cui et al., 2021; this study). Light green-, blue-, and red-shaded intervals of the Jiulongwan section represent EN3a, EN3b, and EN3c, respectively, which are defined by McFadden et al. (2008). The yellow-shaded intervals at Zhongling and Yangjiaping show highly negative $\delta^{13}C_{carb}$ in authigenic calcite, suggesting pulsed occurrence of methane oxidation. A thorough investigation has also been conducted for the lower 200 m of the Doushantuo Formation at the Zhongling section, but no methane-derived authigenic calcite (MDAC) was found. **(A, E, I)** Organic carbon isotope $\delta^{13}C_{org}$ (‰, VPDB, green filled circles) and carbonate carbon isotope $\delta^{13}C_{carb}$ (‰, VPDB) profiles. Vertical red and blue dash lines represent $\delta^{13}C$ of modern marine DIC and organic matter, respectively, with maximal fractionation of carbon isotopes by phytoplanktonic producers (Hayes et al., 1999; Kump and Arthur, 1999). **(B, F, J)** Carbonate oxygen isotope $\delta^{18}O_{carb}$ (‰, VPDB) profiles. **(C, G, K)** Pyrite sulfur isotope $\delta^{34}S_{pyrite}$ (‰, VCDT, gray color) and sulfate sulfur isotope $\delta^{34}S_{CAS}$ (‰, VCDT, cyan color) profiles. **(D, H, L)** Strontium isotope $^{87}Sr/^{86}Sr$ profiles of carbonates. White circles in **E, F,** and **H** represent micro-drilled authigenic calcite or micro-drilled dolomite matrix with various amounts of authigenic calcite cements. Data sources: Jiulongwan $\delta^{13}C_{carb}$, $\delta^{18}O_{carb}$, $\delta^{13}C_{org}$ (McFadden et al., 2008); Jiulongwan $\delta^{34}S$ shown as squares (McFadden et al., 2008); Jiulongwan $\delta^{34}S$ shown as circles (Shi et al., 2018); Jiulongwan $^{87}Sr/^{86}Sr$ (Sawaki et al., 2010); All Zhongling data (Cui et al., 2017) except for the $\delta^{34}S_{CAS}$ data (Li et al., 2010); Yangjiaping data shown as filled circles and squares (Cui et al., 2015); Yangjiaping data shown as empty circles (Zhu et al., 2007b; Ader et al., 2009; Kunimitsu et al., 2011; Furuyama et al., 2016). Abbreviations: CAS, carbonate-associated sulfate; DY, Dengying; EN, Ediacaran negative excursion; EP, Ediacaran positive excursion; GS-IRMS, gas-source isotope ratio mass spectrometer; MDAC, methane-derived authigenic calcite; VCDT, Vienna Canyon Diablo Troilite; VPDB, Vienna Pee Dee Belemnite.

in the burial of ^{13}C-enriched authigenic carbonate. In this scenario, enhanced burial of ^{13}C-enriched authigenic carbonate can drive the $\delta^{13}C_{DIC}$ of platform environment towards much lower values; authigenesis of this ^{13}C-enriched reservoir may occur in global open oceans during a period with enhanced methanogenesis (Laakso and Schrag, 2020). The potential trigger for this hypothesized large-scale methanogenic event — as well as the consequent mineralization of ^{13}C-enriched authigenic carbonate — has been proposed to be a global drawdown of seawater sulfate during the SE (Laakso and Schrag, 2020). Based on this hypothesis, SE sections record the compensating DIC of global open oceans with significantly ^{13}C-depleted signals, while correlative sections that show less negative $\delta^{13}C_{carb}$ values may result from different proportions of mixing between ^{13}C-depleted depositional carbonate and ^{13}C-enriched authigenic carbonate (Laakso and Schrag, 2020).

Notably, this hypothesis predicts the occurrence of ^{13}C-enriched authigenic carbonate cement in SE-correlative sections that show less negative $\delta^{13}C_{carb}$ values. If true, SIMS $\delta^{13}C_{carb}$ analysis of different generations of carbonates should be able to identify those hypothesized ^{13}C-enriched authigenic carbonate cements. In this regard, the upper Doushantuo Formation at the Zhongling section is an ideal target, which shows bulk $\delta^{13}C_{carb}$ of mostly positive values, with only very few mildly negative values down to –2‰ in depositional carbonate (Fig. 1C) (Li et al., 2010; Cui et al., 2015); the $\delta^{13}C_{carb}$ profile of the Zhongling section is in contrast with the typical SE (with $\delta^{13}C_{carb}$ consistently around –9‰) that is recorded in the upper Doushantuo Formation at Jiulongwan (Fig. 3) (Jiang et al., 2007; McFadden et al., 2008; Zhu et al., 2013). In this study, we actively searched for the hypothesized ^{13}C-enriched authigenic carbonate in the upper Doushantuo Formation at Zhongling.

2.3.2. *Hypothesis 2: Local authigenesis of ^{13}C-depleted carbonate*

An alternative hypothesis that invokes authigenic carbonate proposes that the SE may result from *local* authigenesis of ^{13}C-depleted authigenic carbonate, therefore representing local carbon cycle anomaly of individual sedimentary basins (Schrag et al., 2013; Fantle et al., 2020). Based on this hypothesis, the DIC of global open oceans may maintain normal $\delta^{13}C_{DIC}$ signals around 0‰ or slightly positive values, while disparate basins may preserve variable and much lower $\delta^{13}C_{carb}$ signals due to different proportions of mixing between depositional carbonate and ^{13}C-depleted authigenic carbonate. The trigger for local-scale authigenesis has been proposed to be a marine transgression, which can effectively add authigenic carbonate to marine carbonate precipitated from the water column (Schrag et al., 2013). Indeed, methane-derived authigenic calcite (MDAC) nodules with strong ^{13}C depletion (down to –37.2‰) have been reported from South China and are linked to the SE (Cui et al., 2016; Cui et al., 2017). In addition, negative $\delta^{13}C_{carb}$ excursions that were measured from authigenic carbonate within clastic rocks have also been claimed to be correlative with the SE (Canfield et al., 2020; Zhang et al., 2022), although the veracity of these $\delta^{13}C_{carb}$ excursions still requires further constraints.

This hypothesis can be tested by searching for ^{13}C-depleted authigenic carbonate in SE sections. However, challenges remain on how to distinguish authigenic carbonate from depositional carbonate on a micron scale. Authigenic carbonate that formed around the sediment–water interface may preserve the original fabrics on a micron scale, making them difficult to be identified. So far, no convincing evidence for the hypothesized mixing of ^{13}C-depleted authigenic carbonate has been found on a micron scale within the SE. Published SIMS studies of the SE-equivalent Wonoka Formation and the EN3/DOUNCE interval of the upper Doushantuo Formation at Jiulongwan do not show extremely negative $\delta^{13}C_{carb}$ values (<–12‰) that can clearly be interpreted as the occurrence of authigenesis; instead, most of the analyzed SIMS $\delta^{13}C_{carb}$ values clustered around the typical Shuram bulk value of ca. –10‰, though the SIMS data often show a larger variability compared with $\delta^{13}C_{carb}$ values analyzed on micro-drilled powers (Husson et al., 2020; Cui et al., 2021).

In this study, we expand our SIMS investigation of the upper Doushantuo Formation from the intra-shelf Jiulongwan section to the outer-shelf shoal Zhongling section. Previous studies reveal that the upper Doushantuo Formation in the outer-shelf region is rich in authigenic calcite nodules on a centimeter scale (Cui et al., 2021; Cui et al., 2022). It is possible that isotopically distinct authigenic carbonate cements exist on a micron scale in this region. We aim to test this hypothesis by identifying and analyzing authigenic carbonate cements by SIMS in this study.

3. Background of the Doushantuo Formation

3.1. *Geological background*

3.1.1. *Stratigraphy, geochronology, and paleogeography*

The Ediacaran Doushantuo Formation in the Yangtze block of South China overlies the Nantuo diamictite and begins with a ca. 635 Ma Marinoan cap carbonate (Fig. 2) (Condon et al., 2005; Jiang et al., 2011). Stratigraphically above the Doushantuo Formation is the dolostone-dominated Dengying Formation. The age of the Doushantuo–Dengying boundary has been constrained to be ca. 551 Ma (Condon et al., 2005; Yang et al., 2021), but was also suggested to be slightly older based on an alternative stratigraphic correlation mode (An et al., 2015; see Zhou et al., 2017 for a different view).

The available age constraints for the SE are largely based on U-Pb dating of volcanic zircons (Condon et al., 2005; Yang et al., 2021), Re-Os dating of interbedded shales (Rooney et al., 2020; Yang et al., 2021), and astrochronologic calibrations (Gong et al., 2017; Minguez and Kodama, 2017; Gong and Li, 2020; Li et al., 2022). Notably, a recent Re-Os study reveals that the SE was deposited between 574.0 ± 4.7 and 567.3 ± 3.0 Ma (Rooney et al., 2020). The duration of the SE has been estimated to be ca. 20 Myr (Sui et al., 2019), ca. 9.1 ± 1.0 Myr (Gong et al., 2017), ca. 8 Myr (Minguez and Kodama, 2017), ca. 7.7 ± 0.2 Myr

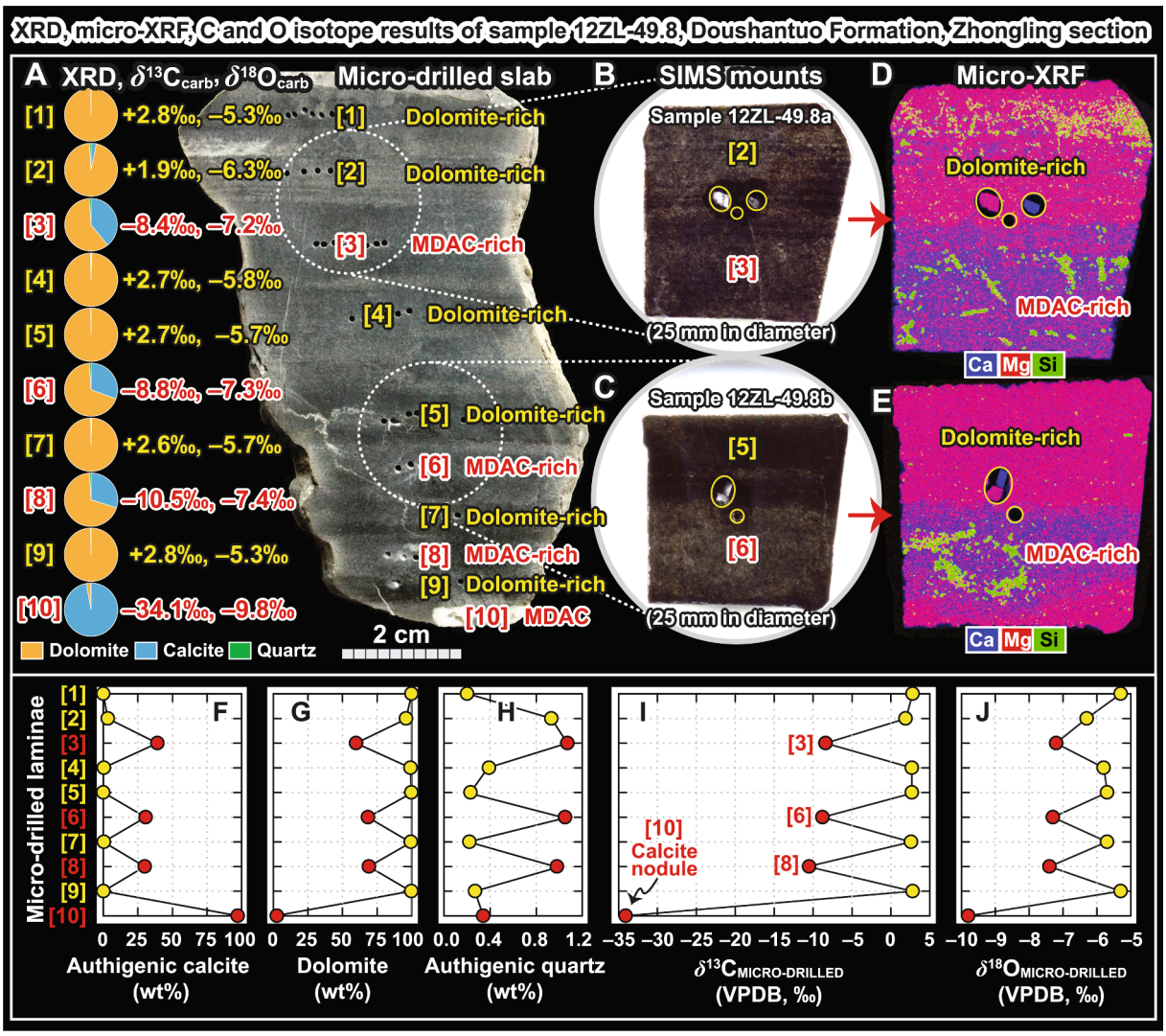

Fig. 4. Laminated dolostone sample 12ZL-49.8 investigated in this study by integrated SEM-EDS-CL-μXRF-SIMS. This sample was collected from the upper Doushantuo Formation (209.2 m in height) at the outer-shelf shoal Zhongling section, Hunan Province, South China. **(A)** Photograph of the analyzed sample (12ZL-49.8). Yellow (indicating dolomite-rich) and red (indicating authigenic-calcite-rich) numbers [1] to [10] represent ten micro-drilled laminae. The micro-drilling holes are ca. 800 μm in diameter. $\delta^{13}C_{carb}$ and $\delta^{18}O_{carb}$ data of micro-drilled powders were analyzed by conventional GS-IRMS. Pie chart shows different proportions of calcite (blue), dolomite (orange), and quartz (green) for each sample based on XRD data of micro-drilled powders from each lamina. Note the remarkable heterogeneity of $\delta^{13}C_{carb}$ in alternating laminae and the extremely negative $\delta^{13}C_{carb}$ value of –34.1‰ from a small, white-colored authigenic calcite nodule at the bottom of this slab. **(B, C)** SIMS epoxy mounts investigated in this study. Each SIMS mount is 25 mm in diameter, with three WiscSIMS standards (calcite UWC3, dolomite UW6220, and pyrite UWPy1) mounted in the center (marked by yellow circles). Panorama views of these two SIMS mounts under BSE can be found in Figs. A1 and A2, respectively. **(D, E)** Elemental maps of Ca (blue), Mg (red), and Si (green) generated by μXRF. Note that the upper half of the SIMS mount is dominated by dolomite, and shows positive $\delta^{13}C_{carb}$ values based on the measurement of micro-drilled powders; whereas the lower half of each SIMS epoxy mount is rich in ^{13}C-depleted methane-derived authigenic calcite (MDAC) cements and a trace amount of authigenic quartz cements. **(F–H)** XRD results of the ten micro-drilled laminae of slab 12ZL-49.8. **(I–J)** $\delta^{13}C_{carb}$ and $\delta^{18}O_{carb}$ data of the ten micro-drilled laminae of slab 12ZL-49.8. Data source: GS-IRMS and XRD data (Cui et al., 2017); SIMS epoxy mounts and μXRF results (this study). Abbreviations: MDAC, methane-derived authigenic calcite; XRD, X-ray diffraction; μXRF, micro-X-ray fluorescence.

(Gong and Li, 2020), or ca. 6.1 ± 0.2 Myr (Li et al., 2022) based on different astrochronologic calculations. The termination age of the SE was initially proposed to be ca. 551 Ma (Condon et al., 2005), but was later revised to be 562.5 ± 1.1 Ma (Canfield et al., 2020) or 567.3 ± 3.0 Ma (Rooney et al., 2020; Yang et al., 2021).

Deposition of the Doushantuo Formation has been broadly divided into two stages: an open ramp shelf followed by a rimmed shelf protecting an intra-shelf basin (Jiang et al., 2011; Cui et al., 2015). In addition, two depositional mega-sequences with multiple sub-stages of deposition have also been proposed for the Doushantuo Formation (Zhu et al., 2007b; Zhu et al., 2013; Zhu et al., 2022). Stratigraphic data and paleogeographic reconstructions indicate an increase in water depth from proximal intertidal environments in the northwest to distal deep basinal settings in the southeast. Three platform facies belts have been proposed, including a proximal inner shelf dominated by peritidal carbonates, an intra-shelf basin containing mixed carbonates and shales, and an outer-shelf shoal complex consisting of carbonates and phosphorites (Fig. 2) (Jiang et al., 2011).

3.1.2. *Sedimentology of outer-shelf sections*

In the field, the upper 50 m of the Doushantuo Formation at Zhongling and Yangjiaping is mainly composed of intraclastic, oolitic, or fine-grained carbonate facies associated with discrete levels of phosphorite, suggesting deposition in an outer-shelf carbonate shoal environment (Jiang et al., 2011; Cui et al., 2015; Cui et al., 2016; Cui et al., 2017). Based on the occurrence of phosphatic allochems and oolite, the bedded fine-grained dolostone and phosphorite likely formed in well agitated seawater, and was then dolomitized in the outer-shelf environment

during very early diagenesis (Cui et al., 2016; Cui et al., 2017).

The Doushantuo dolostones are often fine grained, indicating a primary or early diagenetic origin. Indeed, earlier studies suggest that the composition of Precambrian ocean may be very different from the Phanerozoic ones and can facilitate the precipitation of primary dolomite (Tucker, 1982; Hood and Wallace, 2012; Hood et al., 2015; Hood and Wallace, 2018). Notably, largely based on a clumped isotope study, dolostones of the Doushantuo Formation at the inner shelf Zhangcunping section have been interpreted to result from *syn*-depositional (i.e., early diagenetic) dolomitization near the sediment–water interface (Chang et al., 2020).

A striking feature of the upper Doushantuo Formation at Zhongling and Yangjiaping is the occurrence of ^{13}C-depleted MDAC nodules and cements (Macouin et al., 2004; Ader et al., 2009; Kunimitsu et al., 2011; Cui et al., 2016; Furuyama et al., 2016; Cui et al., 2017; Cui et al., 2022). Extremely negative $\delta^{13}C_{carb}$ values down to ca. –37.2‰ (VPDB) have been found in these nodules (Fig. 3E, 3I), suggesting a significant contribution from the oxidation of biogenic methane (Cui et al., 2017). These MDACs have been interpreted to have formed during early diagenesis in shallow marine sediments (Macouin et al., 2004; Ader et al., 2009; Macouin et al., 2012; Cui et al., 2016; Furuyama et al., 2016; Cui et al., 2017; Cui et al., 2022).

Late calcite veins have also been found at the Zhongling section, but they typically crosscut the primary sedimentary bedding and show moderate and variable $\delta^{13}C_{carb}$ values (ranging from ca. –5 to +6‰) (Cui et al., 2017). Therefore, we rule out any causal link — both isotopically and petrographically — between these late calcite veins and the ^{13}C-depleted authigenic calcite (Cui et al., 2017). In addition, no mineralogical evidence for metamorphic alteration or massive recrystallization has been observed in the field or in thin sections, precluding the possibility that the outer-shelf shoal sections have been significantly affected by late hydrothermal activity. Detailed evaluation about the origin of these authigenic calcites can be found in Section 3.6.

3.2. Chemostratigraphy of the Doushantuo Formation

Based on conventional analyses of micro-drilled or crushed bulk powders, detailed chemostratigraphic profiles have been published for the Doushantuo Formation at both intra-shelf sections (Jiang et al., 2007; McFadden et al., 2008; Li et al., 2010; Sawaki et al., 2010; Zhou et al., 2012; Ling et al., 2013; Tahata et al., 2013; Shi et al., 2018; Lan et al., 2019) and outer-shelf sections (Macouin et al., 2004; Zhu et al., 2007b; Ader et al., 2009; Li et al., 2010; Kunimitsu et al., 2011; Furuyama et al., 2016; Cui et al., 2017) (e.g., Fig. 3). The sampling holes induced by micro-drilling are typically ca. 800 μm in diameter and ca. 2000 μm in depth (Cui et al., 2015; Cui et al., 2017). Before we present the more detailed SIMS results, an overview of the published chemostratigraphic results of the Doushantuo Formation is necessary. Here, we briefly summarize the main chemostratigraphic features below.

3.2.1. $\delta^{13}C_{carb}$ chemostratigraphy based on micro-drilled carbonates

The $\delta^{13}C_{carb}$ profile of the Doushantuo outcrops at Jiulongwan shows three notable Ediacaran Negative (EN) excursions: EN1 in the basal cap carbonate, EN2 in the middle section, and EN3/DOUNCE at the top (Jiang et al., 2007; McFadden et al., 2008; Li et al., 2010), although recent studies based on drill cores or outcrops also reveal more nuanced variations (Tahata et al., 2013; Zhu et al., 2013; Zhou et al., 2017; Chen et al., 2022). The EN3/DOUNCE interval in the Yangtze Gorges area typically shows a sudden decrease of $\delta^{13}C_{carb}$ from +5‰ down to –9‰ (VPDB) within 20 m, and then the $\delta^{13}C_{carb}$ values remain as low as –9‰ stratigraphically upward for around 40 m before recovering back to positive values (Fig. 3A) (Jiang et al., 2007; Zhou et al., 2012; Ling et al., 2013; Lu et al., 2013; Tahata et al., 2013). This profound $\delta^{13}C_{carb}$ negative excursion has been correlated with the SE on a global scale (Jiang et al., 2007; McFadden et al., 2008; Yang et al., 2021).

The $\delta^{13}C_{carb}$ profiles of carbonate matrix in the upper Doushantuo Formation at Zhongling and Yangjiaping show scattered and only a few moderately negative data points (ranging from +7 to −7‰) in the upper 60 m (gray filled circles in Fig. 3E, 3I). However, white-colored authigenic calcite nodules and cements in the upper part of these two sections preserve remarkably negative $\delta^{13}C_{microdrilled\ carbonates}$ values down to ca. –37.2‰ (Fig. 3E; Fig. 3I) (Macouin et al., 2004; Zhu et al., 2007b; Ader et al., 2009; Macouin et al., 2012; Cui et al., 2016; Furuyama et al., 2016; Cui et al., 2017). Viewed together, the carbonate matrix and the authigenic calcite show a much wider range of $\delta^{13}C_{carb}$ in the upper Doushantuo Formation at these two outer-shelf shoal sections (Fig. 3E, 3I).

3.2.2. $\delta^{13}C_{org}$ chemostratigraphy based on bulk acidified powders

The $\delta^{13}C_{org}$ profiles of the upper Doushantuo Formation at intra-shelf and outer-shelf shoal sections show three main features. First, the EN3/DOUNCE interval at Jiulongwan shows a strong decoupling between paired $\delta^{13}C_{carb}$ and $\delta^{13}C_{org}$ (Fig. 3A). Second, the uppermost 10 m of the EN3 interval (i.e., Member IV shale in McFadden et al., 2008) show highly negative $\delta^{13}C_{org}$ values approaching −40‰ (Fig. 3A), which suggests recycling of methane in deeper environment. Third, the $\delta^{13}C_{org}$ profile of the Zhongling section show relatively steady values between −25‰ and −30‰, although the corresponding $\delta^{13}C_{carb}$ of carbonate matrix show slightly larger variations (Fig. 3E). Notably, paired $\delta^{13}C_{carb}$ and $\delta^{13}C_{org}$ at Yangjiaping show a broad co-variation (Fig. 3I), which is similar to the published $\delta^{13}C_{carb}$ and $\delta^{13}C_{org}$ profiles at the inner-shelf Wangji section (Gao et al., 2019).

3.2.3. $\delta^{18}O_{carb}$ chemostratigraphy based on micro-drilled carbonates

The $\delta^{18}O_{carb}$ profile of the EN3/DOUNCE interval at Jiulongwan shows an overall negative excursion down to −10‰ (Fig. 3B), which broadly co-varies with the $\delta^{13}C_{carb}$ profile (Fig. 3A). The $\delta^{18}O_{carb}$ profiles at Zhongling and Yangjiaping show variations between −2 to −9‰, with authigenic calcites typically having more negative (−9‰) $\delta^{18}O_{carb}$ values than the carbonate matrix (Fig. 3F, 3J).

Notably, published SE profiles on a global scale generally show tight correlations between $\delta^{13}C_{carb}$ and $\delta^{18}O_{carb}$ (Derry, 2010; Grotzinger et al., 2011). Multiple mechanisms have been proposed to explain this phenomenon, including meteoric water and mixing zone diagenesis (Knauth and Kennedy, 2009; Zhao et al., 2020), burial diagenesis (Derry, 2010), primary paleoclimatic change that involves global warming and glacial melt during deposition (Bjerrum and Canfield, 2011), early authigenesis in shallow marine sediments (Cui et al., 2017), and mixing of recycled carbonatite volcanic ash formed by the melting of sedimentary carbonates (Liu et al., 2021). Very often, interpretations of the SE closely hinge on how one interprets the $\delta^{13}C_{carb}$ and $\delta^{18}O_{carb}$ correlation (Knauth and Kennedy, 2009; Derry, 2010). However, there is still no consensus on this issue.

3.2.4. $\delta^{34}S$ chemostratigraphy based on bulk powder

Sulfur isotope data measured from the Jiulongwan EN3/DOUNCE interval show a progressive decrease from ca. +30 to +10‰ in carbonate-associated sulfate ($\delta^{34}S_{CAS}$) (Fig. 3C) (McFadden et al., 2008; Li et al., 2010; Shi et al., 2018). At the same time, pyrite S isotope ($\delta^{34}S_{pyrite}$) data in the EN3/DOUNCE interval at Jiulongwan show a parallel decrease from ca. 0 to –20‰ (Fig. 3C) (McFadden et al., 2008; Li et al., 2010; Shi et al., 2018). The coupled decreases in $\delta^{34}S_{pyrite}$ and $\delta^{34}S_{CAS}$ have been taken as evidence for increasing sulfate concentrations during EN3/DOUNCE (McFadden et al., 2008; Li et al., 2010; Shi et al., 2018). It has been proposed that a stratified ocean with a dynamic euxinic wedge was maintained on an open shelf represented by the Jiulongwan section (Li et al., 2010), but more recent studies suggest that this putative euxinic water mass was confined to an intra-shelf lagoonal basin (Xiao et al., 2012; Cui et al., 2015). In addition, sulfate concentrations in outer-shelf shoal region have been suggested to be depleted in seawater (Li et al., 2010; Li et al., 2017; Shi et al., 2018). However, the finding of chicken wire texture that is indicative of *syn*-depositional

precipitation of gypsum suggests that seawater sulfate concentration may be locally higher than previously thought (Cui et al., 2022).

The $\delta^{34}S_{pyrite}$ profiles of the upper Doushantuo Formation at Zhongling and Yangjiaping show exclusively positive values of around +20‰ (Fig. 3G) (Li et al., 2010; Cui et al., 2015; Cui et al., 2017). The $\delta^{34}S_{CAS}$ data in the upper Zhongling section show consistent values at ca. +40‰ (Li et al., 2010). Compared with the Jiulongwan section, lower $\delta^{34}S_{pyrite}$ and $\delta^{34}S_{CAS}$ data that are seen in the EN3/DOUNCE interval at Jiulongwan (Fig. 3C) are missing at Zhongling and Yangjiaping (Fig. 3G, 3K). This has been interpreted as either a sulfate gradient in the ocean (Li et al., 2010; Li et al., 2017) or a potential stratigraphic truncation or non-deposition near the top of the Doushantuo Formation in outer-shelf regions (Cui et al., 2015).

3.2.5. $^{87}Sr/^{86}Sr$ chemostratigraphy based on micro-drilled carbonates

The $^{87}Sr/^{86}Sr$ profile of the Jiulongwan section shows a notable rise from ca. 0.7080 to 0.7090 in the EN3/DOUNCE interval (Fig. 3D), suggesting enhanced chemical weathering during the SE. Similar increases in $^{87}Sr/^{86}Sr$ have also been reported from other SE-equivalent strata worldwide (Burns et al., 1994; Calver, 2000; Le Guerroué et al., 2006c; Melezhik et al., 2009; Cui et al., 2015; Cui et al., 2020a).

The $^{87}Sr/^{86}Sr$ profile of the upper Doushantuo Formation at Zhongling was mainly measured from calcite phases of MDAC nodules and cements, which show a slight increase from 0.7080 to 0.7083 in the upper 50 m (Fig. 3H) (Cui et al., 2017). The $^{87}Sr/^{86}Sr$ profile of the upper Yangjiaping section shows a similar increase from 0.7080 to 0.7085 (Fig. 3L). Compared with the Jiulongwan section (Fig. 3D), the lack of more radiogenic $^{87}Sr/^{86}Sr$ values of ca. 0.7090 at the Zhongling and Yangjiaping sections (Fig. 3H, 3L) has been interpreted to result from a potential stratigraphic incompleteness in the shallow shelf environment (Cui et al., 2015).

3.3. Redox constraints

Published studies of the Doushantuo Formation reveals heterogeneous redox conditions across the basin. Fe speciation results of the Jiulongwan section suggest that the EN3/DOUNCE interval was deposited in an overall anoxic intra-shelf environment with intermitted euxinic episodes and increasing sulfide availability (see Fig. S6 in Li et al., 2010). These inferred anoxic/euxinic redox conditions for the EN3/DOUNCE interval at Jiulongwan are also consistent with published cerium anomalies (Ce/Ce*) in carbonates, which show a progressive increase from ca. 0.3 to ca. 0.8 across EN3/DOUNCE and have been interpreted to reflect increasingly reducing redox conditions (Zhou et al., 2012; Wei et al., 2018; see also a different view in Liu et al., 2021).

Compared with the extensively studied Jiulongwan section, geochemical data indicative of redox conditions at the Zhongling section are limited. Nevertheless, sedimentological results of the Zhongling and nearby Yangjiaping sections show abundant carbonate intraclasts, oolite, and phosphorite intraclasts in the upper part of the Doushantuo Formation (Jiang et al., 2011; Kunimitsu et al., 2011; Cui et al., 2017), suggesting an overall shallow, dynamic, and probably well oxygenated depositional environment during carbonate and phosphorite deposition. In contrast, few intraclasts, ooids, or cross-stratified beds are known in the upper Doushantuo Formation at Jiulongwan (Jiang et al., 2007; McFadden et al., 2008). Therefore, sedimentological results of the upper Zhongling section suggest an overall shallower and more oxygenated environment during deposition than the upper Jiulongwan section.

On a global scale, U isotope ($\delta^{238}U$) data of the SE suggest an extensive oceanic oxygenation event. Profiles of the SE at the Jiulongwan section of South China, the Bol'shoy Patom section of Siberia, the Death Valley succession of the southwestern United States, and the Sonora Succession in northwestern Mexico, all reveal significant positive shifts from ca. −0.73‰ to ca. −0.27‰, which have been interpreted as a major oceanic oxygenation event (Zhang et al., 2019; Li et al., 2020). It should be noted that this inferred global oceanic oxygenation event during the SE does not necessarily conflict with the local anoxia/euxinia in intra-shelf environment based on the Fe speciation and Ce/Ce* data of the Jiulongwan section. As emphasized by Li et al. (2020), "there is no irreconcilable contradiction between local anoxia and extensively enhanced ocean oxygenation, as shown by the modern ocean in which anoxic basins exist locally despite generally oxic conditions globally". Therefore, although the $\delta^{238}U$ data suggest an extensive oceanic oxygenation event in the global open ocean (Zhang et al., 2019; Li et al., 2020), the local redox proxies (including Fe speciation, Ce anomaly) of the Doushantuo Formation at Jiulongwan suggest an overall anoxic/euxinic redox conditions in the intra-shelf basin.

3.4. Stratigraphic correlation

The stratigraphic correlation between the EN3/DOUNCE interval at Jiulongwan (Fig. 3A) and the much more expanded $\delta^{13}C_{carb}$ excursions at the upper Zhongling (Fig. 3E) and Yangjiaping sections (Fig. 3I) is not straightforward. Given the lack of direct geochronological constraints from these sections, their stratigraphic correlation largely relies on $\delta^{13}C_{carb}$ and $^{86}Sr/^{86}Sr$ chemostratigraphy. Two schemes of stratigraphic correlation between these sections have been proposed, including one scheme in which the upper 50 m of the Zhongling section is correlated with the EN3/DOUNCE interval at Jiulongwan, and the alternative view that only the upper 15 m of the Zhongling section is correlated with the EN3/DOUNCE interval (see both correlations in Fig. S7 of Li et al., 2010).

The potential existence of stratigraphic truncation, non-deposition, or faulting around the upper Doushantuo Formation may further complicate the correlation across the basin. It is notable that, although the Doushantuo Formation at Zhongling (260 m) is much thicker than at Jiulongwan (160 m), an integrated chemostratigraphic study suggests that the top of the Doushantuo Formation in the outer-shelf shoal region may have been stratigraphically truncated or with no deposition near the top (Cui et al., 2015). More recently, it was proposed that the variable stratigraphic expression of $\delta^{13}C_{carb}$ excursions in upper Doushantuo could be caused by multiple factors, including local facies variation, diagenesis, and/or potential unconformities (Zhou et al., 2017; Li et al., 2022).

Despite the above-mentioned uncertainties that may prevent a precise correlation of $\delta^{13}C_{carb}$ excursions in the upper Doushantuo Formation, we suggest that the ages of the $\delta^{13}C_{carb}$ negative excursions at Zhongling and Yangjiaping, including those extremely ^{13}C-depleted methane signals (Fig. 3E, 3I), may not be substantially different from that of the Jiulongwan EN3/DOUNCE interval. These methane signals have been interpreted as early diagenetic in origin (see Section 3.5 for details). Although the lower and middle Zhongling section has also been thoroughly investigated in the field, no calcite nodules or other evidence of methane were found. It appears that the massive mineralization of MDAC only occurred during the deposition of the upper Doushantuo and the basal Dengying formations.

It is important to point out that the division of the Doushantuo and Dengying formations at Yangjiaping is not always consistent in published literature. Some studies use the discrete phosphorite interval as the marker bed for the uppermost Doushantuo Formation (Zhu et al., 2007b; Jiang et al., 2011; Cui et al., 2015; Cui et al., 2017); whereas other studies place the Doushantuo–Dengying boundary slightly higher based on the termination of the $\delta^{13}C_{carb}$ negative excursion (Macouin et al., 2004; Ader et al., 2009; Kunimitsu et al., 2011; Furuyama et al., 2016). If we accept the former scheme, then negative $\delta^{13}C_{carb}$ signals also appear in the basal Dengying Formation (Fig. 3I); if we accept the later, all the negative $\delta^{13}C_{carb}$ signals are limited to the Doushantuo Formation. The Zhongling section bears very similar features to that of the Yangjiaping section. In addition, authigenic calcite at Zhongling has also been found in the fine-grained, gray dolostone interval immediately above the uppermost phosphorite layer of the Doushantuo Formation (Cui et al., 2017), although these nodules have not been systematically

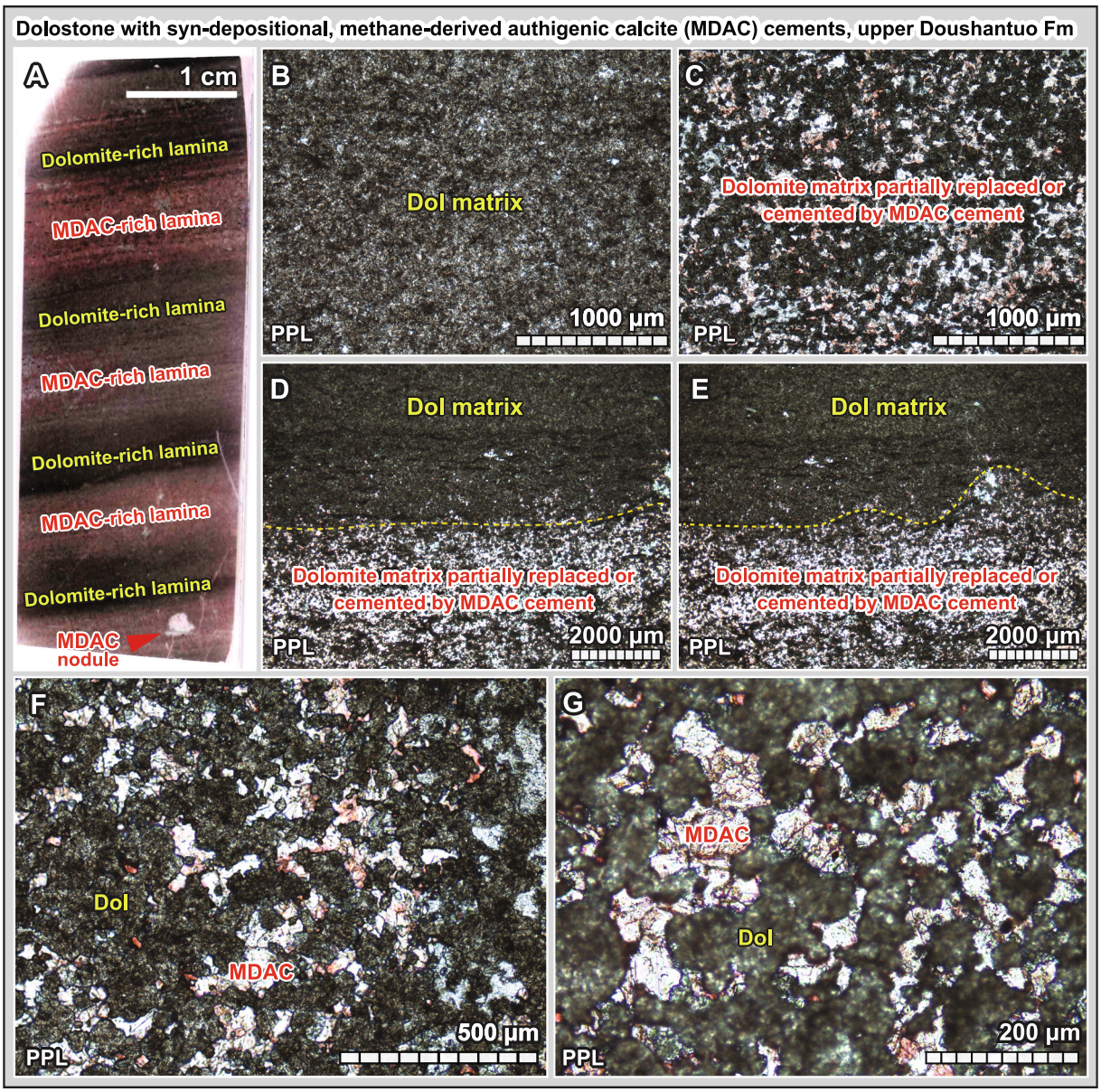

Fig. 5. Petrographic results of the Zhongling dolostone sample 12ZL-49.8 under transmitted-light optical microscopes. Note that the Zhongling dolostone is partially replaced or cemented by ^{13}C-depleted methane-derived authigenic calcite (MDAC). Both the dolomite matrix and the MDAC cements were analyzed by SIMS in this study. **(A)** Thin section slide (calcite is stained red by Alizarin-red S) showing interbedded dolomite-dominated laminae and MDAC-rich laminae. The interbedded texture suggests a *syn*-depositional origin for the MDAC cements. The width of this thin section is ca. 2 cm. **(B)** Petrographic view showing a lamina dominated by dolomite. **(C)** Petrographic view showing dolomite partially replaced or cemented by ^{13}C-depleted MDAC cements. **(D, E)** Petrographic views showing the transition between dolomite-dominated lamina and MDAC-rich lamina. **(F, G)** Petrographic views showing dolomite partially replaced or cemented by ^{13}C-depleted MDAC cements. Abbreviations: Cal, calcite; Dol, dolomite; MDAC, methane-derived authigenic calcite; PPL, plane polarized light.

analyzed for $\delta^{13}C_{carb}$ values. While the Doushantuo–Dengying boundary is likely to be diachronous across the basin (Yang et al., 2021), the different schemes of stratigraphic division do not affect our interpretation of the extremely negative and spatially variable $\delta^{13}C_{carb}$ reported here.

In summary, although multiple factors could complicate the precise correlation between the intra-shelf and outer-shelf shoal sections, the overall negative $\delta^{13}C_{carb}$ excursions at Zhongling and Yangjiaping (including those highly ^{13}C-depleted methane signals measured from authigenic calcite) appear to be broadly correlative to the SE at Jiulongwan. Therefore, we propose a causal link between these $\delta^{13}C_{carb}$ anomalies, which we further explore here.

3.5. Sedimentology of authigenic calcite

Three types of MDAC have been identified at outer-shelf sections based on detailed field and petrographic observations (Cui et al., 2016; Cui et al., 2017; Cui et al., 2022). In order to place our new SIMS $\delta^{13}C_{carb}$ data in a detailed sedimentological context, here we summarize the main features of the MDAC below.

(1). *MDAC nodules or lenses*. These nodules or lenses are mostly isolated from each other, rimmed by authigenic quartz, and generally aligned with sedimentary laminations, although laminations in host dolostone are sometimes cryptic. In some cases, calcite nodules or lenses are found to be surrounded by warping laminations, suggesting that these formed before sediment

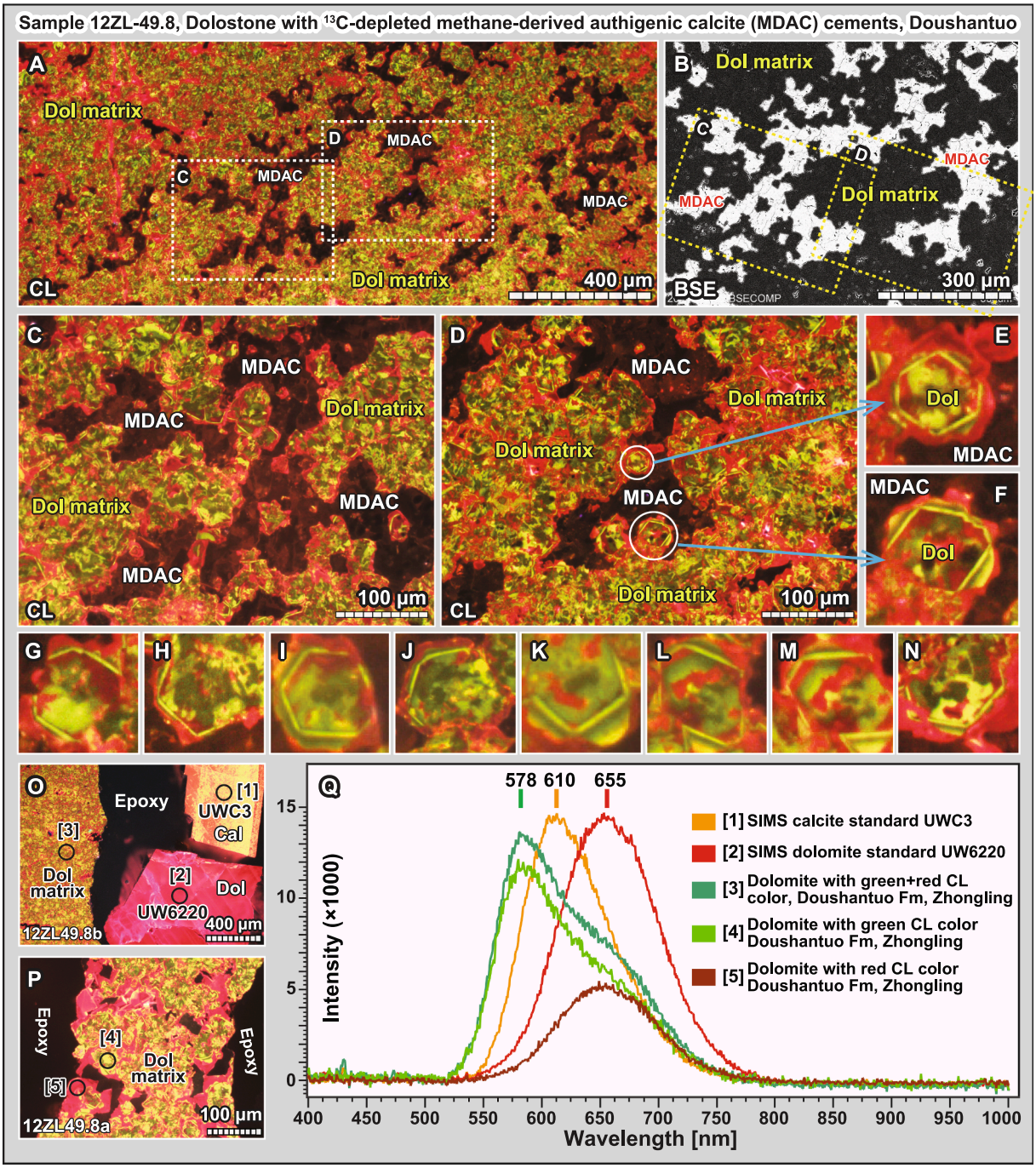

Fig. 6. Cold-cathode cathodoluminescence (CL) results and spectral analysis of the calcite and dolomite in sample 12ZL-49.8, Doushantuo Formation at the Zhongling section, South China. **(A)** The dolomite matrix (typically with positive $\delta^{13}C_{carb}$ values) shows distinct yellow-green + red luminescence, whereas the ^{13}C-depleted MDAC cement typically shows dull luminescence. Dashed-line boxes show the same views of images C and D. **(B)** A similar view of the center part of image A under BSE. Dolomicrite and ^{13}C-depleted MDAC cement show dark and bright color, respectively, under BSE. **(C, D)** Closer views of the domains marked by dashed-line boxes in images A and B. **(E, F)** Closer views of the two circles in D, showing hexagonal crystal shape in the dolomite matrix. **(G–N)** More hexagonal crystals found in the Zhongling dolomite matrix. These hexagonal crystals are ca. 20 to 30 μm in size, and indicate a vaterite or aragonite precursor for the studied Zhongling dolomite. **(O)** CL image of dolomite matrix and WiscSIMS standards (calcite UWC3, dolomite UW6220) in SIMS epoxy mount 12ZL-49.8b. Note that the calcite standard UWC3, dolomite standard UW6220, and Zhongling dolomite matrix show distinct orange, red, and zoned yellow-green + red colors, respectively. The size of analyzed spots (labeled 1, 2, 3) is ~120 μm in diameter. **(P)** CL image of dolomite matrix in SIMS epoxy mount 12ZL-49.8a. The size of analyzed spots (labeled 4, 5) is ~30 μm in diameter. **(Q)** CL spectra of the five analyzed spots corresponding to labeled spots in E–F. Abbreviations: BSE, backscattered electron; Cal, calcite; CL, cathodoluminescence; Dol, dolomite MDAC, methane-derived authigenic calcite; SE, secondary electron; SEM, scanning electron microscope.

compaction (Cui et al., 2022). $\delta^{13}C_{carb}$ compositions as low as –37.2‰ have been measured from the micro-drilled powders of these nodules. The thin rims of authigenic quartz have been interpreted to have formed prior to, or simultaneously with the calcite nodules as a result of change in porewater pH during early diagenesis (Cui et al., 2017).

(2). *MDAC with chicken wire texture or "ghost gypsum" texture.* In certain stratigraphic horizons, authigenic calcites show a mosaic

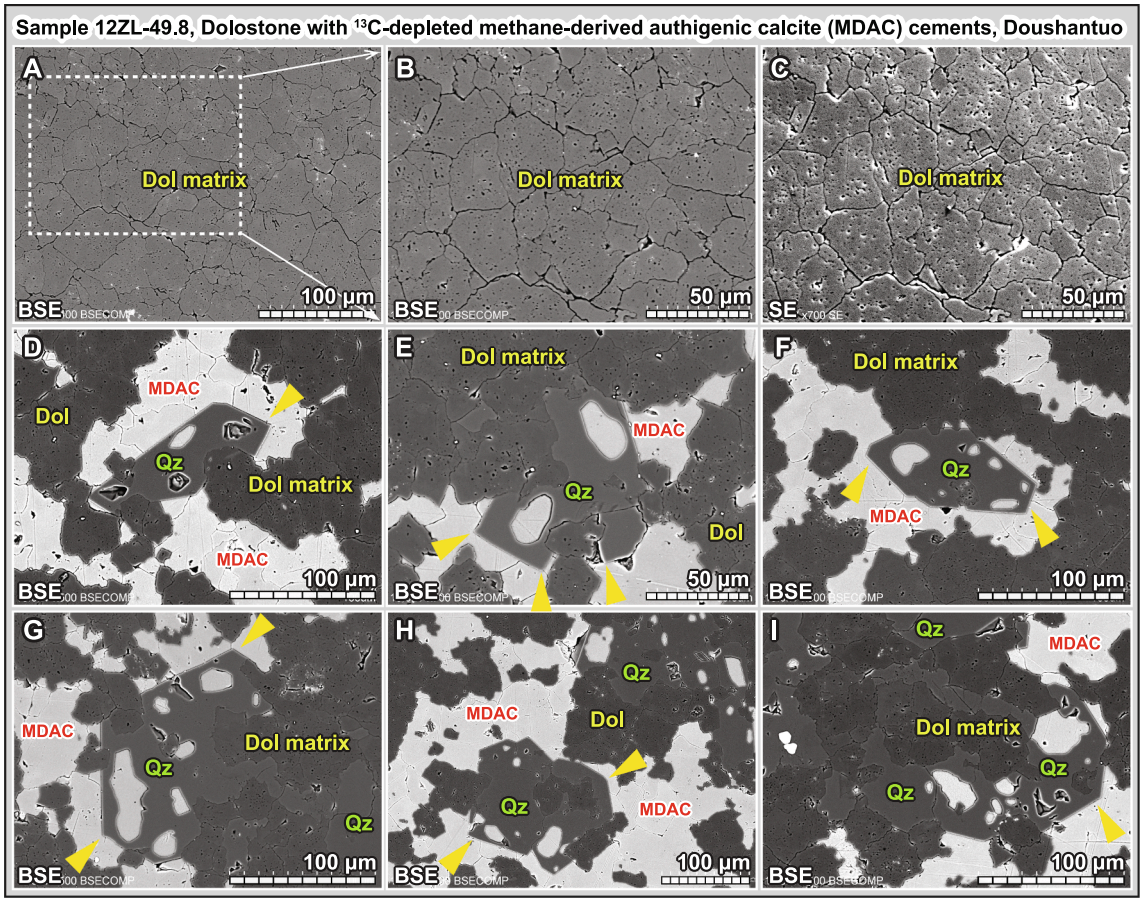

Fig. 7. Typical microscopic features of dolostone sample 12ZL-49.8 under SEM. **(A, B)** BSE images of dolomite matrix consisting of subhedral dolomicrite with an overall grain size of ca. 30 μm. Dashed-line box in A shows the same view of image B. **(C)** Secondary electron image of the same view in image B. Note the interlocking boundary of subhedral, inclusion-rich dolomicrite grains. **(D–I)** BSE images of dolomicrite matrix (dark color, inclusion-rich) partially replaced or cemented by ^{13}C-depleted MDAC cement (light color, inclusion-free) and a trace amount of authigenic quartz (gray color, inclusion-free). Note the sharp crystal terminations of authigenic quartz (yellow arrows). Both the dolomite matrix and the MDAC cements were analyzed by SIMS in this study. Abbreviations: BSE, backscattered electron; Cal, calcite; Dol, dolomite; MDAC, methane-derived authigenic calcite; Qz, quartz, SE, secondary electron; SEM, scanning electron microscope.

Table 2
XRD and geochemical results of micro-drilled powders of dolostone slab12ZL-49.8. This sample was collected from the upper Doushantuo Formation at the outer-shelf shoal Zhongling section, South China. The stratigraphic height of this sample is 209.2 m. Micro-drilled powders were collected using a drill bit of 800 μm in diameter. $\delta^{13}C_{carb}$ and $\delta^{18}O_{carb}$ data were analyzed by conventional GS-IRMS. XRD and geochemical data are from Cui et al. (2017). Laminae 2 and 3, 5 and 6 were newly investigated by integrated μXRF-SEM-CL-SIMS in this study. Abbreviations: MDAC, methane-derived authigenic calcite; GS-IRMS, gas source-isotope ratio mass spectrometry; XRD, X-ray diffraction.

Laminae (Fig. 4A)	XRD data of micro-drilled powders			GS-IRMS data of micro-drilled powders		Description	SIMS epoxy mounts (25-mm in diameter) investigated in this study
	Calcite [wt.%]	Dolomite [wt.%]	Quartz [wt.%]	$\delta^{13}C_{carb}$ [VPDB ‰]	$\delta^{18}O_{carb}$ [VPDB ‰]		
[1]	0.00	99.80	0.20	+2.8	–5.3	Dominated by dolomite	
[2]	3.24	95.83	0.93	+1.9	–6.3	Dominated by dolomite	Upper half of 12ZL-49.8a (Fig. A1)
[3]	39.12	59.81	1.07	–8.4	–7.2	Dolomite matrix; Rich in MDAC cement and quartz cement	Lower half of 12ZL-49.8a (Figs. A1, 9, 10)
[4]	0.45	99.16	0.39	+2.7	–5.8	Dominated by dolomite	
[5]	0.00	99.77	0.23	+2.7	–5.7	Dominated by dolomite	Upper half of 12ZL-49.8b (Fig. A2)
[6]	30.61	68.33	1.05	–8.8	–7.3	Dolomite matrix; Rich in MDAC cement and quartz cement	Lower half of 12ZL-49.8b (Figs. A2, 11)
[7]	0.40	99.38	0.22	+2.6	–5.7	Dominated by dolomite	
[8]	29.92	69.09	0.98	–10.5	–7.4	Dolomite matrix; Rich in MDAC cement and quartz cement	
[9]	0.04	99.69	0.27	+2.8	–5.3	Dominated by dolomite	
[10]	97.10	2.50	0.34	–34.1	–9.8	MDAC nodule	

Table 3
SIMS and EPMA data of calcite from the upper Doushantuo Formation, outer-shelf shoal Zhongling section, Hunan Province, South China. Each analyzed SIMS pit has a unique spot ID that can be retrieved in the online supplementary materials (Supplementary material 4). Elemental concentration data of each SIMS pit were obtained based on the EPMA analyses of two or three spots that are close to the SIMS pit (Supplementary material 5). An averaged Fe# value = [molar ratio of Fe/(Fe + Mg)] of two or three EMPA spots closely associated with each SIMS pit was used for the $\delta^{13}C_{calcite}$ correction of each SIMS pit. Elemental concentration value of "0.00" in the table represents under detection limit.

Sample	SIMS domain	SIMS spot ID	Mineralogy	SIMS $\delta^{13}C_{carb}$ [‰, VPDB]	2SD [‰]	Fe#	$MnCO_3$ [mol %]	$FeCO_3$ [mol %]	$MgCO_3$ [mol %]	$CaCO_3$ [mol %]
12ZL-49.8a	#1	@183	Calcite	–18.3	1.4	0.00	0.00	0.00	0.88	99.12
12ZL-49.8a	#1	@184	Calcite	–24.0	1.4	0.00	0.00	0.00	0.88	99.12
12ZL-49.8a	#1	@186	Calcite	–19.7	1.4	0.00	0.02	0.00	0.29	99.68
12ZL-49.8a	#1	@187	Calcite	–12.4	1.4	0.00	0.02	0.00	0.29	99.68
12ZL-49.8a	#1	@188	Calcite	–37.1	1.4	0.00	0.00	0.00	0.88	99.12
12ZL-49.8a	#1	@189	Calcite	–21.9	1.4	0.00	0.00	0.00	0.88	99.12
12ZL-49.8a	#1	@190	Calcite	–26.6	1.4	0.00	0.00	0.00	0.62	99.38
12ZL-49.8a	#1	@191	Calcite	–26.2	1.4	0.00	0.00	0.00	0.62	99.38
12ZL-49.8a	#1	@198	Calcite	–11.6	1.2	0.00	0.00	0.00	0.70	99.30
12ZL-49.8a	#1	@199	Calcite	–16.6	1.2	0.00	0.00	0.00	1.69	98.31
12ZL-49.8a	#1	@200	Calcite	–36.0	1.2	0.00	0.02	0.00	1.17	98.80
12ZL-49.8a	#1	@201	Calcite	–36.8	1.2	0.00	0.00	0.00	0.82	99.18
12ZL-49.8a	#1	@202	Calcite	–36.4	1.2	0.00	0.00	0.00	0.93	99.07
12ZL-49.8a	#1	@203	Calcite	–35.2	1.2	0.00	0.00	0.00	0.63	99.37
12ZL-49.8a	#1	@204	Calcite	–23.9	1.2	0.00	0.00	0.00	1.51	98.49
12ZL-49.8a	#1	@205	Calcite	–31.4	1.2	0.01	0.00	0.00	0.73	99.26
12ZL-49.8a	#2	@240	Calcite	–36.6	1.0	0.00	0.00	0.00	2.16	97.84
12ZL-49.8a	#2	@241	Calcite	–37.5	1.0	0.00	0.00	0.00	1.03	98.97
12ZL-49.8a	#2	@242	Calcite	–16.2	1.0	0.00	0.00	0.00	0.59	99.41
12ZL-49.8a	#2	@243	Calcite	–26.7	1.0	0.00	0.00	0.00	0.59	99.41
12ZL-49.8a	#2	@244	Calcite	–18.8	1.0	0.00	0.00	0.00	0.79	99.21
12ZL-49.8a	#2	@245	Calcite	–13.9	1.0	0.00	0.01	0.00	1.15	98.85
12ZL-49.8a	#2	@246	Calcite	–11.1	1.0	0.00	0.00	0.00	1.29	98.71
12ZL-49.8a	#2	@247	Calcite	–27.7	1.0	0.00	0.00	0.00	3.27	96.73
12ZL-49.8a	#2	@248	Calcite	–17.4	1.0	0.00	0.00	0.00	1.46	98.54
12ZL-49.8a	#2	@249	Calcite	–24.9	1.0	0.00	0.00	0.00	0.87	99.13
12ZL-49.8a	#2	@254	Calcite	–32.5	1.0	0.00	0.00	0.00	1.83	98.17
12ZL-49.8a	#2	@255	Calcite	–21.8	1.0	0.00	0.00	0.00	0.75	99.25
12ZL-49.8a	#2	@256	Calcite	–14.9	1.0	0.00	0.00	0.00	0.94	99.06
12ZL-49.8a	#2	@257	Calcite	–23.4	1.0	0.00	0.01	0.00	0.68	99.31
12ZL-49.8a	#2	@258	Calcite	–23.9	1.0	0.00	0.02	0.00	1.08	98.90
12ZL-49.8a	#2	@259	Calcite	–11.0	1.0					
12ZL-49.8a	#2	@260	Calcite	–14.9	1.0					
12ZL-49.8a	#2	@261	Calcite	–29.1	1.0	0.00	0.00	0.00	1.77	98.23
12ZL-49.8a	#2	@262	Calcite	–26.9	1.0	0.00	0.00	0.00	0.77	99.23
12ZL-49.8a	#2	@263	Calcite	–12.6	1.0	0.00	0.00	0.00	1.56	98.44
12ZL-49.8a	#2	@265	Calcite	–28.7	1.0	0.00	0.01	0.01	1.22	98.77
12ZL-49.8b	#3	@499	Calcite	–29.3	1.0	0.00	0.00	0.00	1.50	98.50
12ZL-49.8b	#3	@500	Calcite	–9.3	1.0	0.00	0.02	0.00	0.71	99.27
12ZL-49.8b	#3	@501	Calcite	–19.8	1.0	0.00	0.00	0.00	1.40	98.60
12ZL-49.8b	#3	@502	Calcite	–26.0	1.0	0.00	0.00	0.00	0.70	99.30
12ZL-49.8b	#3	@503	Calcite	–18.7	1.0	0.00	0.00	0.00	1.04	98.96
12ZL-49.8b	#3	@504	Calcite	–24.2	1.0	0.00	0.00	0.00	1.15	98.85
12ZL-49.8b	#3	@505	Calcite	–15.1	1.0	0.00	0.00	0.00	2.96	97.04
12ZL-49.8b	#3	@506	Calcite	–20.5	1.0	0.02	0.01	0.02	0.65	99.33
12ZL-49.8b	#3	@507	Calcite	–36.6	1.0	0.00	0.00	0.00	0.87	99.13
12ZL-49.8b	#3	@508	Calcite	–17.3	1.0	0.00	0.00	0.00	0.87	99.13
12ZL-49.8b	#3	@509	Calcite	–37.2	1.0	0.00	0.00	0.00	0.70	99.30
12ZL-49.8b	#3	@510	Calcite	–17.8	1.0	0.00	0.00	0.00	0.75	99.25
12ZL-49.8b	#3	@516	Calcite	–11.9	1.0	0.00	0.01	0.00	1.51	98.49
12ZL-49.8b	#3	@517	Calcite	–12.3	1.0	0.00	0.00	0.00	0.67	99.33
12ZL-49.8b	#3	@518	Calcite	–31.6	1.0	0.01	0.02	0.01	0.95	99.03
12ZL-49.8b	#3	@519	Calcite	–15.0	1.0	0.00	0.02	0.00	1.42	98.55
12ZL-49.8b	#3	@520	Calcite	–24.0	1.0	0.00	0.00	0.00	0.73	99.27

texture of compacted nodules (i.e., chicken wire texture) (Cui et al., 2022), which is typical of gypsum nodules formed in evaporative environments (Hardie, 2003). Some samples show calcite with vertically aligned boundaries (Cui et al., 2022), resembling those of "ghost gypsum" and thus supporting an evaporite mineral precursor (Warren, 2016).

(3). *MDAC cements*. It is important to note that many dolostone laminae consist of fine-grained dolomicrite matrix that are rich in MDAC cements (Figs. 4–7, 9–11, A1, A2) — the focus of this SIMS study. The MDAC cements typically consist of calcite crystals tens to hundreds of μm in size, therefore, are not obvious in outcrops. However, when viewed under an optical microscope or SEM, the MDAC cements are distributed parallel to the sedimentary beddings (Fig. 5A). XRD analysis of the MDAC-rich laminae reveals that MDAC cements can account for up to 30–40% of the total carbonates (Fig. 4). Due to the spatial limitations of micro-drilling techniques (i.e., drill holes ~800 μm diameter in diameter), previous studies were unable to effectively separate dolomite matrix and calcite cements via micro-drilling. The isotopic composition and heterogeneity of the MDAC cement was, therefore, not documented. In this study, we focus on this type of calcite and obtain in-situ and spatially resolved $\delta^{13}C_{carb}$ data using SIMS (see Section 5 for details).

Table 4
SIMS and EPMA data of dolomite from the upper Doushantuo Formation, outer-shelf shoal Zhongling section, Hunan Province, South China. Each analyzed SIMS pit has a unique spot ID that can be retrieved in the online supplementary materials (Supplementary material 4). Elemental concentration data of each SIMS pit were obtained based on the EPMA analyses of two or three spots that are close to the SIMS pit (Supplementary material 5). An averaged Fe# value = [molar ratio of Fe/(Fe + Mg)] of two or three EMPA spots closely associated with each SIMS pit was used for the $\delta^{13}C_{calcite}$ correction of each SIMS pit. Elemental concentration value of "0.00" in the table represents under detection limit.

Sample	SIMS domain	SIMS spot ID	Mineralogy	SIMS $\delta^{13}C_{carb}$ [‰, VPDB]	2SD [‰]	Fe#	$MnCO_3$ [mol %]	$FeCO_3$ [mol %]	$MgCO_3$ [mol %]	$CaCO_3$ [mol %]
12ZL-49.8a	#1	@206	Dolomite	+2.7	1.2	0.00	0.00	0.00	48.25	51.75
12ZL-49.8a	#1	@207	Dolomite	+4.0	1.2	0.00	0.01	0.00	48.55	51.43
12ZL-49.8a	#1	@212	Dolomite	+1.8	1.1	0.00	0.00	0.03	48.71	51.25
12ZL-49.8a	#1	@213	Dolomite	+3.3	1.1	0.00	0.00	0.00	48.36	51.64
12ZL-49.8a	#1	@214	Dolomite	+2.5	1.1	0.00	0.00	0.06	48.63	51.31
12ZL-49.8a	#1	@215	Dolomite	+1.6	1.1	0.00	0.01	0.00	49.34	50.65
12ZL-49.8a	#1	@216	Dolomite	+2.3	1.1	0.00	0.00	0.04	48.60	51.36
12ZL-49.8a	#1	@217	Dolomite	+2.5	1.1	0.00	0.00	0.00	48.13	51.87
12ZL-49.8a	#1	@218	Dolomite	+0.6	1.1	0.00	0.00	0.00	48.68	51.32
12ZL-49.8a	#1	@220	Dolomite	+1.7	1.1	0.00	0.01	0.02	48.20	51.77
12ZL-49.8a	#1	@221	Dolomite	+2.4	1.1	0.00	0.00	0.00	48.65	51.34
12ZL-49.8a	#2	@227	Dolomite	+1.6	1.0	0.00	0.00	0.01	48.50	51.49
12ZL-49.8a	#2	@228	Dolomite	+3.6	1.0	0.00	0.00	0.00	48.72	51.28
12ZL-49.8a	#2	@229	Dolomite	+0.7	1.0	0.00	0.00	0.02	48.84	51.14
12ZL-49.8a	#2	@230	Dolomite	+1.2	1.0	0.00	0.00	0.02	48.59	51.39
12ZL-49.8a	#2	@231	Dolomite	+3.3	1.0	0.00	0.00	0.03	48.19	51.78
12ZL-49.8a	#2	@232	Dolomite	+2.3	1.0	0.00	0.00	0.00	50.11	49.89
12ZL-49.8a	#2	@233	Dolomite	+3.7	1.0	0.00	0.00	0.03	48.20	51.77
12ZL-49.8a	#2	@234	Dolomite	+2.9	1.0	0.00	0.00	0.00	49.30	50.70
12ZL-49.8b	#3	@498	Dolomite	+1.8	1.0	0.00	0.00	0.01	48.44	51.55
12ZL-49.8b	#3	@521	Dolomite	–1.5	1.0	0.00	0.01	0.07	48.09	51.84
12ZL-49.8b	#3	@522	Dolomite	+0.2	1.0	0.00	0.00	0.07	48.24	51.69
12ZL-49.8b	#3	@523	Dolomite	+2.2	1.0	0.00	0.00	0.02	47.18	52.79
12ZL-49.8b	#3	@524	Dolomite	+1.8	1.0	0.00	0.01	0.03	48.42	51.54
12ZL-49.8b	#3	@525	Dolomite	+2.0	1.0	0.00	0.00	0.04	48.09	51.87

Table 5
Comparison of the SEM-CL-SIMS results from both calcite and dolomite in the upper Doushantuo Formation, South China. The 2SD represents two standard deviations of each SIMS data set (note: not analytical precision). The value n represents the number of analyzed SIMS spots. Data source: Jiulongwan SIMS-SEM data (Cui et al., 2021); Zhongling SIMS-SEM data (this study).

Upper Doushantuo Formation	Mineral	Typical texture	CL	SEM petrography		SIMS $\delta^{13}C_{carb}$ data (VPDB, ‰)					Interpretations	
				Features	Grain size	Min	Max	Mean	2SD	n	Paragenesis	Carbon source
Zhongling section (outer-shelf shoal environment)	Dolomite	Matrix (in dolostones)	Red and yellow-green	Homogeneous, subhedral	ca. 30 μm	–1.5	+4.0	+2.0	2.29	25	Syn-depositional	Open marine DIC
	Calcite	Cement (in dolostones)	Dull	Homogeneous, subhedral, sparry	Irregular	–37.5	–9.3	–23.2	16.08	54	Early diagenetic	Methane-derived alkalinity in porewater of shallow marine sediments
Jiulongwan section (intra-shelf environment)	Calcite	Matrix (in dolomitic limestones)	Relatively uniform	Homogeneous microspar, interlocking boundary	ca. 5–10 μm	–9.5	–6.2	–8.2	1.51	36	Depositional	Seawater DIC mixed with methane-derived alkalinity in the bottom water column of a restricted basin
	Dolomite	Disseminated replacement (in dolomitic limestones)	Zoned in dolomitic limestones	Zoned, disseminated, often with irregular boundary with surrounding calcite microspars	up to 100 μm	–11.2	–3.8	–7.9	2.93	91	Post-depositional	Inherited from preexisting calcite

3.6. Paragenesis of authigenic calcite

Interpreting the origin of different types of MDACs in the upper Doushantuo Formation requires a careful evaluation of paragenesis. Multiple lines of field, petrographic, and geochemical evidence suggest that the MDAC is early diagenetic in origin and formed via microbial sulfate reduction (MSR) and anaerobic oxidation of methane (AOM) through initial dissolution of preexisting dolomicrite or gypsum and subsequent early diagenetic formation of authigenic phases.

First, no obvious evidence for hydrothermal fluids was found to be closely associated with MDAC. We indeed noticed some late calcite veins that vertically crosscut sedimentary bedding in the field, but these veins show mildly negative $\delta^{13}C_{carb}$ values (ca. –5‰) (Cui et al., 2017), and are therefore unlikely to be the carbon source of the MDAC.

Second, the MDACs show $^{87}Sr/^{86}Sr$ ratios of ca. 0.7081 to 0.7083 (Cui et al., 2017), which are consistent with the reconstructed Ediacaran seawater signals based on a global compilation (see Fig. 17 in Cui et al., 2020a). The dolomite matrix normally shows slightly higher $^{87}Sr/^{86}Sr$

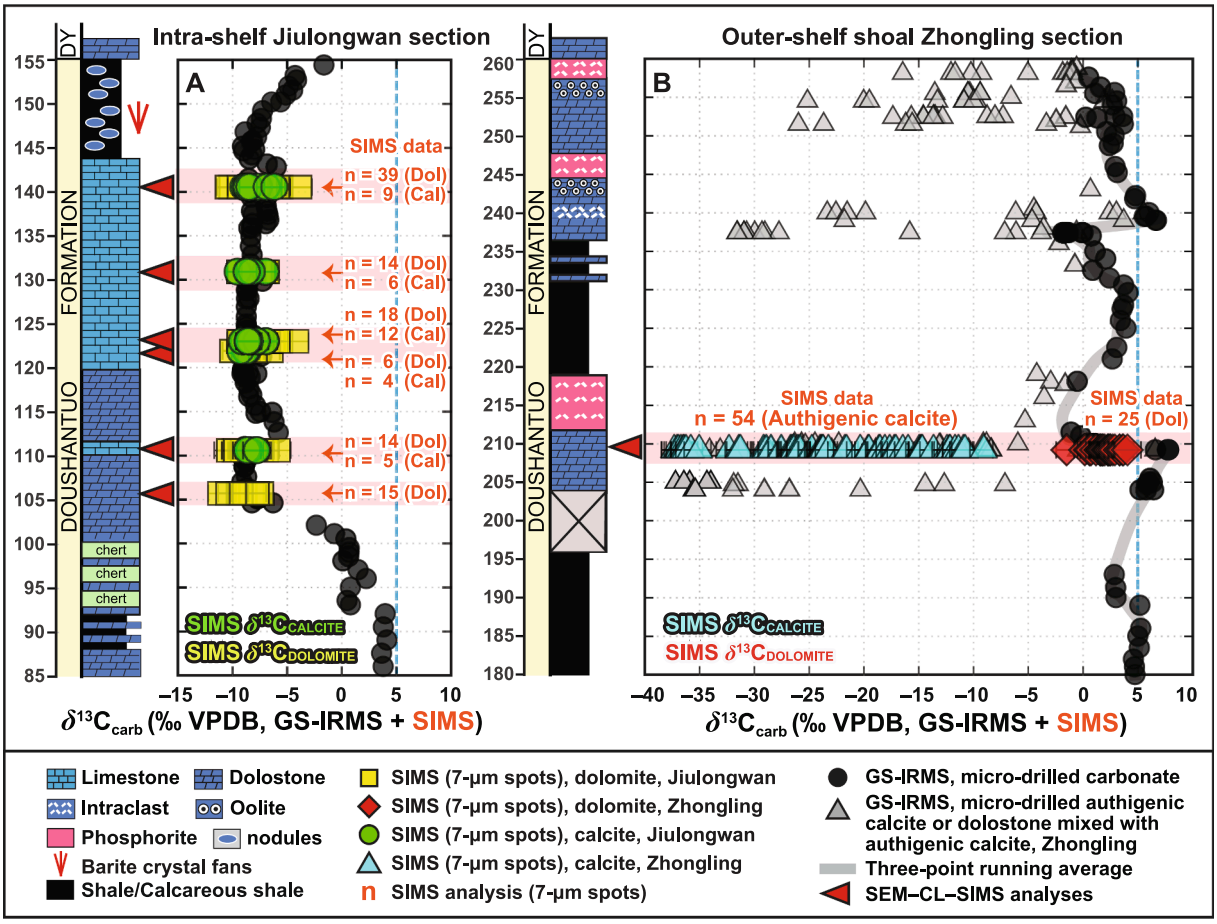

Fig. 8. Chemostratigraphic $\delta^{13}C_{carb}$ profiles of the upper Doushantuo Formation at Jiulongwan and Zhongling, South China. Red triangles alongside the lithological columns of Jiulongwan and Zhongling sections represent the horizons investigated by SIMS (Cui et al., 2021; this study). The numbers of SIMS spots (n) analyzed on calcite and dolomite are also provided for each sample. Blue dashed line ($\delta^{13}C_{carb} = +5‰$) represents the background value of depositional carbonate of the upper Doushantuo Formation during the Ediacaran Period. **(A)** $\delta^{13}C_{carb}$ profile of the upper Doushantuo Formation at the intra-shelf Jiulongwan section, Hubei Province, South China. **(B)** $\delta^{13}C_{carb}$ profile of the upper Doushantuo Formation at the outer-shelf shoal Zhongling section, Hunan Province, South China. Note that these SIMS $\delta^{13}C_{carb}$ data show two important features: (i) In strong contrast with the Jiulongwan SIMS data that show a relatively narrower range (i.e., $\delta^{13}C_{carb}$ from –11.2 to –3.8‰, n = 127), the new SIMS results of Zhongling samples reveal a much wider range (i.e., $\delta^{13}C_{carb}$ from –37.5‰ in calcite to +4.0‰ in dolomite, n = 79); (ii) The Jiulongwan SIMS $\delta^{13}C_{calcite}$ and $\delta^{13}C_{dolomite}$ data largely overlap, while the Zhongling SIMS $\delta^{13}C_{calcite}$ and $\delta^{13}C_{dolomite}$ data reveal two distinct end-members. Data Source: Jiulongwan $\delta^{13}C_{carb}$ data analyzed by GS-IRMS (McFadden et al., 2008); Jiulongwan $\delta^{13}C_{carb}$ data analyzed by SIMS (Cui et al., 2021); Zhongling $\delta^{13}C_{carb}$ data analyzed by GS-IRMS (Cui et al., 2015; Cui et al., 2017); Zhongling $\delta^{13}C_{carb}$ data analyzed by SIMS (this study). Abbreviations: Cal, calcite; Dol, dolomite; DY, Dengying; GS-IRMS, gas-source isotope ratio mass spectrometer; SIMS, secondary ion mass spectrometer.

ratios, which has been attributed to the loss of Sr during dolomitization, and the addition of ^{87}Sr from the radioactive decay of ^{87}Rb in admixed clay minerals.

The finding of chicken wire texture at certain stratigraphic horizons indicates that some MDAC nodules formed via post-depositional replacement of pre-existing gypsum (Cui et al., 2022). However, the typical Ediacaran seawater $^{87}Sr/^{86}Sr$ values preserved in these authigenic calcite nodules (Cui et al., 2017) suggest that the replacement of gypsum by calcite occurred very early, likely around the sediment–water interface with primary $^{87}Sr/^{86}Sr$ diffused from coeval seawater.

It is worth mentioning that MDAC has also been reported in the cap carbonates of the basal Doushantuo Formation in the Yangtze Gorges area (Jiang et al., 2003; Jiang et al., 2006; Wang et al., 2008; Bristow et al., 2011; Zhou et al., 2016; Wang et al., 2017b), but in stark contrast, these MDACs within cap carbonates preserve far more elevated $^{87}Sr/^{86}Sr$ compositions (i.e., >0.70990) (Sawaki et al., 2010; Bristow et al., 2011), suggesting a highly radiogenic source of fluids.

Third, the sedimentological relationship between sedimentary laminations and MDAC nodules is not always obvious in the field, but in certain horizons, authigenic calcite nodules or lenses are found to be surrounded by warping laminations, suggesting that the nodules or lenses formed during early diagenesis, before sediment compaction (Cui et al., 2022).

Fourth, elemental analyses of individual MDAC nodules show much higher Sr concentration and much lower Fe, Mn, and Rb concentrations than the dolomite matrix (Cui et al., 2017). The MDAC nodules are rich in Sr (mean value: 1681 ppm; n = 6), with Mn/Sr and Rb/Sr ratios all near zero (Cui et al., 2017). These elemental data suggest that MDAC nodules were not formed via meteoric water diagenesis or late diagenesis, which generally leads to progressively lower Sr concentrations and higher Mn/Sr and Rb/Sr ratios (e.g., Brand and Veizer, 1980; Kaufman et al., 1992; Banner, 1995; Melim et al., 2002; Zhao et al., 2020).

Fifth, based on detailed petrographic and SEM observations, there is no clear evidence of late veins or stylolites directly associated with the

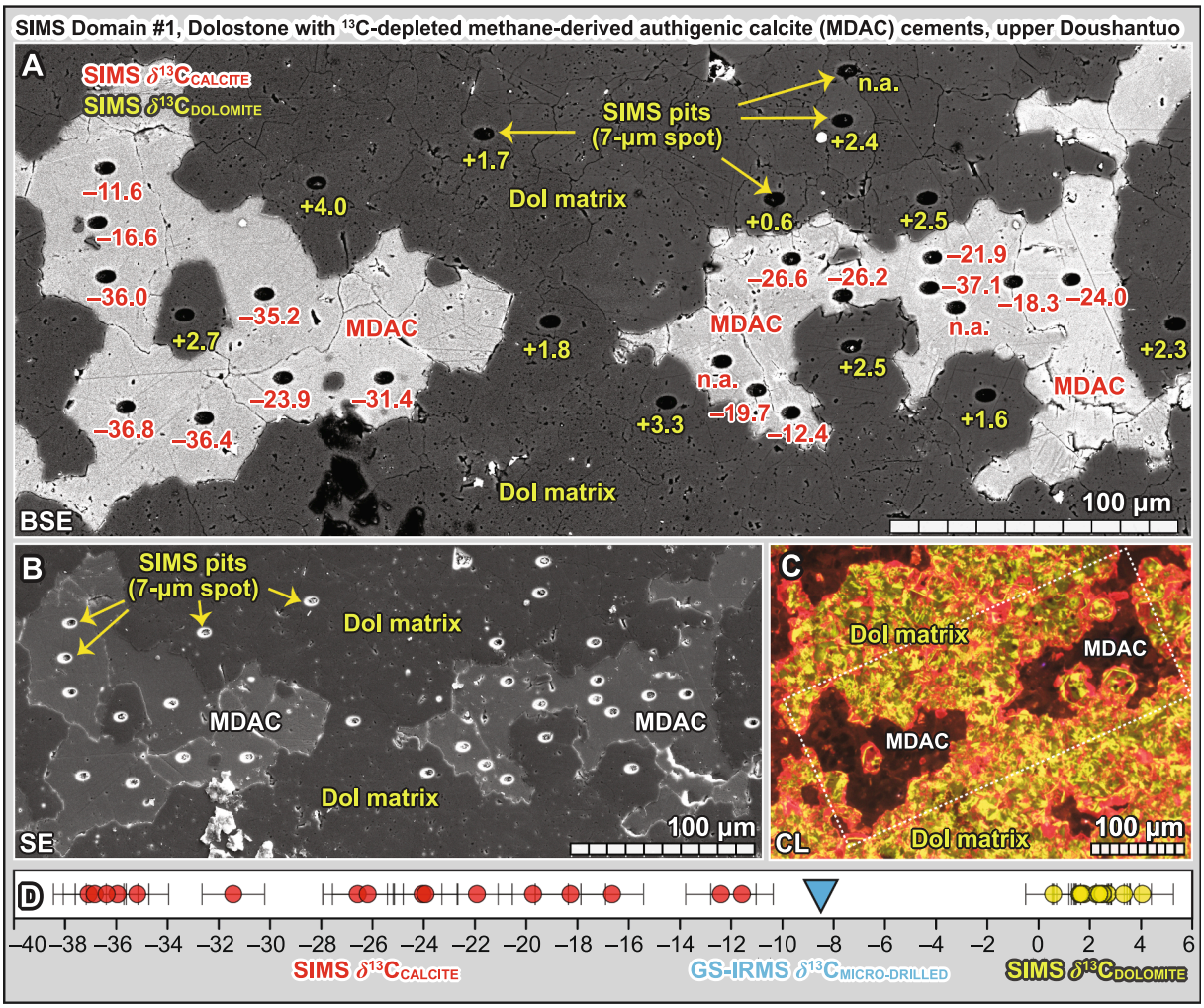

Fig. 9. Integrated SEM-CL-SIMS results of dolomite matrix and methane-derived authigenic calcite (MDAC) cements in SIMS Domain #1, sample 12ZL-49.8a, upper Doushantuo Formation, Zhongling section, South China. Values of $\delta^{13}C_{carb}$ are adjacent to 7-μm SIMS pits. Detailed position of this SIMS domain can be traced in Fig. A1. **(A)** BSE image with SIMS $\delta^{13}C_{calcite}$ and $\delta^{13}C_{dolomite}$ (‰, VPDB) data shown in red and yellow color, respectively. Note the remarkable μm-scale heterogeneity of $\delta^{13}C_{carb}$ on authigenic calcite cements, which was revealed by SIMS in this study. **(B)** Corresponding SE image of A. **(C)** Corresponding cold-cathode CL image, with the dashed-line box marking the same view of A and B. Note the yellow-green + red luminescence of dolomite and the overall dull luminescence of ^{13}C-depleted authigenic calcite. Some dolomite crystals show hexagonal crystal shapes, which indicate a vaterite or aragonite precursor for the Zhongling dolomite. **(D)** Plot of individual SIMS $\delta^{13}C_{calcite}$ (‰, VPDB, 7-μm spot size, red circles) and $\delta^{13}C_{dolomite}$ (‰, VPDB, 7-μm spot size, yellow circles) data points measured from this domain. Error bars represent two standard deviations. Measured $\delta^{13}C_{carb}$ of micro-drilled powders (~800-μm spot size, blue triangle) by GS-IRMS is also plotted. Data source: SIMS data (this study); GS-IRMS data (Cui et al., 2017). Abbreviations: BSE, backscattered electron; Cal, calcite; CL, cathodoluminescence; Dol, dolomite; GS-IRMS, gas source-isotope ratio mass spectrometry; MDAC, methane-derived authigenic calcite; Qz, quartz; SE, secondary electron; SEM, scanning electron microscope.

μm-scale MDAC cements (Figs. 5–7, A1, A2). The disseminated MDAC cements, while sparry, do not show any texture that is indicative of pseudomorphs of preexisting evaporite minerals (e.g., gypsum, anhydrite). Therefore, we rule out the possibility that the μm-scale MDAC cements result from replacement of evaporite minerals. Instead, the μm-scale MDAC cements are exclusively distributed along sedimentary laminae (Fig. 4A. 5A) and appear to have been precipitated *syn*-depositionally or during early diagenesis.

Sixth, viewed on a broader scale, both the Zhongling and Yangjiaping sections, which are only 4 km apart, preserve very similar sedimentological textures and geochemical signals (Fig. 3E, 3I). The fact that these MDACs were exclusively found in the same stratigraphic interval (i.e., the uppermost Doushantuo and the basal Dengying formations) at both sections indicates that MDAC mineralization was a *syn*-depositional event. It is conceivable that a potential flow of post-depositional hydrothermal fluids confined by sedimentary beds can influence both sections, but petrographic and geochemical observations of the host sedimentary rocks and the textures associated with MDAC do not support the presence of such fluids.

Based on the evidence presented above, although a post-depositional origin cannot be completely excluded, an early diagenetic origin with active sulfate-driven AOM in pore fluids of shallow marine sediments is preferred for the MDAC in the upper Doushantuo Formation in outer-shelf regions.

4. Samples and methods

Following our recent SIMS study of the upper Doushantuo Formation at intra-shelf Jiulongwan (Cui et al., 2021), here we focus on the outer-shelf shoal Zhongling section in order to obtain a basin-wide view of the SE in South China (Fig. 2). Two SIMS epoxy mounts with 2-cm rock billets from a dolostone sample at Zhongling were newly analyzed by integrated μXRF, SEM, CL, and SIMS (Figs. A1, A2). Detailed descriptions of the SIMS and EPMA methods can be found in Cui et al. (2021) and are briefly summarized below.

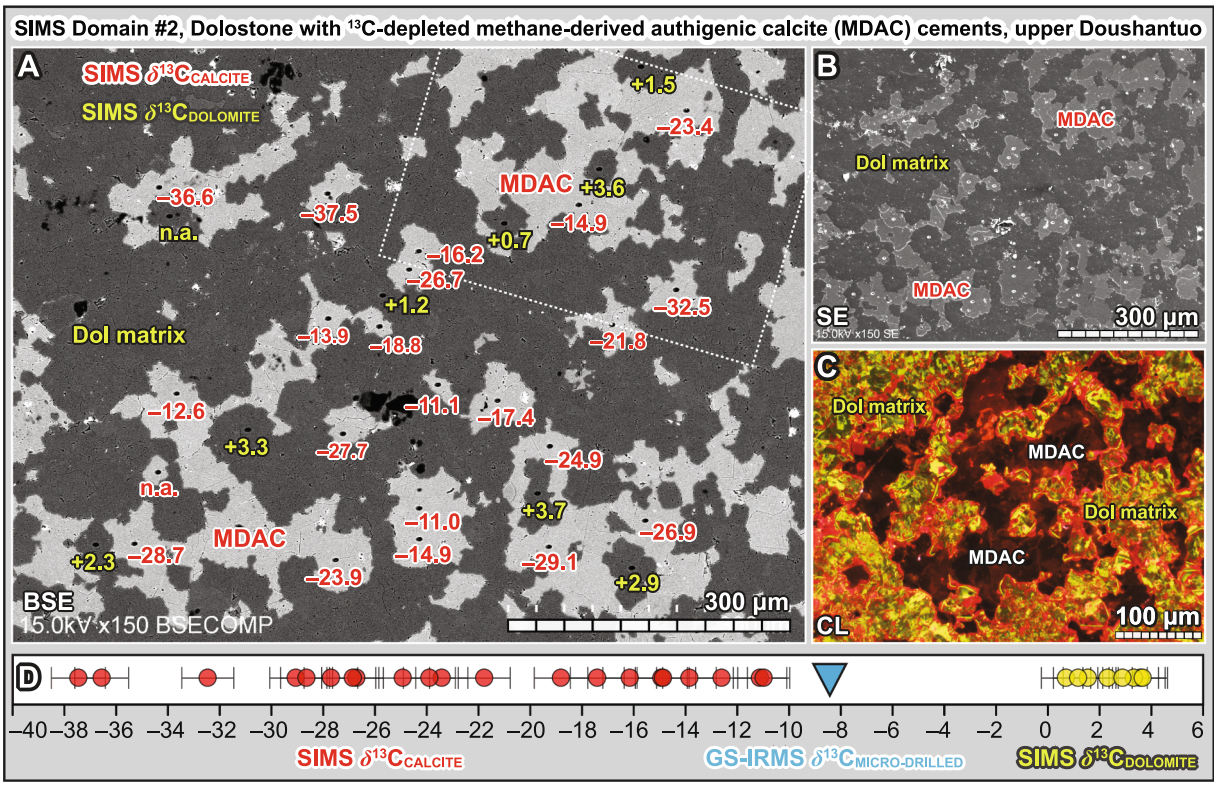

Fig. 10. Integrated SEM-CL-SIMS results of dolomite matrix and methane-derived authigenic calcite (MDAC) cements in SIMS Domain #2, sample 12ZL-49.8a, upper Doushantuo Formation, Zhongling section, South China. Values of $\delta^{13}C_{carb}$ are adjacent to 7-µm SIMS pits. Detailed position of this SIMS domain can be traced in Fig. A1. **(A)** BSE image with SIMS $\delta^{13}C_{calcite}$ and $\delta^{13}C_{dolomite}$ (‰, VPDB) data shown in red and yellow color, respectively. Dashed-line box marks the same view of image C. Note the remarkable µm-scale heterogeneity of $\delta^{13}C_{carb}$ on authigenic calcite cements, which was revealed by SIMS in this study. **(B)** Corresponding SE image of image A. **(C)** Cold-cathode CL image of the view marked by dashed-line box in A. Note the distinct yellow-green + red luminescence of dolomite and the overall dull luminescence of ^{13}C-depleted authigenic calcite. **(D)** Plot of individual SIMS $\delta^{13}C_{calcite}$ (‰, VPDB, 7-µm spot size, red circles) and $\delta^{13}C_{dolomite}$ (‰, VPDB, 7-µm spot size, yellow circles) data points measured from this domain. Error bars represent two standard deviations. Measured $\delta^{13}C_{carb}$ of micro-drilled powders (~800-µm spot size, blue triangle) by GS-IRMS is also plotted. Data source: SIMS data (this study); GS-IRMS data (Cui et al., 2017). Abbreviations: BSE = back-scattered electron; Cal, calcite; CL, cathodoluminescence; Dol, dolomite; GS-IRMS, gas source-isotope ratio mass spectrometry; MDAC, methane-derived authigenic calcite; Qz, quartz; SE, secondary electron; SEM, scanning electron microscope.

4.1. µXRF analysis

Both SIMS mounts were investigated by micro-X-ray Fluorescence (µXRF) before SIMS analysis. High-resolution elemental abundance maps of the polished sample surfaces (Fig. 4) were produced using the M4 Tornado µXRF scanner (Bruker nano GmbH, Berlin, Germany) at Vrije Universiteit Brussel, Brussels, Belgium. µXRF mapping was performed along a 2D grid with 25 µm spacing, a spot size of 25 µm and an integration time of 1 ms per pixel. The X-ray source was operated under maximum energy settings (600 µA, 50 kV) with no source filters. This mapping approach by µXRF resulted in qualitative element concentration distributions on the elemental maps.

4.2. CL imaging and CL intensity analysis

Most of the cathodoluminescence (CL) images in this study were generated by a cold-cathode CITL CL system (Cambridge Image Technology – model Mk5, UK) in the Department of Geology, University of Mons, Belgium. A few additional CL images were generated by a hot-cathode CL at UW-Madison and are presented in the online supplementary material-6. The cold-cathode CL instrument was operated at 15 kV acceleration voltage, 500 µA beam current, and a current density of about 8 µA/mm^2. CL images were captured with a Peltier-cooled digital color camera (Lumenera model Infinity 3, Canada) set from 0.1 s to a few seconds exposure time depending on the CL intensity and microscope magnification. Multiple-frame averaging was used to reduce noise. Color calibration of the camera (white balance) was performed using the blue-filtered, tungsten-halogen light source of the microscope, which may result in CL colors that are slightly different from other equipment (especially around the yellow band, which is narrow), but ensures more or less standardized observation conditions.

CL intensity of MDAC cements was measured on the region of interest (ROI) adjacent to each SIMS pit based on reprocessed CL images (Fig. A3). Due to the much brighter luminescence of dolomite than MDAC, dolomite is masked before the measurement of CL intensity for MDAC. We further adjusted the image contrast in order to enhance the subtle changes in CL intensity of MADC (Fig. A3). The CL image was then transformed to grey levels (8-bits) for intensity measurement. The ROI was manually selected adjacent to each SIMS pit assuming that it is representative of the SIMS pit. The mean grey level of the ROI was then measured by Fiji software (Schindelin et al., 2012) and reported as the average CL intensity.

Nearby EPMA spots were carefully avoided as they usually have a lower CL intensity after high electron bombardment. Both SIMS pits and EPMA spots are visible on CL images based on their distinct shape, size, shadow, and/or dark CL. The locations of SIMS pits and EPMA spots were double checked based on the available SE and BSE images. It should be noted that the above procedure is only valid for each individual CL image or domain. The CL intensity data measured from individual CL images should not be grouped together, because the electron dose received by each domain during various previous analyses may not be equivalent. Therefore, the CL intensity baseline may change from domain to domain.

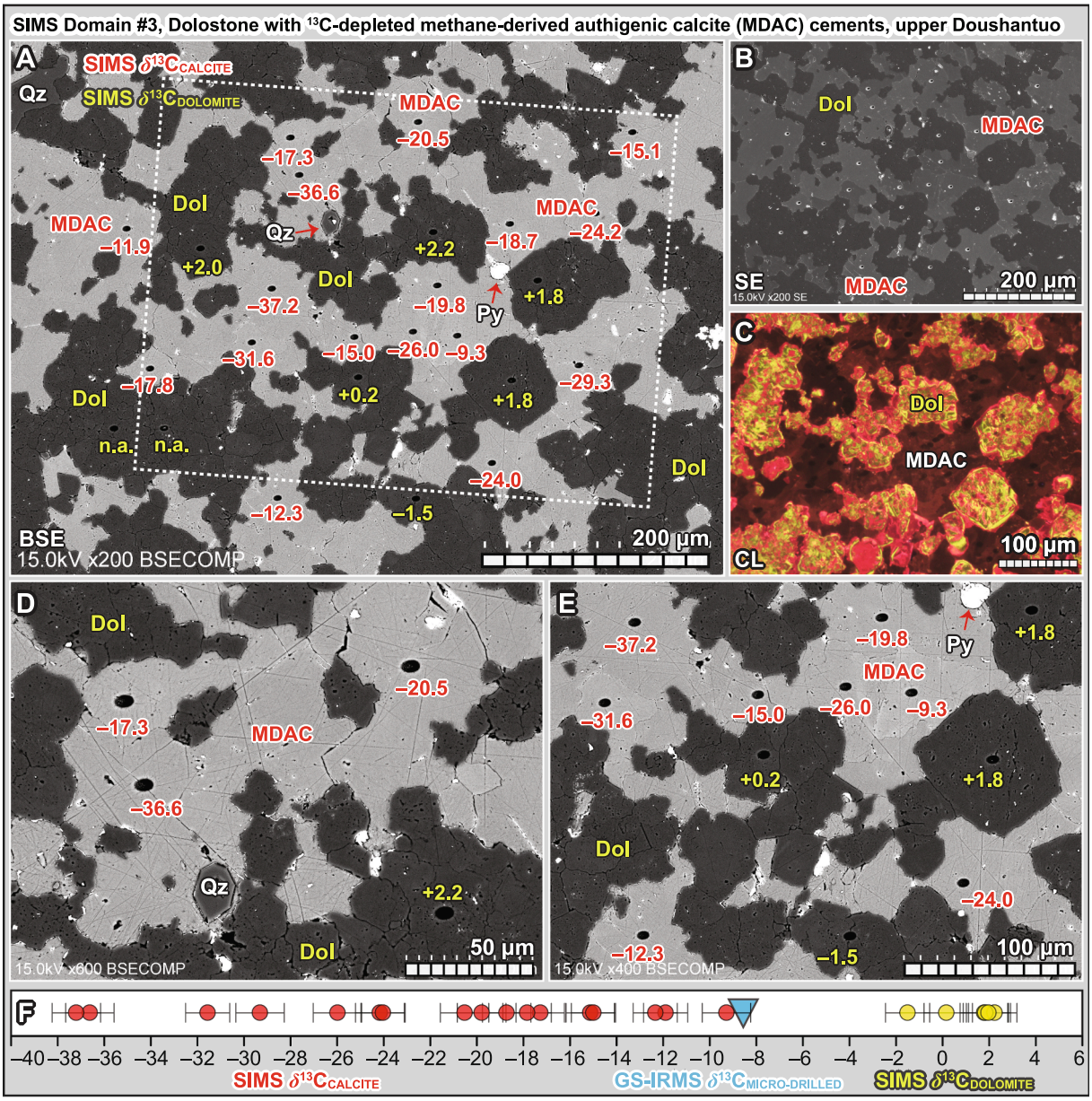

Fig. 11. Integrated SEM-CL-SIMS results of dolomite matrix and methane-derived authigenic calcite (MDAC) cements in SIMS Domain #3, sample 12ZL-49.8b, upper Doushantuo Formation, Zhongling section, South China. Values of $\delta^{13}C_{carb}$ are adjacent to 7-µm SIMS pits. Detailed position of this SIMS domain can be traced in Fig. A2. **(A)** BSE image with SIMS $\delta^{13}C_{calcite}$ and $\delta^{13}C_{dolomite}$ (‰, VPDB) data shown in red and yellow color, respectively. Dashed-line box marks the same view of image C. Note the remarkable µm-scale heterogeneity of $\delta^{13}C_{carb}$ on authigenic calcite cements, which was revealed by SIMS in this study. **(B)** Corresponding SE image of image A. **(C)** Corresponding cold-cathode CL image of area marked by the dashed-line box in A. Note the distinct yellow-green + red luminescence of dolomite and the overall dull luminescence of ^{13}C-depleted authigenic calcite. **(D–E)** Closer views of image A. **(F)** Plot of individual SIMS $\delta^{13}C_{calcite}$ (‰, VPDB, 7-µm spot size, red circles) and $\delta^{13}C_{dolomite}$ (‰, VPDB, 7-µm spot size, yellow circles) data points measured from this domain. Error bars represent two standard deviations. Measured $\delta^{13}C_{carb}$ of micro-drilled powders (~800-µm spot size, blue triangle) by GS-IRMS is also plotted. Data source: SIMS data (this study); GS-IRMS data (Cui et al., 2017). Abbreviations: BSE, backscattered electron; Cal, calcite; CL, cathodoluminescence; Dol, dolomite; GS-IRMS, gas source-isotope ratio mass spectrometry; MDAC, methane-derived authigenic calcite; Qz, quartz; SE, secondary electron; SEM, scanning electron microscope.

4.3. SIMS $\delta^{13}C_{carb}$ analysis

In situ $\delta^{13}C_{carb}$ analysis of both calcite and dolomite was conducted on a CAMECA IMS 1280 at the Wisconsin Secondary Ion Mass Spectrometer (WiscSIMS) Laboratory, Department of Geoscience, University of Wisconsin–Madison. During SIMS analysis, carbon stable isotopes (^{12}C, ^{13}C) were measured with a 7-µm-diameter beam size. The WiscSIMS reference material UWC3 calcite was used as a running standard (Fig. A4) (Kozdon et al., 2009; Valley and Kita, 2009; Śliwiński et al., 2016a). Each group of 10–15 sample analyses was bracketed by eight analyses of UWC3. Carbon isotope ratios are reported in standard per mil (‰) notation relative to VPDB, calculated as $\delta^{13}C_{sample} = [(^{13}C/^{12}C)_{sample} / (^{13}C/^{12}C)_{VPDB} - 1] \times 1000$. The spot-to-spot reproducibility of $\delta^{13}C_{carb}$ values, calculated from all bracketing analyses on UWC3, is ± 1.1‰ (2SD, 7 µm spot size). All raw and corrected SIMS data are reported in the online supplementary materials.

After SIMS analysis of dolomites, Fe concentration (Fe# = molar ratio of Fe/[Fe + Mg]) adjacent to each SIMS pit was measured by EPMA to correct the composition-specific instrumental mass fractionation (IMF or bias) of each SIMS $\delta^{13}C_{carb}$ analysis. A suite of standards along the dolomite–ankerite series were analyzed at the beginning of each session and used to generate a calibration curve relative to the dolomite

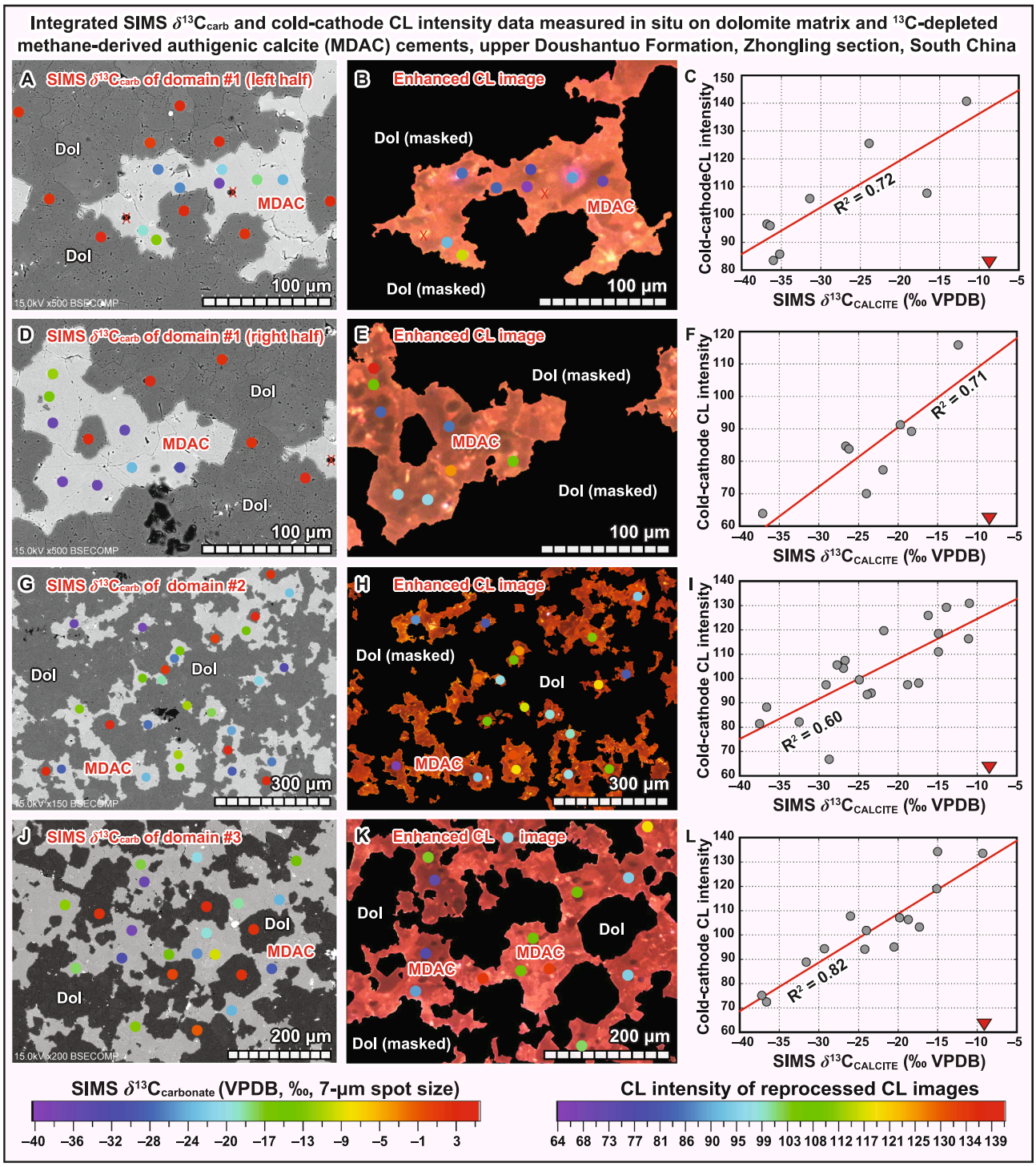

Fig. 12. SEM-BSE image (left) of four individual SIMS domains, cold-cathode CL image (middle, with dolomite masked), and cross plots (right) of integrated SIMS $\delta^{13}C_{calcite}$ and cold-cathode CL intensity data measured in situ on methane-derived authigenic calcite (MDAC) cements, upper Doushantuo Formation, Zhongling section, South China. For a better visual effect, the size of color dots is larger than the actual size of SIMS spots (i.e., 7 μm in diameter). SIMS spots with abnormal analytical signals are marked by red cross. Only calcite was analyzed for CL intensity. Triangles in the cross plots represent $\delta^{13}C$ of micro-drilled powders. **(A–C)** The left half of SIMS domain #1 of SIMS epoxy mount 12ZL-49.8a. **(D–F)** The right half of SIMS domain #1 of SIMS epoxy mount 12ZL-49.8a. **(G–I)** SIMS domain #2 of SIMS epoxy mount 12ZL-49.8a. **(J–L)** SIMS domain #3 of SIMS epoxy mount 12ZL-49.8b. All the four SIMS domains have been analyzed in situ for both SIMS $\delta^{13}C_{calcite}$ and CL intensity data. Detailed descriptions of CL intensity analysis and SIMS $\delta^{13}C_{calcite}$ analysis can be found in section 4.2 and section 4.3, respectively. Note that the SIMS $\delta^{13}C_{calcite}$ values of MDAC cements largely co-vary with the cold-cathode CL intensity of areas surrounding the corresponding SIMS pits, showing clear positive correlations. The remarkable micron-scale spatial heterogeneity in both CL intensity and $\delta^{13}C_{calcite}$ is unlikely to represent that of hydrothermal fluids which typically have uniform composition, but may result from the progressive generation of calcite cements modulated by localized microbial activity (e.g., MSR, AOM) and variable mixture of seawater and methane-derived alkalinity. In other words, this CL-$\delta^{13}C_{calcite}$ covariation likely results from micron-scale carbonate authigenesis via a mixing process between a seawater endmember (represented by relatively higher calcite CL intensity and $\delta^{13}C_{calcite}$) and a methane-derived pore fluid endmember (represented by relatively lower calcite CL intensity and $\delta^{13}C_{calcite}$) near the sediment–water interface. See section 6.3 for detailed discussion. Abbreviations: CL, cathodoluminescence; MDAC, methane-derived authigenic calcite; VPDB, Vienna Pee Dee Belemnite.

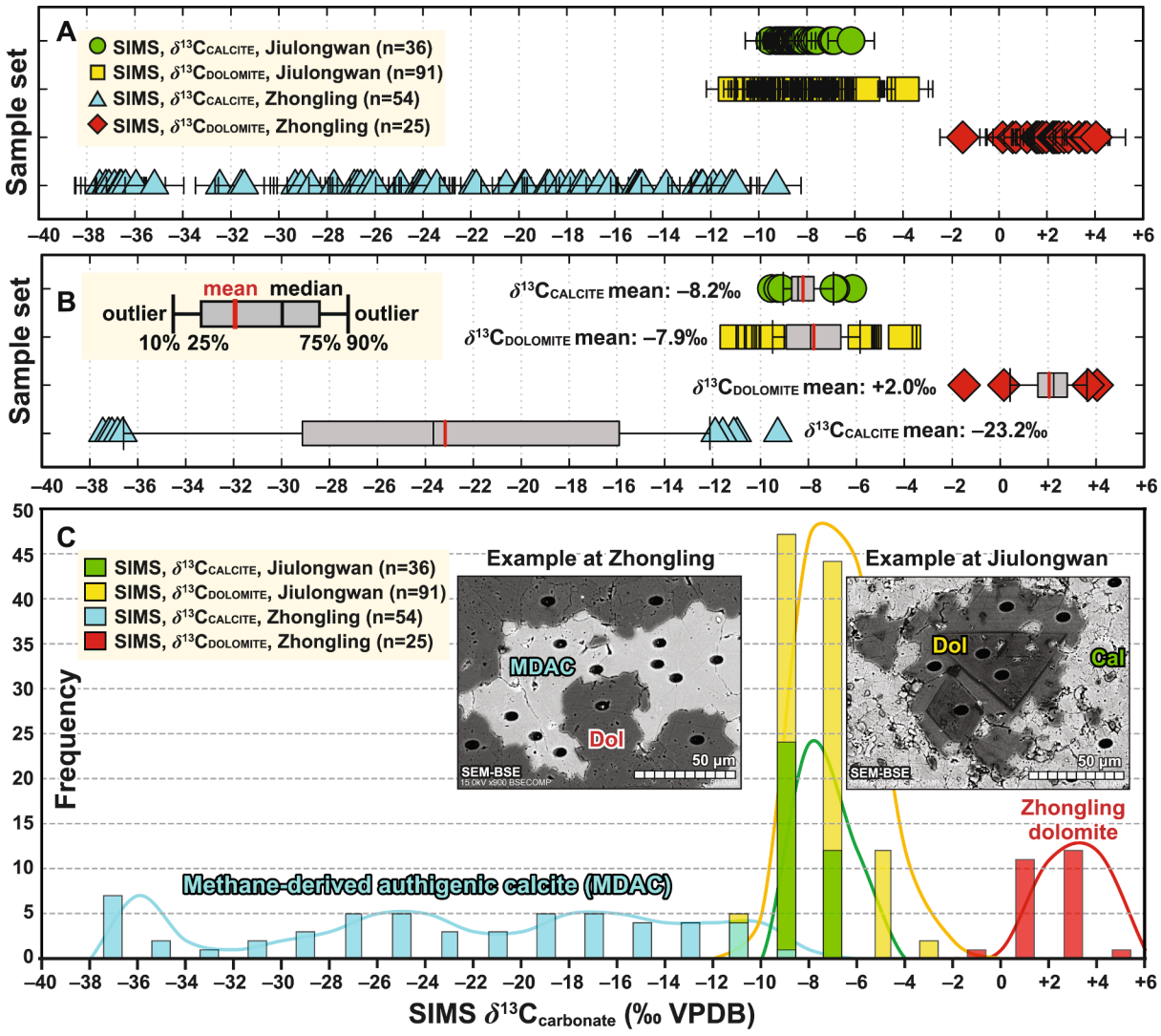

Fig. 13. Summary of SIMS $\delta^{13}C_{carb}$ data analyzed from the SE at the upper Doushantuo Formation at intra-shelf Jiulongwan section and outer-shelf shoal Zhongling section, South China. **(A)** Plot of individual SIMS $\delta^{13}C_{carb}$ values measured from dolomite and calcite at the Zhongling and Jiulongwan sections. (**B**) Box plot of the SIMS $\delta^{13}C_{carb}$ data. **(C)** Histogram of the SIMS $\delta^{13}C_{calcite}$ and $\delta^{13}C_{dolomite}$ data measured from the Jiulongwan and Zhongling sections. Inserted SEM images show typical views of the Jiulongwan and Zhongling samples, respectively. Note that these SIMS $\delta^{13}C_{carb}$ data show two important features: (i) In strong contrast with the Jiulongwan SIMS data that show a relatively narrower range (i.e., $\delta^{13}C_{carb}$ from –11.2 to –3.8‰, n = 127), the new SIMS results of Zhongling samples reveal a much wider range (i.e., $\delta^{13}C_{carb}$ from –37.5‰ in calcite to +4.0‰ in dolomite, n = 79); (ii) The Jiulongwan SIMS $\delta^{13}C_{calcite}$ and $\delta^{13}C_{dolomite}$ data largely overlap, while the Zhongling SIMS $\delta^{13}C_{calcite}$ and $\delta^{13}C_{dolomite}$ data reveal two distinct end-members. Data Source: Jiulongwan SIMS data (Cui et al., 2021); Zhongling SIMS data (this study). SEM images of all the SIMS spots analyzed in this study can be found in the online supplementary materials. Abbreviations: Cal, calcite; Dol, dolomite; MDAC, methane-derived authigenic calcite; SIMS, secondary ion mass spectrometry.

standard UW6220 (Fig. A5) (Śliwiński et al., 2016a). EPMA data show that the Zhongling calcite is very low in Fe, Mn, and Mg concentration, with average values of $MgCO_3$ = 1.08 mol% (n = 52, Table 3) and $FeCO_3$, $MnCO_3$ below detection limits. Therefore, the SIMS $\delta^{13}C_{carb}$ data analyzed from Zhongling calcite were corrected for IMF using data from UWC3 (2.96 mol % $MgCO_3$). All raw and corrected SIMS data, EPMA data are reported in the online supplementary materials.

SIMS calcite standard UWC3 was analyzed at least four times before and after every 10 to 15 measurements of unknowns to monitor running conditions. The $\delta^{13}C_{carb}$ values of UWC3 by SIMS analysis show highly consistent values (Fig. A4; 2SD = 1.1‰), suggesting steady running conditions. Cross plots of SIMS $\delta^{13}C_{carb}$ values vs. Fe, Mn, and Mg concentration data show no clear correlation (Fig. A6).

4.4. SEM imaging

After SIMS analysis, the gold coating was removed and replaced with an iridium coating for imaging by Scanning Electron Microscope (SEM) coupled with Energy-Dispersive Spectroscopy (EDS) in the Ray and Mary Wilcox SEM Laboratory, Department of Geoscience, University of Wisconsin–Madison. BSE images of samples were acquired with a Hitachi S3400 VP SEM with EDS using a Thermo Fisher thin window detector. SEM images were acquired using an accelerating voltage of 15 keV at a working distance of 10 mm. All the SIMS pits were imaged by SEM and are shown with corresponding $\delta^{13}C_{carb}$ values in the online supplementary materials.

5. Results

5.1. Petrographic SEM, CL and μXRF results

Dolomite.—SEM results show that the Zhongling dolostone consists of uniformly fine-grained (ca. 30 μm in size), homogeneous, anhedral dolomite crystals with non-planar boundaries (Figs. 7, 9–11). Although

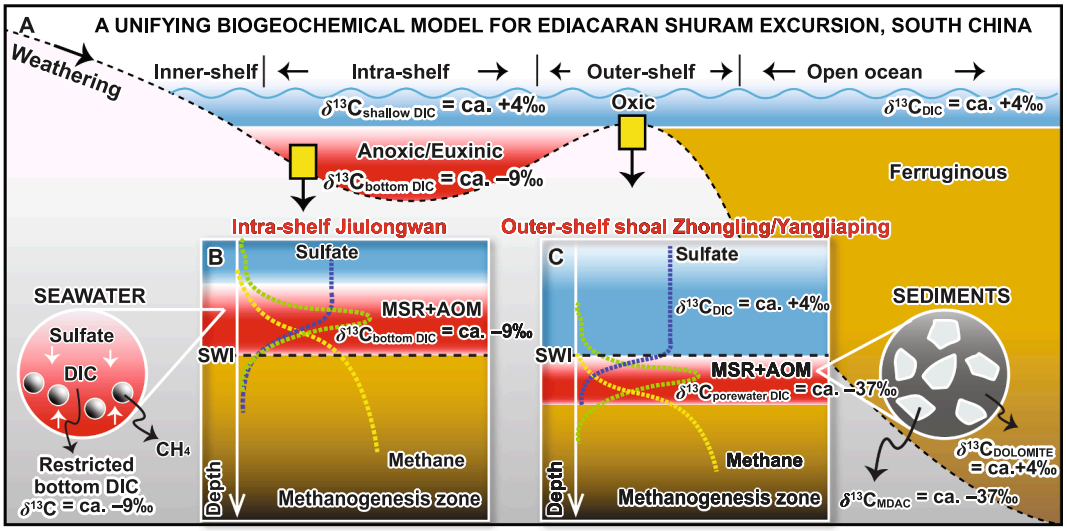

Fig. 14. Conceptual model for the heterogeneous expression of Shuram excursion (SE) in South China based on results from intra-shelf (Jiulongwan) and outer-shelf shoal (Zhongling and Yangjiaping) sections. Note that in this model, the heterogeneous SE in South China — manifest at both micron and basinal scales — was modulated by methane oxidation under variable local redox conditions. **(A)** Reconstructed redox conditions based on previous studies (Li et al., 2010; Jiang et al., 2011; Cui et al., 2015). **(B)** The Jiulongwan section is characterized by a restricted basin with microbial sulfate reduction (MSR) and anaerobic oxidation of methane (AOM) occurring in the anoxic/euxinic bottom water column. Zoomed-in circle on the left-hand side shows marine dissolved inorganic carbon (DIC) mixed with methane-derived alkalinity *above* the sediment–water interface (i.e., in the bottom water column). A strong isotopic gradient may exist from shallow ($\delta^{13}C_{shallow\ DIC}$ = ca. +4‰) to bottom ($\delta^{13}C_{bottom\ DIC}$ = ca. –9‰) water column in the restricted intra-shelf basin. **(C)** At the outer-shelf shoal Zhongling and Yangjiaping sections, deposition occurred in a more oxygenated marine shelf environment, with sulfate-methane transition zone (SMTZ) located within shallow marine sediments. The $\delta^{13}C$ of seawater at Zhongling and Yangjiaping represents open ocean DIC signal ($\delta^{13}C_{seawater\ DIC}$ = ca. +4‰), while the $\delta^{13}C$ of porewater is characterized by extremely negative and variant values ($\delta^{13}C_{porewater\ DIC}$ down to ca. –37‰). Zoomed-in circle on the right-hand side shows dolomicrite matrix and *syn*-depositional MDAC cements *below* the sediment–water interface (i.e., within pore space of shallow marine sediments). See detailed discussion in Section 6.3. Abbreviations: AOM, anaerobic oxidation of methane; DIC, dissolved inorganic carbon; MDAC, methane-derived authigenic calcite; MSR, microbial sulfate reduction; SMTZ, sulfate-methane transition zone; SWI, sediment–water interface.

the Zhongling dolomite matrix appears to be homogeneous under the SEM, it shows remarkable zoning under CL. Notably, the Zhongling dolomite shows distinct generations of yellow-green and red luminescence (Fig. 6; 9–11; online supplementary materials). In addition, the CL results also reveal many hexagonal crystals in the Zhongling dolomite matrix (Fig. 6D–N), which appear similar to the recently published vaterite crystals in the Mono Lake, California, USA (Scheller et al., 2021).

Calcite.—In contrast, the MDAC cement within the dolomite matrix typically reveals inclusion-free, sparry textures (Figs. 5, 7, 9–11), and dull luminescence (Fig. 6). It is notable that the BSE images of MDAC cements is generally light and homogeneous, which is consistent with the overall low Fe and Mn contents (see Section 5.4). That being said, we also investigated a few areas of the MDAC cements by CL and found subtle differences in brightness under both cold- and hot-cathode CL (see online supplementary materials). Four individual areas have been analyzed in situ for both SIMS $\delta^{13}C_{calcite}$ and CL intensity (Fig. 12). It is revealed that the SIMS $\delta^{13}C_{carb}$ values of MDAC cements largely co-vary with the CL intensity near SIMS pits, showing clear positive correlations (Fig. 12).

Quartz.—Trace amounts of authigenic quartz cement have also been found in the MDAC-rich laminae (Fig. 4D–E, 7D–I). The quartz crystals have euhedral shape and distinct terminations (Fig. 7D–I). It is notable that authigenic quartz rims have previously been reported surrounding many authigenic calcite nodules, which are interpreted as resulting from early diagenesis (Cui et al., 2017; Cui et al., 2022). We regard that the trace amount of authigenic quartz cements (Fig. 7D–I) in the MDAC-rich laminae probably has the same origin.

5.2. Prior $\delta^{13}C_{carb}$ and XRD data from micro-drilled powders

The focus of this study is SIMS $\delta^{13}C_{carb}$ analysis of μm-scale MDAC cement and the associated dolomite matrix from a previously studied sample 12ZL-49.8 (upper Doushantuo Formation, Zhongling section). Published $\delta^{13}C_{carb}$ and XRD results based on micro-drilled powders of the same sample (Cui et al., 2017) are also presented below in order to provide a more complete context for the new SIMS data.

Micro-XRF and optical petrographic results of sample 12ZL-49.8 (Figs. 4, 5; Table 2) show that the Zhongling dolostone consists of alternating laminations between dolomite-dominated laminae (with dolomite up to 99.8%) and authigenic-calcite-rich laminae (with calcite up to 39.1%). Integrated with the previously published $\delta^{13}C_{carb}$ and XRD data based on micro-drilled powders (Cui et al., 2017), it is revealed that the dolomite-dominated laminae typically show positive $\delta^{13}C_{micro\text{-}drilled}$ values, whereas the authigenic-calcite-rich laminae typically show more negative $\delta^{13}C_{micro\text{-}drilled}$ values (Fig. 4A; Table 2). Notably, a pure calcite nodule in the bottom of the slab shows a $\delta^{13}C_{micro\text{-}drilled}$ value of –34.1‰ VPDB (Fig. 4A).

The $\delta^{13}C_{carb}$ and XRD data based on micro-drilled powders indicate that the mixing of dolomite matrix with μm-scale authigenic calcite cements during micro-drilling can lower the overall $\delta^{13}C_{carb}$ values of the micro-drilled powders in conventional analysis by gas-source isotope ratio mass spectrometer (GS-IRMS). It is important to recognize that the MDAC cements consist of calcite crystals typically tens to hundreds μm in size, which is considerably smaller than the micro-drill pits that are 800 μm in diameter. Therefore, the micro-drilling technique cannot separate the dolomite matrix and the finely intermixed calcite cement. Consequently, the previously published $\delta^{13}C_{micro\text{-}drilled}$ data reflect mixed signals of both dolomite and calcite. In order to better constrain the isotopic composition of authigenic calcite cement, in situ analysis by SIMS is required (see the next section).

5.3. SIMS $\delta^{13}C_{carb}$ results

The new SIMS $\delta^{13}C_{carb}$ data (n = 79) show a wide range in compositions, from a nadir of –37.5‰ in the authigenic calcite cement to +4‰

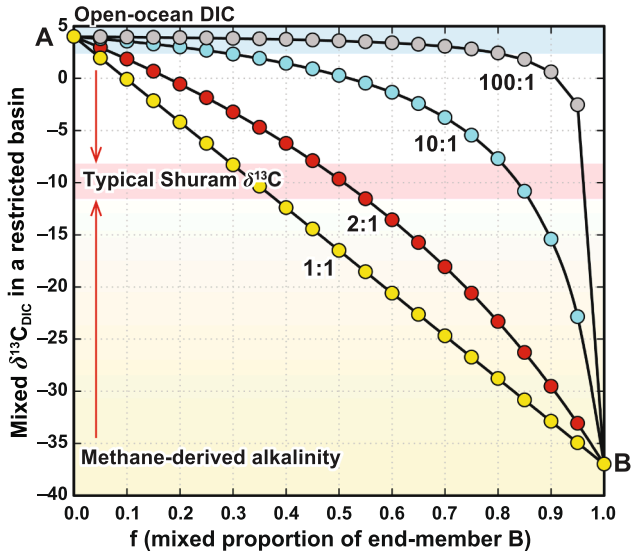

Fig. 15. A two-component fluid-mixing model to address variability of $\delta^{13}C$ in the upper Doushantuo Formation, South China. The isotopic constraints of these two end-members are based on empirical evidence in this SIMS study. End-member A represents dissolved inorganic carbon (DIC) in open marine environment of the Ediacaran ocean ($\delta^{13}C_{open\ marine\ DIC} = +4‰$, approximately the highest SIMS $\delta^{13}C$ value of Zhongling dolomite), whereas end-member B represents a fluid source that is rich in methane-derived alkalinity ($\delta^{13}C_{methane\text{-}rich\ alkalinity} = -37‰$, approximately the lowest SIMS $\delta^{13}C$ value of Zhongling MDAC cements). The X-axis represents molar mixing proportion of end-member B (i.e., rich in methane-derived alkalinity). The Y-axis represents the $\delta^{13}C$ values of mixed DIC in a restricted basin. The ratios in the panel represent DIC concentration in end-member A relative to end-member B. When the DIC concentrations in the two components are equal (1:1), a traditional linear mixing is predicted. As one component increases in relative concentration (from 1:1 to 2:1, 10:1, 100:1 in the figure), the mixing array becomes hyperbolic. Abbreviation: DIC, dissolved inorganic carbon.

in the dolomite matrix. The Zhongling dolomite matrix preserves mostly positive values (mean +2.0‰, n = 25, 2SD = 2.3‰), whereas the Zhongling authigenic calcite cement shows extremely negative values down to –37.5‰ (mean –23.2‰, n = 54, 2SD = 16.1‰) (Table 5).

It is notable that the new SIMS data reveal remarkable micron-scale spatial heterogeneity of $\delta^{13}C_{carb}$ in MDAC cement (SIMS data from –37.5 to –9.3, 2SD = 16.1‰, n = 54). In some cases, the $\delta^{13}C_{carb}$ values vary up to ca. 20‰ over ~20 μm (from –36.0 to –16.6‰ in calcite, Fig. 9A; from –37.1 to –18.3‰ in calcite, Fig. 9A), or up to ca. 39‰ over ~30 μm (from –36.0‰ in calcite to +2.7‰ in dolomite, Fig. 9A).

5.4. EPMA results

EPMA results of dolomite and calcite in sample 12ZL-49.8 show Fe and Mn contents generally below detection limits (Tables 3, 4), suggesting very low concentrations. Therefore, cross plots of Fe and Mn content vs. SIMS $\delta^{13}C_{carb}$ data show no clear correlations (Fig. A6).

6. Discussion

6.1. Comparison of the SE between intra- and outer-shelf sections

The new SIMS-SEM data in this study allow a comparison of the upper Doushantuo Formation at intra-shelf Jiulongwan and outer-shelf shoal Zhongling sections. These two sections reveal distinct characteristics in petrography, elemental and isotopic compositions. We summarize these below.

6.1.1. Distinct petrographic features

The SE-equivalent EN3/DOUNCE interval at Jiulongwan largely consists of alternating dolomitic limestone and dolostone. The dolomitic limestone consists of a matrix of calcite microspar (ca. 5–10 μm in size); disseminated, zoned dolomite crystals are up to 100 μm and account for < 10% by volume based on petrographic observations (Cui et al., 2021). Thin dolostone layers have also been found in the lower EN3/DOUNCE interval that consist mostly of euhedral to subhedral dolomite crystals under SEM (Cui et al., 2021).

In contrast, the upper Doushantuo Formation at Zhongling mostly consists of dolostone and phosphorite. Notably, the Zhongling SIMS samples investigated in this study (i.e., 12ZL-49.8a, 12ZL-49.8b) show distinct laminae that are different in the percentage of authigenic calcite cements (Fig. 5). The dolomite-dominated laminae show homogeneous dolomite crystals with distinct yellow-green and red luminesce under CL (Fig. 6). Alternating with the dolomite-dominated laminae are laminae that show a greater amount of authigenic calcite cements and a trace amount of authigenic quartz (Figs. 5, 7, A1, A2). These authigenic calcite cements typically formed along the sedimentary beddings (Figs. 4, 5A), suggesting a *syn*-depositional origin.

The yellow-green luminescence of Zhongling dolomite (Fig. 6) appears enigmatic. Although green luminescence is common in aragonite (Sommer, 1972; Lenz and Götze, 2011; Götze, 2012; Barbin, 2013), such luminescence has been rarely reported for dolomite (Gillhaus et al., 2010; Hood and Wallace, 2012; Hood et al., 2016). It has been proposed that green luminescence in dolomite may result from the presence of Mn^{2+} in the Ca^{2+} position within the crystal lattice, which may be formed during early dolomitization under a rapid rate of precipitation in an evaporative environment (El Ali et al., 1993; Gillhaus et al., 2010). The above interpretation for green luminescence in dolomite is consistent with our model of an outer-shelf shoal environment for the Zhongling section.

It is also notable that the CL results of Zhongling dolomite matrix often show hexagonal crystal shapes (Fig. 6D–N), which appear to be very similar to the recently published vaterite crystals from the Pleistocene tufas in the Mono Lake, California, USA (Scheller et al., 2021). These hexagonal crystals, therefore, indicate a vaterite or aragonite precursor for the Zhongling dolomite, which likely formed in the water column or during very early diagenesis.

Taken together, dolomite crystals in the studied Jiulongwan and Zhongling SIMS samples reveal very different paragenetic history. The Zhongling samples have a relatively fine-grained (ca. 30 μm) dolomite matrix (Figs. 5–7), and it is interpreted as a nearly primary, *syn*-depositional phase. In contrast, dolomite crystals in the Jiulongwan samples are either large (ca. 100 μm) recrystallized crystals in dolostone samples or zoned, disseminated crystals (up to 100 μm) in limestone samples (Cui et al., 2021); these are interpreted as later diagenetic phases.

6.1.2. Distinct elemental compositions

EPMA data of the Jiulongwan EN3/DOUNCE samples show a relatively wide range of Fe and Mn contents, with $FeCO_3$ values between 0 and 8 mol%, and $MnCO_3$ values between 0 and 0.12 mol% (Fig. A6) (Cui et al., 2021). In contrast, the EPMA data of the Zhongling samples show Fe and Mn contents mostly below detection limits (Fig. A6). The higher Fe and Mn contents of the coarse-grained Jiulongwan dolomite textures likely result from post-depositional dolomitization of preexisting calcite. The overall low Fe and Mn contents (i.e., mostly below detection limits by EPMA) measured from MDAC cements at Zhongling argue against the possibility of a late diagenetic origin.

It is worth mentioning that MDAC cements have also been reported from the post-Marinoan cap carbonates in the Three Gorges area. The origin of those MDAC veins or cements within cap carbonates have been a matter of debate (Jiang et al., 2003; Jiang et al., 2006; Wang et al., 2008; Bristow et al., 2011; Lin et al., 2011; Peng et al., 2015; Zhou et al., 2016; Wang et al., 2017b; Cui et al., 2019; Bao et al., 2021). Notably, the MDACs in cap carbonates are often remarkably rich in Mn and Fe

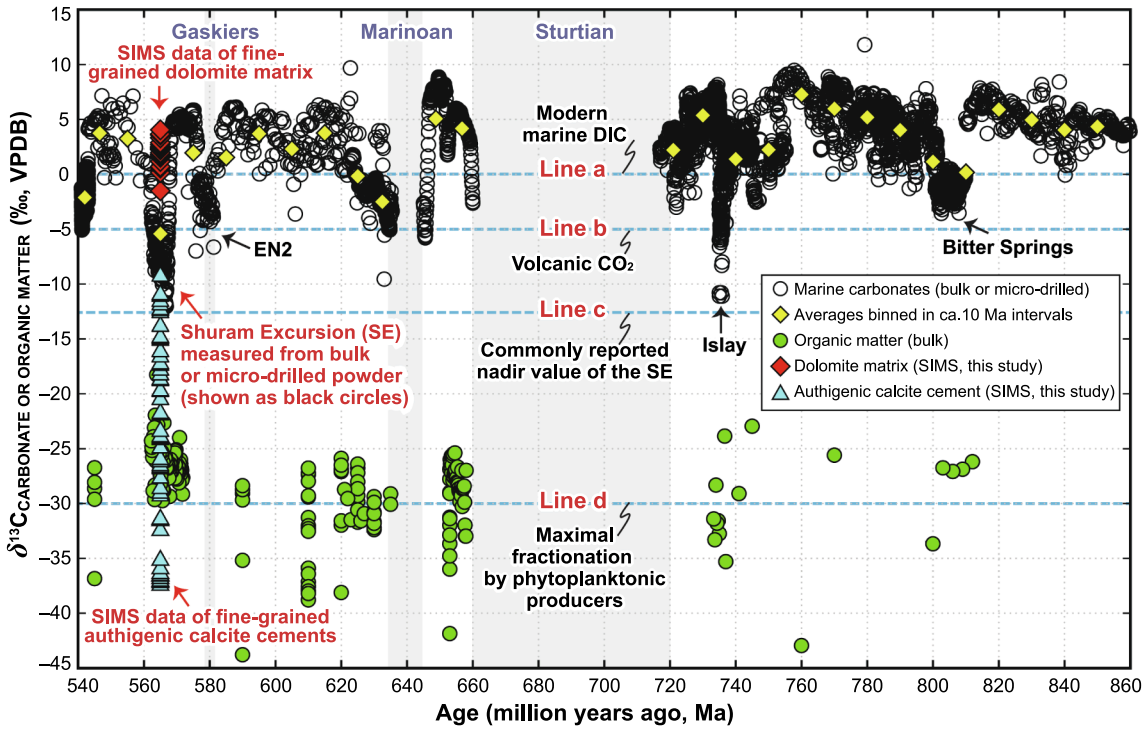

Fig. 16. Time-series $\delta^{13}C$ values from 860 to 540 Ma. The data were measured from marine carbonate (empty black circle), organic matter (green filled circle). Yellow diamonds represent $\delta^{13}C_{carb}$ averages binned in ca. 10 million-year intervals. SIMS $\delta^{13}C$ data measured from both fine-grained dolomite matrix (red diamond) and μm-scale authigenic calcite cements (cyan triangle) of the upper Doushantuo Formation at Zhongling are also plotted. The Sturtian, Marinoan, and Gaskiers glaciations are labelled as gray bands. Four horizontal blue dash lines a, b, c, and d represent $\delta^{13}C$ of modern marine DIC, putative input value of degassed volcanic CO_2, commonly reported nadir value of the SE, and organic matter with maximal fractionation of carbon isotopes by phytoplanktonic producers, respectively. Note that published $\delta^{13}C_{carb}$ profile is largely based on the measurement of marine carbonates that have been widely assumed to represent DIC of global open oceans; whether those measured marine carbonates were formed in restricted basins or incorporated isotopically distinct authigenic carbonate cements remains largely untested. Data source: $\delta^{13}C$ data of bulk or micro-drilled carbonate, organic matter, averages binned in ca. 10 Ma intervals (Canfield et al., 2020); SIMS $\delta^{13}C$ data of fine-grained dolomite matrix (this study); SIMS data of μm-scale authigenic calcite cement (this study); horizontal blue dash line a and line b (Kump and Arthur, 1999); horizontal blue dash line c (Grotzinger et al., 2011; Busch et al., 2022); horizontal blue dash line d (Hayes et al., 1999; Kump and Arthur, 1999); age constrains of the Sturtian, Marinoan, and Gaskiers glaciations (Rooney et al., 2015; Pu et al., 2016); age constrains of the SE (Canfield et al., 2020; Rooney et al., 2020; Yang et al., 2021). Abbreviations: DIC, dissolved inorganic carbon; EN, Ediacaran negative excursion; SE, Shuram excursion; VPDB, Vienna Pee Dee Belemnite.

(Sawaki et al., 2010; Bristow et al., 2011; Cui et al., 2019), which is in strong contrast with the MDAC cements in this study (with both Fe and Mn mostly below detection limits by EPMA, Fig. A6). The different sedimentological, stratigraphic, and geochemical characteristics of MDACs in the base and the upper part of the Doushantuo Formation suggest that the fluid sources of these two levels of MDACs are vastly different.

6.1.3. *μm-scale heterogeneity in SIMS $\delta^{13}C_{carb}$ and CL intensity*

SIMS $\delta^{13}C_{carb}$ results of the SE calcite and dolomite from Jiulongwan and Zhongling show distinct ranges of values (Figs. 8, 13; Table 5). The Jiulongwan SIMS $\delta^{13}C_{carb}$ data preserve values spanning from –9.5 to –6.2‰ (mean –8.2‰, n = 36, 2SD = 1.5‰) for calcite microspar and from –11.2 to –3.8‰ (mean –7.8‰, n = 91, 2SD = 2.9) for dolomite (Cui et al., 2021). In striking contrast, the new Zhongling SIMS $\delta^{13}C_{carb}$ data (n = 79) record a much wider range (from –37.5‰ to +4‰) in authigenic calcite cements (mean –23.2‰, n = 54, 2SD = 16.1‰) and dolomite matrix (mean +2.0‰, n = 25, 2SD = 2.3‰). For the first time, the new SIMS data reveal remarkable micron-scale spatial heterogeneity in $\delta^{13}C_{carb}$ compositions (Figs. 9–12). In this study, we propose a conceptual model that aims to explain the distinct $\delta^{13}C_{carb}$ data at both sections (see Section 6.3 for details).

Integrated analysis of SIMS $\delta^{13}C_{calcite}$ and CL intensity for four individual areas of MDAC cements reveals that the $\delta^{13}C_{calcite}$ values largely co-vary with the CL intensity of areas surrounding SIMS pits, with clear positive correlations (Fig. 12).This spatial heterogeneity unlikely represents that of hydrothermal fluids which typically have uniform compositions, but may result from the progressive generation of cements modulated by localized microbial activity and variable mixture of seawater and methane-derived alkalinity. Here we propose that the CL-$\delta^{13}C_{calcite}$ covariation likely results from micron-scale carbonate authigenesis via a mixing process between a seawater endmember (represented by relatively higher calcite CL intensity and $\delta^{13}C_{calcite}$) and a methane-derived pore fluid endmember (represented by relatively lower calcite CL intensity and $\delta^{13}C_{calcite}$) near the sediment–water interface. Detailed mechanism remains unclear about why lower-$\delta^{13}C$ calcite typically shows lower CL intensity. Considering that CL intensity in carbonate is typically controlled by the interplay between Mn^{2+} and Fe^{2+} substitution of Ca^{2+} in various redox conditions (Frank et al., 1982; Mason, 1987; Barnaby and Rimstidt, 1989; El Ali et al., 1993; Gillhaus et al., 2000; Pagel et al., 2000), it is speculated here that a mineralogical and redox control on elemental partition of Fe^{2+} and Mn^{2+} may have played a role during early authigenesis. However, the CL intensity data cannot be directly translated to Fe and Mn concentrations, and most of the MDAC cements yield Fe and Mn concentration below the detection limit of EPMA (Table 3). Therefore, a more quantitative interpretation is currently not feasible in this study.

6.2. *Testing the role of authigenic carbonate during the Shuram excursion*

Our new SIMS results allow us to test the two hypotheses based on the revised triple-sink carbon cycle model (Fig. 1F; see also Section 2.3 for details).

6.2.1. Testing hypothesis 1 (i.e., global authigenesis of ^{13}C-enriched carbonate)

Hypothesis 1 invokes large-scale mineralization of ^{13}C-enriched authigenic carbonate that could drive the $\delta^{13}C_{DIC}$ of platform environment towards much lower values (Laakso and Schrag, 2020). This hypothesis predicts the occurrence of ^{13}C-enriched authigenic carbonate in SE-equivalent sections with less negative (>–9‰) bulk $\delta^{13}C_{carb}$ values (Laakso and Schrag, 2020). The upper Doushantuo Formation at Zhongling (Fig. 1C) is an ideal target to test this prediction. Here in this study, we have not found the hypothesized ^{13}C-enriched authigenic carbonate from the upper Doushantuo Formation at Zhongling. The highest $\delta^{13}C_{carb}$ value of +4‰ at Zhongling was analyzed from fine-grained dolomite matrix (Fig. 9), which we interpret as reflecting open ocean DIC signals; in contrast, authigenic calcite cements show exclusively negative $\delta^{13}C_{carb}$ values (Fig. 13). Therefore, hypothesis 1 is not supported by this study.

Indeed, many predictable elements of this hypothesis are inconsistent with published results. First, this hypothesis predicts a significant collapse of seawater sulfate reservoir during the SE (Laakso and Schrag, 2020). However, detailed sedimentological compilation of sulfate minerals and chemostratigraphic profiles of carbonate-associated sulfate (CAS) actually reveal the opposite: seawater sulfate concentration was more likely significantly enhanced during the SE (Cui et al., 2022), which would inhibit, rather than facilitate, the hypothesized large-scale methanogenic event. Second, this hypothesis also predicts higher bulk $\delta^{13}C_{carb}$ values in deeper environment due to the hypothesized methanogenic event (Laakso and Schrag, 2020). However, basin-scale chemostratigraphy of the SE shows similarly negative or even lower bulk $\delta^{13}C_{carb}$ values in correlative sections at a deeper water depth in South China (Jiang et al., 2007; Jiang et al., 2008; Furuyama et al., 2017; Wang et al., 2017a; Wang et al., 2020) and Oman (Lee et al., 2013). Third, if the SE indeed reflects the DIC of global open oceans, one would expect to see co-variations of $\delta^{13}C_{carb}$ and $\delta^{13}C_{org}$ values. However, strong decoupling of paired carbon isotopes has been widely reported from SE sections in Oman (Fike et al., 2006; Lee et al., 2013), Australia (Calver, 2000), NW Canada (Macdonald et al., 2013), and South China (McFadden et al., 2008; Wang et al., 2016; Li et al., 2017; Wang et al., 2017a; Wang et al., 2020), which argues against global open ocean signals. Therefore, Hypothesis 1 is not supported in this study.

6.2.2. Testing hypothesis 2 (i.e., local authigenesis of ^{13}C-depleted carbonate)

Hypothesis 2 proposes that the SE may result from local authigenesis of ^{13}C-depleted carbonate (Fig. 1F); and the SE may therefore represent local-scale carbon cycle anomaly in disparate sedimentary basins. Here, the successful identification of μm-scale, ^{13}C-depleted MDAC cements by SIMS supports the occurrence of local authigenesis of ^{13}C-depleted carbonates during the SE; and different degrees of authigenesis across the basin may have led to the variable chemostratigraphic expression of bulk $\delta^{13}C_{carb}$ across the basin.

However, it is also important to recognize that whether ^{13}C-depleted authigenic carbonate also exists in other sections that record negative carbon cycle anomalies remains largely untested (Fig. 16). In South China, MDAC in the upper Doushantuo Formation has only been found from outer-shelf shoal sections (Figs. 3, 8). Notably, authigenic calcite nodules with negative $\delta^{13}C_{carb}$ values down to –20‰ have also been reported from the Mara Member of the Nama Group, southern Namibia (Kaufman et al., 2015; Cui et al., 2022), which has been proposed to be correlative with the SE (Wood et al., 2015; Xiao et al., 2016; Xiao and Narbonne, 2020; see also Yang et al., 2021 for a different view). The lack of MDAC in other SE sections might result from two reasons. First, authigenic carbonate cements are typically μm-scale (<100 μm) and therefore can easily be overlooked in outcrops. It is suggested that more SEM-SIMS studies should be actively conducted for other SE sections in order to identify MDAC cements. Second, it is possible that authigenesis of MDAC is facies- and redox-dependent, therefore is limited to a local or regional scale. Here in the case of the Doushantuo Formation, the fact that only outer-shelf shoal sections have been found to be rich in MDAC may reflect a close link between facies/redox variability and authigenic mineralization. Whether our conceptual model (Fig. 14) is also applicable to other Ediacaran basins or other carbon isotope anomalies in Earth history requires more integrative studies that incorporate sedimentology, diagenesis, petrography, and geochemistry.

In practice, it remains challenging to identify authigenic carbonate in deep-time carbonate record. The distinction between depositional carbonate and authigenic carbonate could be nuanced, especially when the latter formed during *syn*-deposition or very early diagenesis around the sediment–water interface. The ambiguity of the term "authigenic carbonate" has recently been brought up in a review paper by Fantle et al. (2020), who wrote that "authigenic constituents are a broad and ambiguous category: Whereas authigenic carbonates are often depicted as cements that grow in sedimentary pore spaces, technically all forms of recrystallization constitute in situ formation and could be considered to be authigenic". In the case of the EN3/DOUNCE interval at Jiulongwan, detailed SIMS and SEM investigation shows that limestones are dominated by fine-grained calcite microspars (ca. 5–10 μm) that lack any texture indicative of sediment transport and have clearly been neomorphosed/recrystallized (Cui et al., 2021). These petrographic features are not diagnostic as to whether the EN3/DOUNCE carbonates are depositional, or authigenic. Currently, an authigenic origin for the Jiulongwan EN3/DOUNCE carbonates cannot be ruled out. It remains possible that EN3/DOUNCE results from authigenic alteration of pre-existing low-δ^{13}C carbonates, or precipitation of low-δ^{13}C carbonates during authigenesis. In light of the occurrence of MDAC at the Zhongling section, we suggest that contemporary mixing between seawater DIC and methane-derived alkalinity in the bottom water column (Fig. 14B) could possibly explain the largely homogeneous and muted isotopic signature as well as uniform petrographic feature at Jiulongwan.

In summary, our SIMS results echo the scenario of local-scale authigenesis during the SE, and different degrees of authigenesis across the basin may have caused the variable chemostratigraphic expression of bulk $\delta^{13}C_{carb}$ across the basin. However, ambiguity still remains regarding how to identify authigenic carbonate on a micron scale and whether typical SE is composed of authigenic carbonate.

6.3. A unifying biogeochemical model for heterogeneous SE in South China

6.3.1. Methane oxidation in porewater vs. seawater

Viewed in detailed petrographic and stratigraphic context, we propose that the SIMS $\delta^{13}C_{carb}$ data at Zhongling and Jiulongwan reflect a wide spectrum of sedimentary processes that affect local $\delta^{13}C_{carb}$ compositions (Fig. 14). In the shallow outer-shelf shoal environment, the mostly positive SIMS $\delta^{13}C_{carb}$ values of Zhongling dolomite (ranging between +0.2 and +4.0‰, with a single outlier at –1.5‰) likely represent open marine DIC signals, while the much more negative and variable SIMS $\delta^{13}C_{carb}$values (–37.5 to –9.3‰) recorded in MDAC cements were likely influenced by microbial sulfate reduction (MSR) and anaerobic oxidation of methane (AOM) *below* the sediment–water interface (i.e., within the pore space of shallow marine sediments). Due to diffusional constraints in marine sediments, the highly ^{13}C-depleted methane-derived alkalinity that accumulated in pore fluids could not be fully mixed with seawater, and therefore left a isotopic fingerprint in MDAC cements or nodules (Fig. 14C).

In the intra-shelf environment (i.e., Jiulongwan section), we propose that the much narrower range of $\delta^{13}C_{carb}$ values (mean ca. –9‰) in the EN3/DOUNCE interval likely resulted from a more thorough mixing of bottom seawater DIC (i.e., +4‰) with methane-derived alkalinity *above* the sediment–water interface (i.e., within the water column) (Fig. 14B). In this view, methane flux from the deeper methanogenesis zone of marine sediments escaped to the seafloor, and was oxidized by seawater sulfate, which consequently decreased the bottom seawater $\delta^{13}C_{DIC}$ of

restricted intra-shelf basins. Based on a simple two-endmember mixing calculation, mixing seawater DIC ($\delta^{13}C_{DIC}$ = +4‰) with ca. 35% of methane-derived alkalinity ($\delta^{13}C$ = –37‰) can generate Shuram-like values of ca. –10‰ (Fig. 15).

Taken together, the above conceptual model shows that the $\delta^{13}C_{carb}$ variability at Jiulongwan and Zhongling was caused by two different depositional processes (Fig. 14). The Jiulongwan EN3/DOUNCE interval results from the mixing of bottom seawater DIC with methane-derived alkalinity *above* the seafloor of a restricted basin (Fig. 14B), whereas the much larger variation in $\delta^{13}C_{carb}$ at Zhongling and Yangjiaping reflects local authigenic mineralization of MDAC within the pore space of shallow marine sediments (Fig. 14C), which is resolved by SIMS in this study.

Then what controlled this basin-scale $\delta^{13}C_{carb}$ heterogeneity between intra-shelf and outer-shelf shoal sections? We suggest that the above distinction between Jiulongwan and Zhongling may result from variable local redox conditions across the basin. Previous studies suggest that the Jiulongwan section was deposited in an overall anoxic intra-shelf environment with intermittent euxinic episodes (Li et al., 2010), while the Zhongling section was deposited in a shallower, oxygenated outer-shelf shoal environment (Cui et al., 2015) (Fig. 14A; see Section 3.3 for details). In this scenario, anoxia/euxinia with a continuous supply of sulfate from the continent may have facilitated MSR and AOM in the water column, leading to a steady and consistent $\delta^{13}C_{bottom\ DIC}$ excursion of ca. –9‰ (Fig. 14B). In contrast, the more oxidizing conditions at Zhongling and Yangjiaping may have driven MSR, AOM, and the sulfate-methane transition zone (SMTZ) *below* the sediment–water interface (Fig. 14C), leading to strong variability of $\delta^{13}C_{porewater\ DIC}$ at a micron scale. Therefore, the different redox conditions may dictate the locations of MSR and AOM in marine environments (i.e., water column vs. pore space), leading to distinct expressions of $\delta^{13}C_{carb}$ in chemostratigraphy across the basin (i.e., narrow range of $\delta^{13}C$ values ca. –9‰ at Jiulongwan vs. highly variable $\delta^{13}C_{carb}$ values from –37.5‰ to +4.0‰ at Zhongling; Fig. 8).

6.3.2. Reinterpretation: Carbon and sulfur cycles revisited

In this study, we revisited the previously published data across the basin (Fig. 3). Notably, the Jiulongwan section shows strongly decoupled $\delta^{13}C_{carb}$ and $\delta^{13}C_{org}$ profiles in the EN3/DOUCE interval (Fig. 3A). Similar decoupling between paired $\delta^{13}C_{carb}$ and $\delta^{13}C_{org}$ has also been reported from SE sections in Oman (Fike et al., 2006; Lee et al., 2013), Australia (Calver, 2000), and NW Canada (Macdonald et al., 2013). This phenomenon has led to the hypothesis of a large dissolved organic carbon (DOC) reservoir in the Ediacaran ocean (Rothman et al., 2003; Fike et al., 2006). The overall invariant $\delta^{13}C_{org}$ was therefore thought to result from the buffering effect of this overwhelmingly large DOC reservoir (Rothman et al., 2003). However, the above hypothesis of a large DOC reservoir in the Ediacaran ocean has been increasingly challenged (Jiang et al., 2010; Johnston et al., 2012; Macdonald et al., 2013; Wang et al., 2014; Fakhraee et al., 2021). Here in the case of the upper Doushantuo Formation, closely *coupled* $\delta^{13}C_{carb}$ and $\delta^{13}C_{org}$ profiles at the inner-shelf Wangji section (Gao et al., 2019) and the outer-shelf Yangjiaping section (Fig. 3I) (Cui et al., 2015) do strongly argue against the existence of a large DOC reservoir in the depositional basin. In addition, the preservation of remarkably negative $\delta^{13}C_{org}$ values (ca. –40‰) at EN3c (Fig. 3A) is also inconsistent with a large and uniform DOC reservoir in the Ediacaran ocean. Therefore, the decoupled $\delta^{13}C_{carb}$-$\delta^{13}C_{org}$ values at Jiulongwan require a re-interpretation.

In light of the new data from Zhongling, here we propose an alternative interpretation for the $\delta^{13}C_{carb}$-$\delta^{13}C_{org}$ decoupling at Jiulongwan. Given that the $\delta^{13}C_{org}$ values at EN3a and EN3b of Jiulongwan are highly consistent with the $\delta^{13}C_{org}$ values measured from outer-shelf environments (Fig. 3A, E, I), primary productivity at Jiulongwan should occur in shallow seawater that was isotopically similar to the open ocean (i.e., $\delta^{13}C_{shallow\ DIC}$ = ca. +4‰). Therefore, to interpret the lower $\delta^{13}C_{carb}$ values (ca. –9‰) at Jiulongwan, an *exogenous* source of isotopically light carbon is required. Here, we propose that *syn*-depositional methane oxidation in the bottom water column may have caused the lower $\delta^{13}C_{carb}$ values (ca. –9‰) and also the $\delta^{13}C_{carb}$-$\delta^{13}C_{org}$ decoupling at Jiulongwan. In this scenario, shallow seawaters that host the majority of primary productivity have normal marine DIC values (i.e., $\delta^{13}C_{shallow\ DIC}$ = ca. +4‰), while the DIC around the sediment–water interface of the restricted intra-shelf basin is characterized by much lower $\delta^{13}C$ due to active methane oxidation in the bottom water column (i.e., $\delta^{13}C_{bottom\ DIC}$ = ca. –9‰) (Fig. 14). This re-interpretation (i.e., *syn*-depositional methane oxidation around the sediment–water interface) for $\delta^{13}C_{carb}$-$\delta^{13}C_{org}$ decoupling does not need to invoke an overwhelmingly large DOC reservoir in the Ediacaran ocean, and is also consistent with published bulk and SIMS $\delta^{13}C$ data across the basin (Fig. 14).

Our conceptual model for the SE in South China is also consistent with published $\delta^{34}S$ chemostratigraphy across the basin. Notably, the upper Doushantuo Formation shows much higher $\delta^{34}S_{pyrite}$ values at the Zhongling and Yangjiaping sections (mostly ca. +10 to +30‰) than at the intra-shelf Jiulongwan section (mostly ca. –15 to +10‰) (Fig. 3C, G, K). This distinct pattern in $\delta^{34}S$ chemostratigraphy has been interpreted as resulting from a concentration gradient of seawater sulfate from intra- to outer-shelf environments (Li et al., 2010). However, such a gradient appears to be inconsistent with the finding of chicken wire texture (indicative of gypsum deposition and high sulfate concentrations) at Zhongling (Cui et al., 2022). Instead, the $\delta^{34}S$ chemostratigraphy echoes our conceptual model that different redox conditions may have locally controlled the depth of MSR, AOM, and pyrite authigenesis during the SE. The more positive $\delta^{34}S_{pyrite}$ values in the outer-shelf shoal regions likely result from a much higher sedimentation rate, more oxidizing conditions in the water column, coupled with pyrite and MDAC authigenesis mostly occurring in sediment porewaters with limited diffusion of seawater sulfate. On the other hand, the much lower $\delta^{34}S_{pyrite}$ values in the intra-shelf Jiulongwan section likely result from MSR, AOM, and pyrite authigenesis occurring in the water column (Fig. 14).

6.4. Implications for the Shuram excursion

Results in this study present a challenge to the conventional view that the SE records global open-ocean $\delta^{13}C_{DIC}$ values. Instead, in light of this study, the globally recorded SE may be coupled with different degrees of authigenesis of ^{13}C-depleted carbonates around the sediment–water interface during *syn*-deposition; such an authigenic event may have been locally modulated by methane oxidation in individual basins, and synchronously driven by a common controlling factor on a global scale. The global and local drivers for the SE have been proposed to be a larger seawater sulfate input during an atmospheric oxygenation event (Kaufman et al., 2007; Li et al., 2017; Shields et al., 2019; Cui et al., 2022), a larger biological pump during deposition (Cao et al., 2020), or a marine transgression paired with enhanced evaporation and primary productivity (Busch et al., 2022).

More specifically, the heterogeneous chemostratigraphic profiles of the SE could have been caused by the confluence of various environmental factors superimposed by both local and global conditions. In anoxic/euxinic basins where methane oxidation occurs in the bottom water column, the $\delta^{13}C_{carb}$ excursion reflects well-mixed, restricted seawater DIC, and therefore is manifest as typical SE ($\delta^{13}C_{carb}$ ~–9‰) with relatively muted variations on a micron scale. At the same time, in more oxic environments where methane oxidation occurs within sediments, $\delta^{13}C_{carb}$ exhibits much greater spatial heterogeneity on the micron scale, millimeter scale, and meter scales.

The emerging view that SE may not represent global open-ocean DIC is supported by an increasing number of published studies. Our view for the SE based on the upper Doushantuo Formation in South China echoes

a study of the Wonoka Formation in South Australia, which also argues for a heterogeneous DIC reservoir in the ocean (Calver, 2000). Similarly, a recent Ca isotopes study of five SE sections across four paleocontinents suggests that the SE is a globally synchronous primary seawater phenomenon but not necessarily representative of average DIC of global open oceans (Busch et al., 2022).

The finding of $\delta^{13}C_{carb}$ signals as low as –37.5‰ in μm-scale MDAC cements by SIMS also sheds light on the source of ^{13}C-depleted carbon for the SE. Numerous hypotheses have been proposed for the sources of isotopically light carbon during the SE (Cui, 2021), among which the most widely invoked process is the oxidation of a large dissolved organic carbon (DOC) reservoir accumulated in the anoxic deep ocean (Rothman et al., 2003; Fike et al., 2006; Jiang et al., 2007; McFadden et al., 2008; Shields et al., 2019; Cheng et al., 2022), although the existence of this putative DOC reservoir has been increasingly challenged (Jiang et al., 2010; Johnston et al., 2012; Macdonald et al., 2013; Wang et al., 2014; Fakhraee et al., 2021) (see detailed discussion in Section 6.3.2). Notably, abrupt oxidation of a preexisting methane hydrate reservoir (Bjerrum and Canfield, 2011) or progressive oxidation of methane diffused from the deeper methanogenesis zone (Cui et al., 2017; Cui et al., 2022) has also been proposed for the SE; however, direct sedimentological evidence for methane oxidation has been limited. In this study, $\delta^{13}C_{carb}$ signals down to –37.5‰ are reported from μm-scale MDAC cements by SIMS (Figs. 9–12). These MDAC cements are ^{13}C-depleted and isotopically heterogeneous, representing a substantial proportion of carbonate component (i.e., ca. 30 to 40% in certain horizons based on XRD data in Fig. 4) in the upper Doushantuo Formation. If our interpretation for the MDAC cements is correct (i.e., a *syn*-depositional origin during the SE), it suggests that the process of methane oxidation could have played a significant role in the genesis of the SE. In addition, the recognition of a potentially large-scale oxidation of methane during the SE also helps solve the mass balance problem of oxidant budget for the SE (Bristow and Kennedy, 2008).

7. Conclusions

Following the recent SIMS $\delta^{13}C_{carb}$ study of the upper Doushantuo Formation at intra-shelf Jiulongwan section (Cui et al., 2021), we expand our study to the outer-shelf shoal environment (Zhongling and Yangjiaping sections). Authigenic calcite cements (Figs. A1, A2) from the upper Zhongling section was directly analyzed by SIMS in this study.

In strong contrast with the Jiulongwan SIMS data that show a relatively narrower range of $\delta^{13}C_{carb}$ (–11.2 to –3.8‰, n = 127) (Cui et al., 2021), the new SIMS results of Zhongling samples reveal a much wider range of $\delta^{13}C_{carb}$ values (from –37.5‰ in calcite to +4.0‰ in dolomite, n = 79), with remarkable micron-scale heterogeneity in $\delta^{13}C_{carb}$ compositions. Extremely negative $\delta^{13}C_{carb}$ values down to –37.5‰ in authigenic calcite cement suggest the contribution of biogenic methane. Integrated SIMS $\delta^{13}C_{carb}$ and CL results show strong heterogeneity and correlation on a micron scale, which argues against an origin of hydrothermal fluids, but may result from the progressive precipitation of calcite cements modulated by localized anaerobic microbial activity (e.g., MSR, AOM) and variable mixture of seawater and methane-derived alkalinity.

We show that the $\delta^{13}C_{carb}$ heterogeneity of SE carbonates in South China is manifest at micrometer, centimeter, and basinal scales, and is modulated by methane oxidation in variable local redox conditions. In the oxygenated outer-shelf shoal environment (i.e., the Zhongling and Yangjiaping sections), MDAC formed within shallow marine sediments via microbial sulfate reduction (MSR) and anaerobic oxidation of methane (AOM), causing strong isotopic contrast in carbonates of different generations at a micron scale (Figs. 9–12), which is resolved by SIMS in this study.

In light of our new finding at Zhongling, we propose that the typical SE (i.e., $\delta^{13}C_{carb}$ = ca. –9‰) at the intra-shelf Jiulongwan section may result from *syn*-depositional methane oxidation in bottom waters. The bottom seawater DIC of restricted intra-shelf basin was likely mixed with methane-derived alkalinity *above* the sediment–water interface (i.e., $\delta^{13}C_{bottom\ DIC}$ = ca. –9‰), leading to the formation of typical SE with stratigraphically consistent $\delta^{13}C_{carb}$ values around –9‰. Syn-depositional methane oxidation may have caused the much lower $\delta^{13}C$ in bottom seawater compared with shallow seawaters ($\delta^{13}C_{shallow\ DIC}$ = ca. 4‰) (Fig. 14). Our interpretation can well explain the strong $\delta^{13}C_{carb}$-$\delta^{13}C_{org}$ decoupling at Jiulongwan without invoking a large DOC reservoir in the ocean.

The new data in our study present a challenge to the view that the SE records global open-ocean $\delta^{13}C_{DIC}$ signals. Instead, the globally recorded SE may be coupled with different degrees of authigenesis of ^{13}C-depleted carbonates, and represents variable expressions of carbon cycle perturbations that were locally modulated by *syn*-depositional methane oxidation. An atmospheric oxygenation event in the Ediacaran Period may have set the stage for widespread delivery of sulfate to the oceans through continental weathering, and subsequently promoted methane oxidation and authigenesis around the sediment–water interface. Local environmental drivers (i.e., redox, facies, water depth) may have played a critical role in modulating the effect of methane signals. Therefore, strongly ^{13}C-depleted methane signals can either be preserved as isotopically anomalous authigenic carbonate cements within porewater, or be muted by mixing with seawater. Our study demonstrates that integrated SIMS-SEM analysis is an effective approach to assess the origin and diagenetic history of $\delta^{13}C_{carb}$ anomalies in the sedimentary record.

Contributions

HC designed research; HC and SX conducted field work at Zhongling and Yangjiaping; HC and MJS prepared SIMS samples; HC and IJO performed SIMS assisted by KK and JWV at the WiscSIMS laboratory; HC and JHF performed SEM and EPMA analyses; KK, IJO, AD, and HC corrected raw SIMS data; JMB and HC performed cold-cathode CL imaging; JMF performed hot-cathode CL imaging; JMB analyzed cold-cathode CL intensity; HC compiled and interpreted the results and wrote the manuscript with review and contributions from all coauthors. All authors contributed to discussion and manuscript revision.

Declaration of Competing Interest

The authors declare that they have no known competing financial interests or personal relationships that could have appeared to influence the work reported in this paper.

Acknowledgements

HC wants to thank Prof. Jianbo Liu (Peking University), who introduced HC the conventional carbon cycle model in his class when HC was a graduate student in Beijing back to over 10 years ago. It was Prof. Liu's course *Biogeochemistry and Biomineralization* that inspired HC to pursue a Ph.D. in geobiology and biogeochemistry abroad.

The authors thank Bil Schneider for assistance in the SEM laboratory at UW-Madison; Brian Hess, Noriko Kita, James Kern, and Maciej Śliwiński for assistance in sample preparation and SIMS analysis at UW-Madison; Huifang Xu for assistance in the microscope laboratory at UW-Madison; Steven Goderis, Niels J. de Winter, and Pim Kaskes for guidance in the μXRF laboratory at VUB; Yiheng Wu for assistance in compiling supplemental materials; Chuanming Zhou (NIGPAS) for field assistance and constructive comments; Ganqing Jiang (UNLV) and Magali Ader (IPGP) for kind discussion. This paper was handled by

Frances Westall (CNRS, Orléans) and benefits from constructive reviews by James Busch (Dartmouth), Thomas Algeo (Cincinnati), and three anonymous reviewers.

This study was supported by the NASA Astrobiology Institute (NNA13AA94A) at UW–Madison. The WiscSIMS Lab is supported by NSF (EAR–1355590, –1658823, –2004618) and UW–Madison. JWV was also supported by NSF (EAR–1524336) and DOE (DE–FG02–93ER14389). SX was supported by NASA Exobiology Program (80NSSC18K1086). HC is grateful for joint support from CIFAR (Canadian Institute for Advanced Research) "Earth 4D: Subsurface Science and Exploration" program at Université Paris Cité and University of Toronto. This paper is dedicated to Yiheng Wu and toddler Ruogu Cui, for the love, peace, and joy during the pandemic in Paris.

Appendices A1–A6

See Figs. A1–A6.

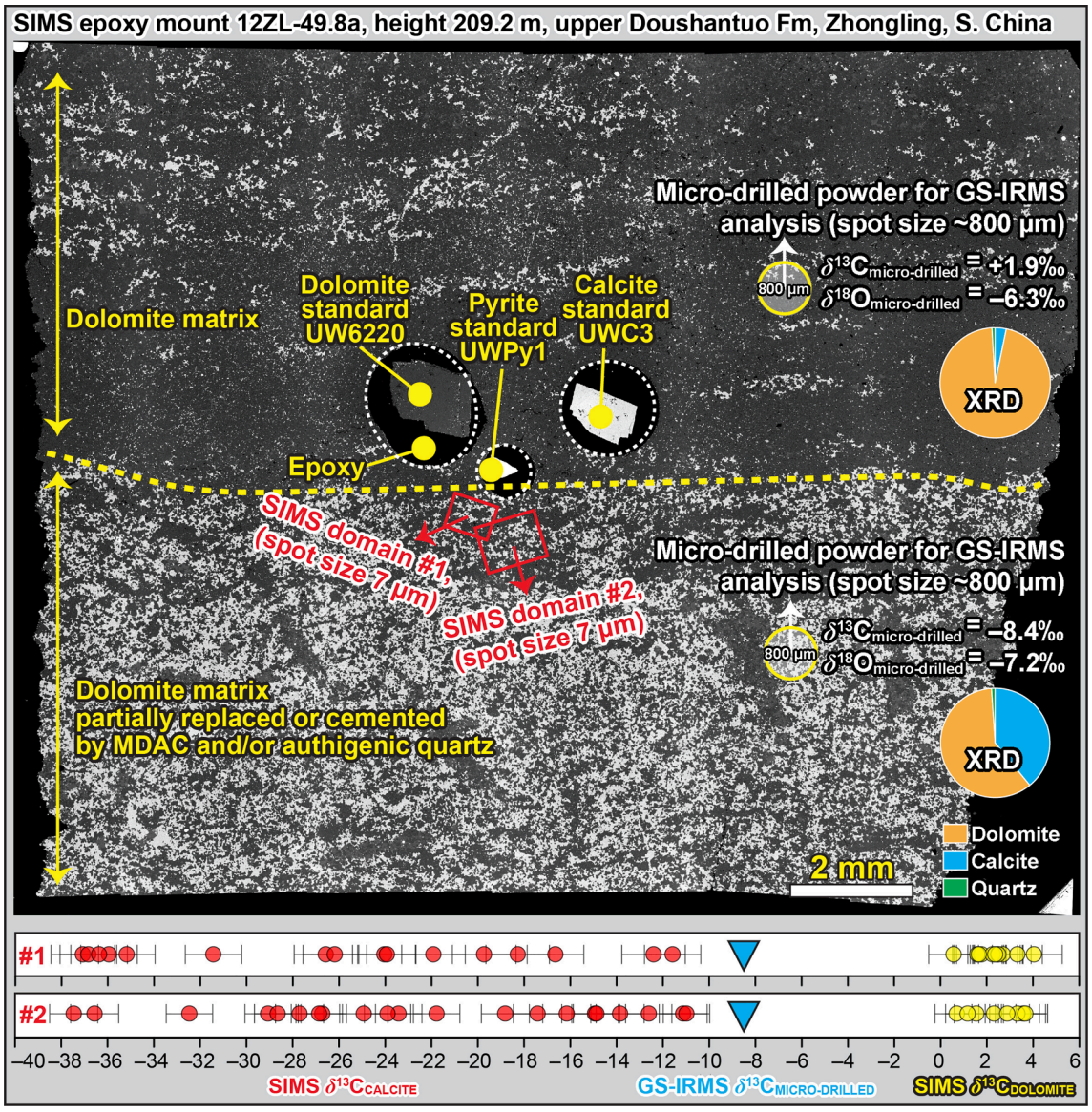

Fig. A1. Composite panorama of SIMS epoxy mount 12ZL-49.8a based on 6×6 BSE images. The SIMS $\delta^{13}C_{calcite}$ (‰, VPDB, 7-μm spot size, red circles) and $\delta^{13}C_{dolomite}$ (‰, VPDB, 7-μm spot size, yellow circles) data measured from SIMS domain #1 and domain #2 are plotted at the bottom. Error bars represent two standard deviations. Measured $\delta^{13}C_{carb}$ of micro-drilled powders (~800-μm spot size, blue triangle) by GS-IRMS is also plotted. This SIMS mount is 25 mm in diameter, with three WiscSIMS standards (calcite UWC3, dolomite UW6220, and pyrite UWPy1) mounted in the center. The upper half of this SIMS mount is dominated by fine-grained dolomite (darker under BSE), whereas the lower half shows dolomite matrix with ^{13}C-depleted, methane-derived authigenic calcite (MDAC) cements (brighter under BSE) and a trace amount of authigenic quartz. The $\delta^{13}C_{carb}$ (VPDB) and $\delta^{18}O_{carb}$ (VPDB) data of micro-drilled powders from the upper and lower halves were analyzed by conventional GS-IRMS. SIMS domains #1 and #2 (marked as two red boxes) were investigated by SEM, CL and WiscSIMS in this study. Note that the spot size of micro-drilling bit is ~800 μm, while the spot size of SIMS pit in this study is 7 μm. Therefore, SIMS analysis in this study offers much higher spatial resolution than conventional GS-IRMS analysis. Data source: GS-IRMS and XRD data (Cui et al., 2017); SEM and SIMS results (this study). Abbreviations: GS-IRMS, gas source-isotope ratio mass spectrometry; MDAC, methane-derived authigenic calcite; SIMS, secondary ion mass spectrometry; XRD, X-ray diffraction.

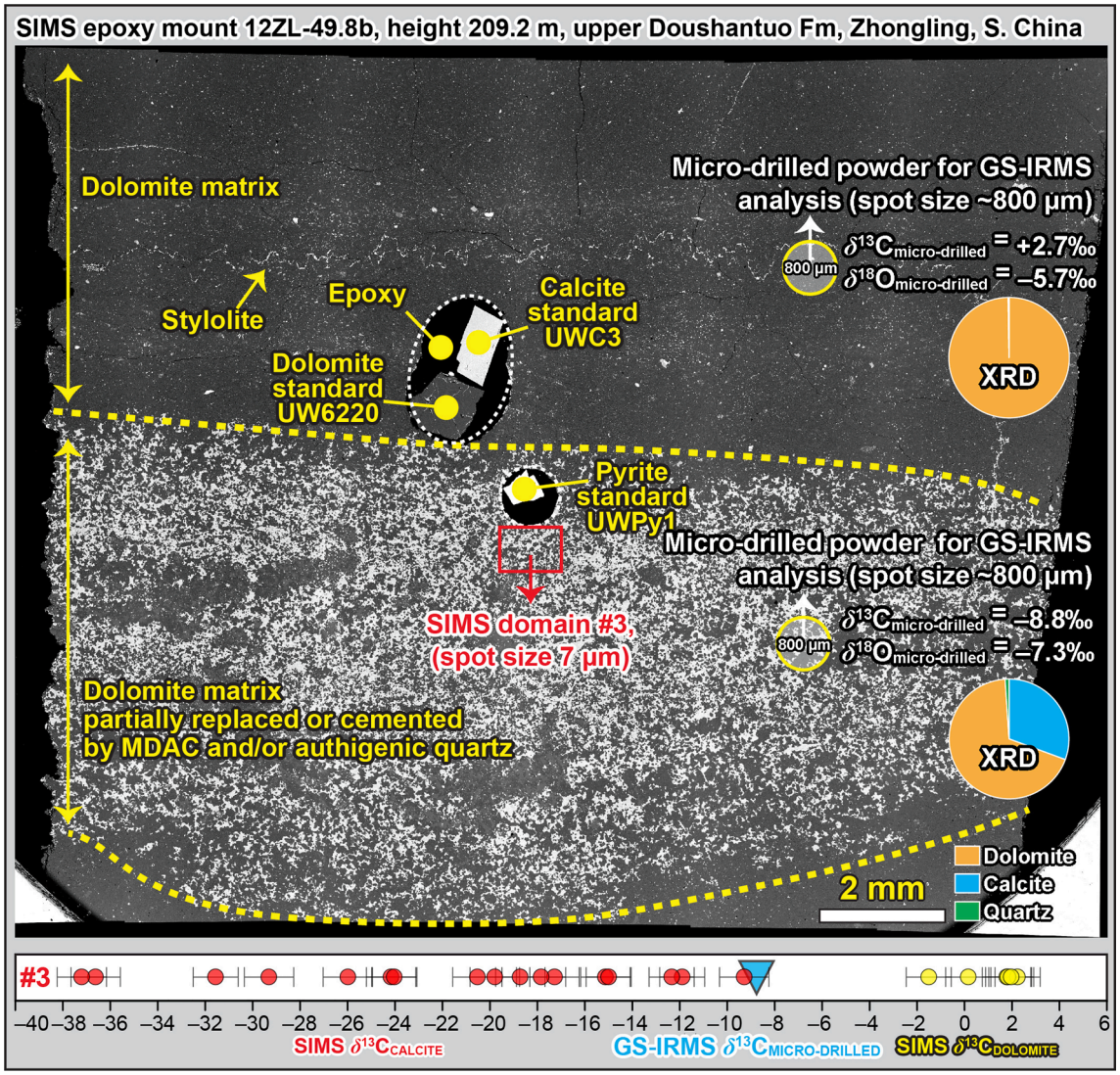

Fig. A2. Composite panorama of SIMS epoxy mount 12ZL-49.8b based on 6×6 BSE images. The SIMS $\delta^{13}C_{calcite}$ (‰, VPDB, 7-μm spot size, red circles) and $\delta^{13}C_{dolomite}$ (‰, VPDB, 7-μm spot size, yellow circles) data measured from SIMS domain #3 are plotted at the bottom. Error bars represent two standard deviations. Measured $\delta^{13}C_{carb}$ of micro-drilled powders (~800-μm spot size, blue triangle) by GS-IRMS is also plotted. This SIMS mount is 25 mm in diameter, with three WiscSIMS standards (calcite UWC3, dolomite UW6220, and pyrite UWPy1) mounted in the center. The upper half of this SIMS mount is dominated by fine-grained dolomite (darker under BSE), whereas the lower half shows dolomite matrix with ^{13}C-depleted, methane-derived authigenic calcite (MDAC) cements (brighter under BSE) and a trace amount of authigenic quartz. The $\delta^{13}C_{carb}$ (VPDB) and $\delta^{18}O_{carb}$ (VPDB) data of micro-drilled powders from the upper and lower halves were analyzed by conventional GS-IRMS. SIMS domain #3 (marked as red box) was investigated by SEM, CL and WiscSIMS in this study. Note that the spot size of micro-drilling bit is ~800 μm, while the spot size of SIMS pit in this study is 7 μm. Therefore, SIMS analysis in this study offers much higher spatial resolution than conventional GS-IRMS analysis. Data source: GS-IRMS and XRD data (Cui et al., 2017); SEM and SIMS results (this study). Abbreviations: GS-IRMS, gas source-isotope ratio mass spectrometry; MDAC, methane-derived authigenic calcite; SIMS, secondary ion mass spectrometry; XRD, X-ray diffraction.

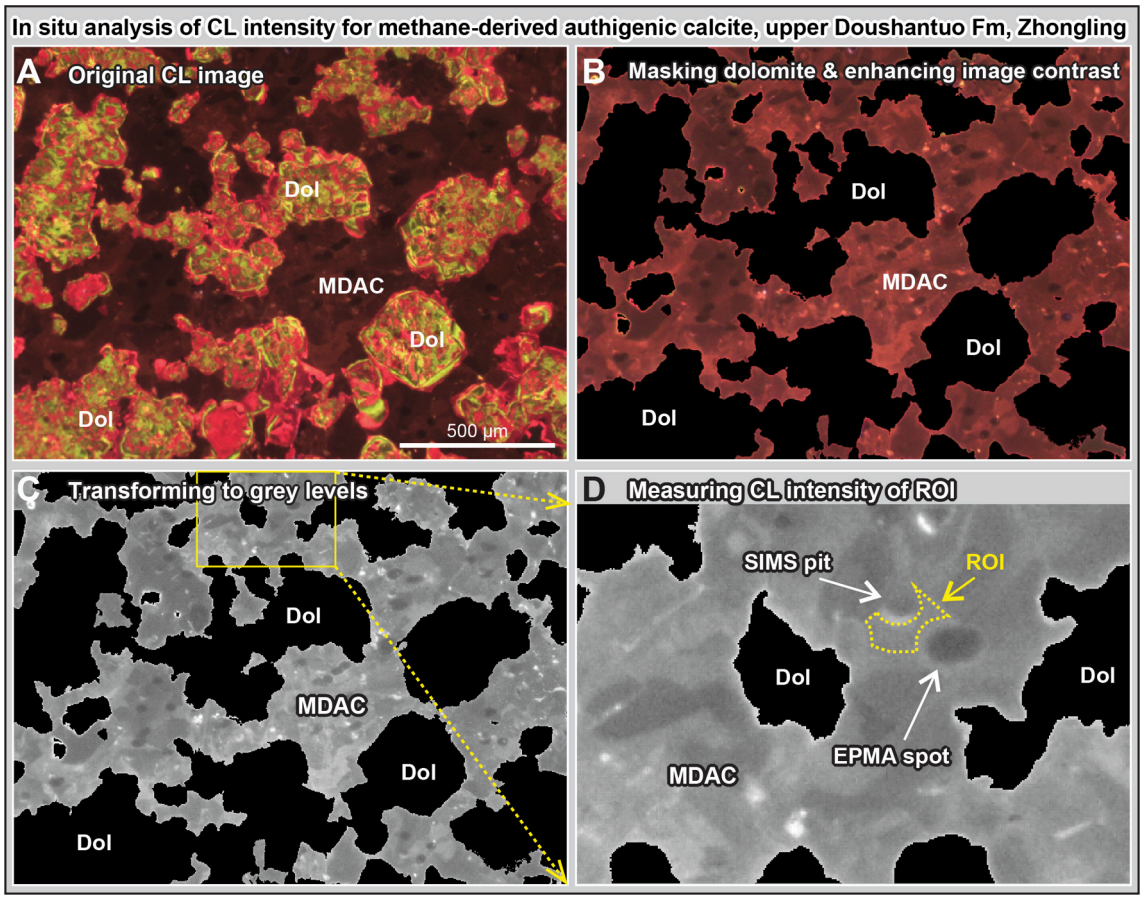

Fig. A3. Procedures showing the measurement of cold-cathode CL intensity of methane-derived authigenic calcite (MDAC) cements, upper Doushantuo Formation, Zhongling section, South China. **(A)** Original cold-cathode CL image of SIMS domain #3, sample 12-ZL49.8b (209.2 m in height), upper Doushantuo Formation, Zhongling section, South China**. (B)** Cold-cathode CL image with masked dolomite luminescence and enhanced image contrast. **(C)** Cold-cathode CL image after grey level transformation. **(D)** Region of interest (ROI, areas surrounding SIMS pits) for cold-cathode CL intensity analysis by Fiji image analysis software. See section 4.2 for detailed description of the analytical method. All the CL intensity results can be found in Fig. 12 and the online supplementary materials. Abbreviations: Cal, calcite; CL, cathodoluminescence; Dol, dolomite; MDAC, methane-derived authigenic calcite; ROI, region of interest.

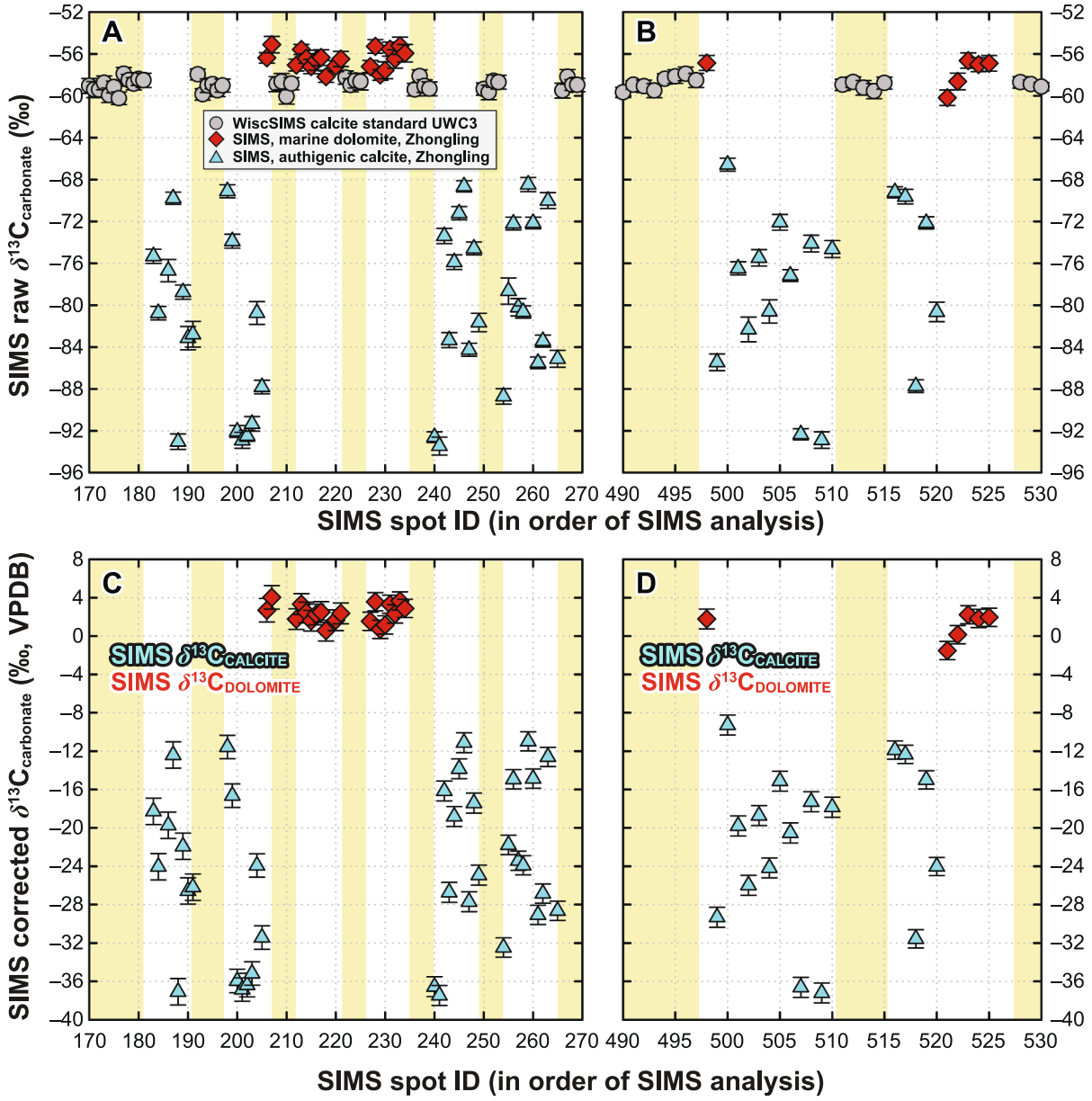

Fig. A4. SIMS data of sample 12ZL-49.8a (**A**, **C**; also see Fig. A1) and sample 12ZL-49.8b (**B**, **D**; also see Fig. A2) during WiscSIMS session 2018-02-05. The samples were collected from the upper Doushantuo Formation, Zhongling section, South China. **(A, B)** Raw $\delta^{13}C_{carbonate}$ data plotted in the order of SIMS analysis. **(C, D)** Corrected $\delta^{13}C_{carbonate}$ data plotted in the order of SIMS analysis. The X-axis shows the unique code of each spot analysis during WiscSIMS session 2018-02-05. Yellow-shaded intervals represent the analyses of WiscSIMS UWC3 calcite standard. All the data are new in this study and are available in the online supplementary material.

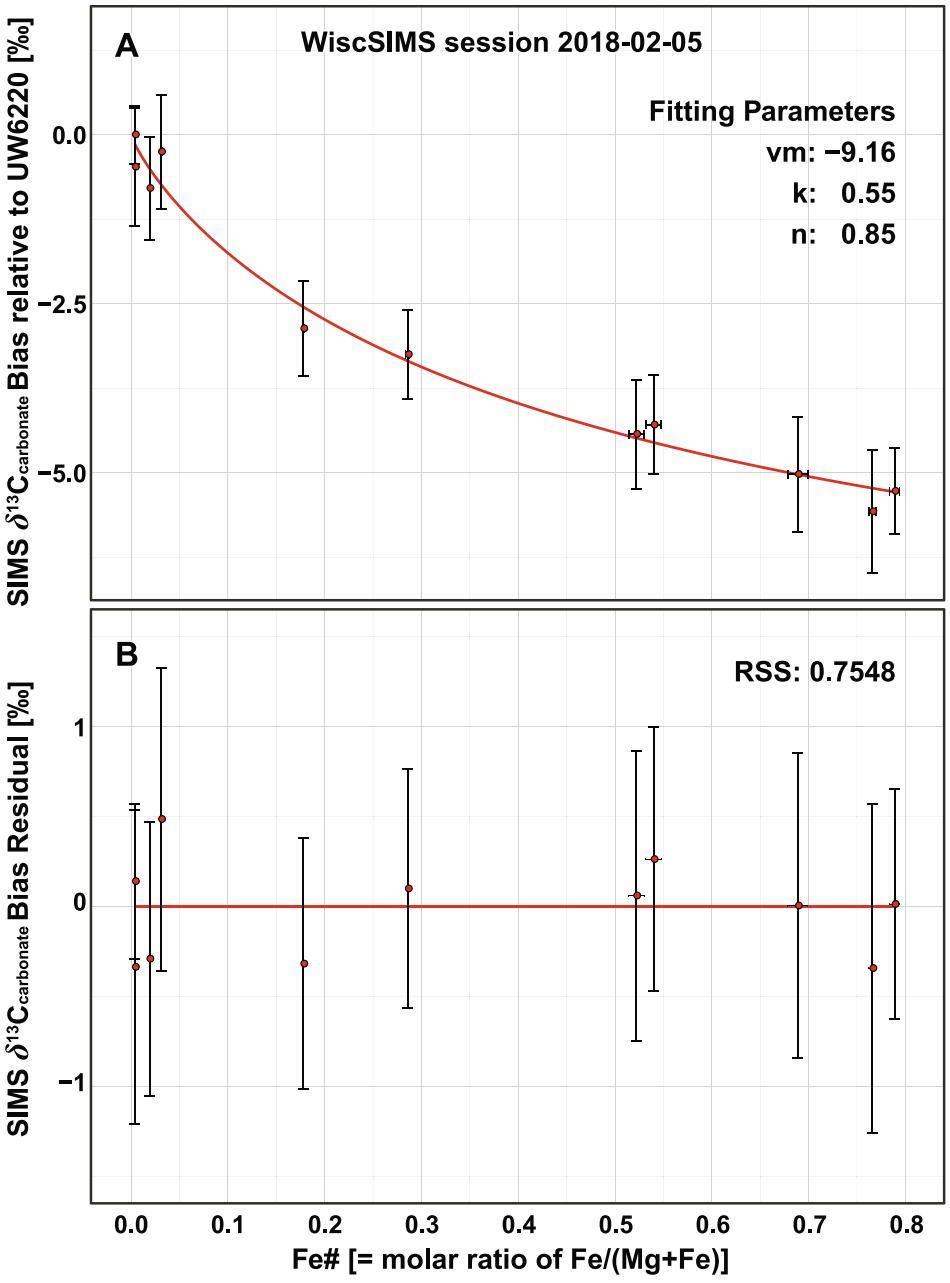

Fig. A5. SIMS $\delta^{13}C_{carbonate}$ bias (i.e., instrumental mass fractionation, IMF) plotted against Fe# [= molar ratio of Fe/(Mg+Fe)]. **(A)** SIMS bias relative to WiscSIMS dolomite standard UW6220. The calibration curve is based on SIMS analyses of a suite of standards along the dolomite–ankerite series at the beginning of WiscSIMS session 2018-02-05. **(B)** SIMS bias residuals after correction. Error bars represent propagated errors [= $(ERR\_RM^2 + ERR\_STD^2)^{0.5}$] calculated from the 2SE of reference materials (i.e., calibration standards) (ERR_RM) and the 2SE of bracketing standards for calibration standards (ERR_STD). All the data are available in the online supplementary material. Abbreviations: IMF, instrumental mass fractionation; RSS, residual sum of squares; SIMS, secondary ion mass spectrometry.

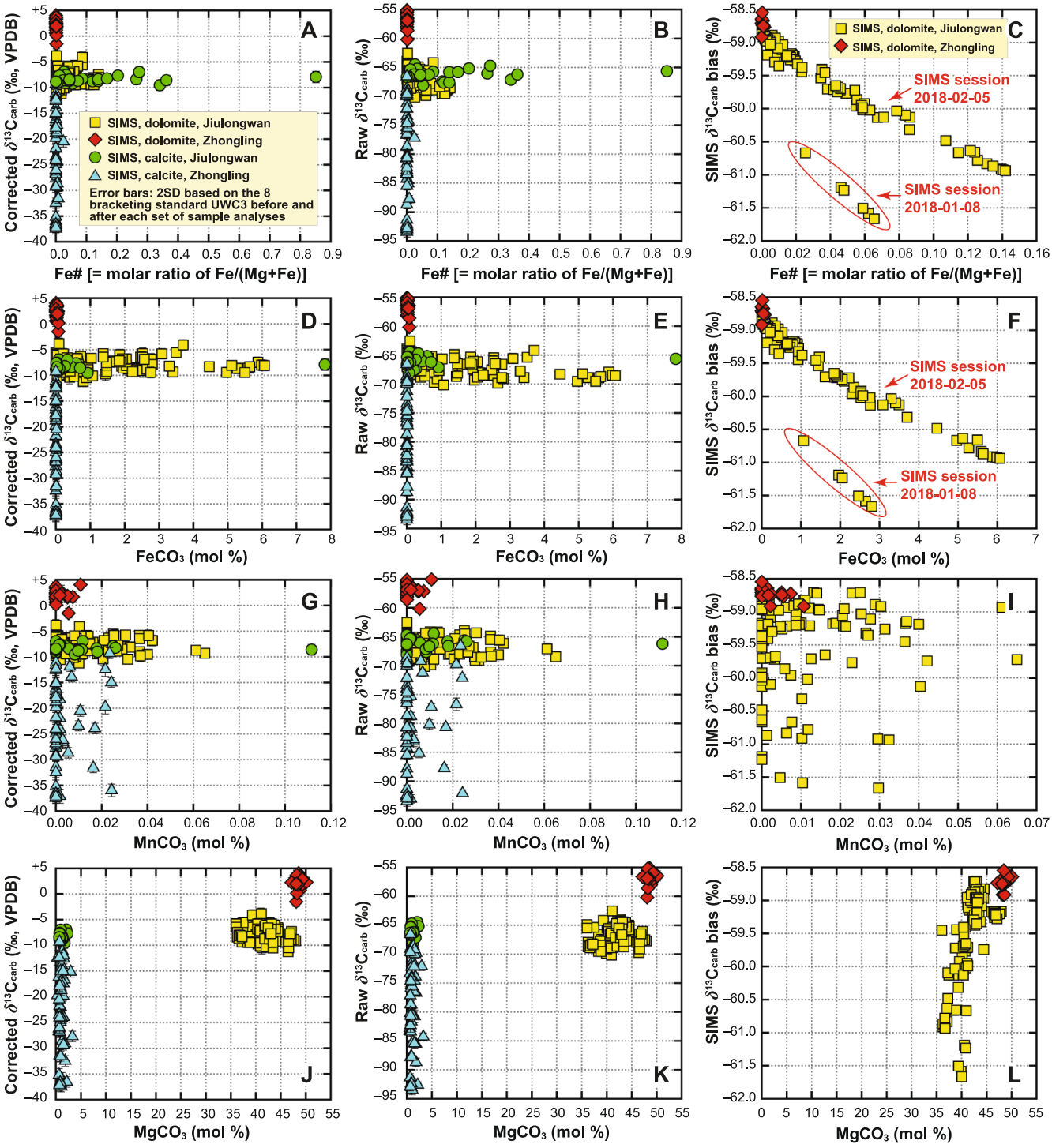

Fig. A6. Cross-plots of SIMS data vs. elemental abundances. Error bars, if not shown, are smaller than symbol size. **(A–C)** Cross-plots of the corrected SIMS data, raw SIMS data, and instrumental bias vs. Fe# [= molar ratio of Fe/(Mg+Fe)]. **(D–F)** Cross-plots of the corrected SIMS data, raw SIMS data, and instrumental bias vs. $FeCO_3$ (mol%). **(G–I)** Cross-plots of the corrected SIMS data, raw SIMS data, and instrumental bias vs. $MnCO_3$ (mol%). **(J–L)** Cross-plots of the corrected SIMS data, raw SIMS data, and instrumental bias vs. $MgCO_3$ (mol%). Note that the dolomite data from Zhongling show very low Fe#, $FeCO_3$ (mol%), and $MnCO_3$ (mol%) values, while the dolomite data from Jiulongwan show much larger range and variations. Data source: Jiulongwan SIMS and EPMA data (Cui et al., 2021); Zhongling SIMS and EPMA data (this study). All the Zhongling data are available in the online supplementary material.

Appendix A. Supplementary material

Online supplementary materials. Supplementary material 1: Integrated SEM-CL-SIMS results of sample 12ZL-49.8a (PowerPoint slides). Supplementary material 2: Integrated SEM-CL-SIMS results of sample 12ZL-49.8b (PowerPoint slides). Supplementary material 3: SEM-EDS results of samples 12ZL-49.8a and 12ZL-49.8b (PowerPoint slides). Supplementary material 4: SIMS data (Excel spreadsheet). Supplementary material 5: EPMA data (Excel spreadsheet). Supplementary material 6: CL intensity results generated by cold-cathode CL. Supplementary data to this article can be found online at https://doi.org/10.1016/j.precamres.2022.106676.

References

Ader, M., Macouin, M., Trindade, R.I.F., Hadrien, M.-H., Yang, Z., Sun, Z., Besse, J., 2009. A multilayered water column in the Ediacaran Yangtze platform? Insights from carbonate and organic matter paired $\delta^{13}C$. Earth Planet. Sci. Lett. 288, 213–227. https://doi.org/10.1016/j.epsl.2009.09.024.

An, Z., Jiang, G., Tong, J., Tian, L., Ye, Q., Song, H., Song, H., 2015. Stratigraphic position of the Ediacaran Miaohe biota and its constrains on the age of the upper Doushantuo $\delta^{13}C$ anomaly in the Yangtze Gorges area, South China. Precambr. Res. 271, 243–253. https://doi.org/10.1016/j.precamres.2015.10.007.

Andrieu, S., Brigaud, B., Barbarand, J., Lasseur, E., 2017. The complex diagenetic history of discontinuities in shallow-marine carbonate rocks: New insights from high-resolution ion microprobe investigation of $\delta^{18}O$ and $\delta^{13}C$ of early cements. Sedimentology 65, 360–399. https://doi.org/10.1111/sed.12384.

Bakakas Mayika, K., Moussavou, M., Prave, A.R., Lepland, A., Mbina, M., Kirsimäe, K., 2020. The Paleoproterozoic Francevillian succession of Gabon and the Lomagundi-Jatuli event. Geology 48, 1099–1104. https://doi.org/10.1130/g47651.1.

Baker, A.J., Fallick, A.E., 1989. Heavy carbon in two-billion-year-old marbles from Lofoten-Vesterålen, Norway: Implications for the Precambrian carbon cycle. Geochim. Cosmochim. Acta 53, 1111–1115. https://doi.org/10.1016/0016-7037(89)90216-0.

Banner, J.L., 1995. Application of the trace element and isotope geochemistry of strontium to studies of carbonate diagenesis. Sedimentology 42, 805–824. https://doi.org/10.1111/j.1365-3091.1995.tb00410.x.

Bao, H., Peng, Y., Jiang, G., Crockford, P.W., Feng, D., Xiao, S., Kaufman, A.J., Wang, J., 2021. A Transient Peak in Seawater Sulfate After the 635-Ma Snowball Earth, AGU Fall Meeting 2021.

Barbin, V., 2013. Application of cathodoluminescence microscopy to recent and past biological materials: a decade of progress. Mineral. Petrol. 107, 353–362. https://doi.org/10.1007/s00710-013-0266-6.

Barnaby, R.J., Rimstidt, J.D., 1989. Redox conditions of calcite cementation interpreted from Mn and Fe contents of authigenic calcites. Geological Society of America Bulletin, 101, 795–804. https://doi.org/0.1130/0016-7606(1989)101<0795:RCOCCI>2.3.CO;2.

Bergmann, K.D., Zentmyer, R.A., Fischer, W.W., 2011. The stratigraphic expression of a large negative carbon isotope excursion from the Ediacaran Johnnie Formation, Death Valley. Precambr. Res. 188, 45–56. https://doi.org/10.1016/j.precamres.2011.03.014.

Bergmann, K.D., Grotzinger, J.P., Osburn, M., Eiler, J.M., Fischer, W.W., 2013a. Chapter 2. Constraints on Ediacaran carbon cycle dynamics from the Shuram excursion of Oman. In: Bergmann, K.D. (Ed.), Constraints on the Carbon Cycle and Climate during the Early Evolution of Animals. Ph.D. Dissertation, California Institute of Technology, Pasadena, California, pp. 33–74. https://doi.org/10.7907/KFJX-7S28.

Bergmann, K.D., Zentmyer, R.A., Fischer, W.W., 2013b. Chapter 3. The stratigraphic expression of a large negative carbon isotope excursion from the Ediacaran Johnnie Formation, Death Valley. In: Bergmann, K.D. (Ed.), Constraints on the Carbon Cycle and Climate during the Early Evolution of Animals. Dissertation (Ph.D.), California Institute of Technology, Pasadena, California, pp. 75–119. https://doi.org/10.7907/KFJX-7S28.

Berner, R.A., 1981. Authigenic mineral formation resulting from organic matter decomposition in modern sediments. Fortschr. Mineral. 59, 117–135.

Birgel, D., Meister, P., Lundberg, R., Horath, T.D., Bontognali, T.R.R., Bahniuk, A.M., de Rezende, C.E., Vasconcelos, C., McKenzie, J.A., 2015. Methanogenesis produces strong ^{13}C enrichment in stromatolites of Lagoa Salgada, Brazil: a modern analogue for Palaeo-/Neoproterozoic stromatolites? Geobiology 13, 245–266. https://doi.org/10.1111/gbi.12130.

Bjerrum, C.J., Canfield, D.E., 2011. Towards a quantitative understanding of the late Neoproterozoic carbon cycle. Proc. Natl. Acad. Sci. 108, 5542–5547. https://doi.org/10.1073/pnas.1101755108.

Bold, U., Smith, E.F., Rooney, A.D., Bowring, S.A., Buchwaldt, R., Dudás, F.Ő., Ramezani, J., Crowley, J.L., Schrag, D.P., Macdonald, F.A., 2016. Neoproterozoic stratigraphy of the Zavkhan terrane of Mongolia: The backbone for Cryogenian and early Ediacaran chemostratigraphic records. Am. J. Sci. 316, 1–63. https://doi.org/10.2475/01.2016.01.

Brand, U., Veizer, J., 1980. Chemical diagenesis of a multicomponent carbonate system—1: Trace elements. J. Sediment. Res. 50, 1219–1236. https://doi.org/10.1306/212F7BB7-2B24-11D7-8648000102C1865D.

Bristow, T.F., Kennedy, M.J., 2008. Carbon isotope excursions and the oxidant budget of the Ediacaran atmosphere and ocean. Geology 36, 863–866. https://doi.org/10.1130/G24968A.1.

Bristow, T.F., Bonifacie, M., Derkowski, A., Eiler, J.M., Grotzinger, J.P., 2011. A hydrothermal origin for isotopically anomalous cap dolostone cements from south China. Nature 474, 68–71. https://doi.org/10.1038/nature10096.

Broecker, W.S., 1970. A boundary condition on the evolution of atmospheric oxygen. J. Geophys. Res. 75, 3553–3557. https://doi.org/10.1029/JC075i018p03553.

Burns, S.J., Matter, A., 1993. Carbon isotopic record of the latest Proterozoic from Oman. Eclogae Geol. Helv. 86, 595–607. https://doi.org/10.5169/seals-167254.

Burns, S.J., Haudenschild, U., Matter, A., 1994. The strontium isotopic composition of carbonates from the late Precambrian (~560–540 Ma) Huqf Group of Oman. Chem. Geol. 111, 269–282. https://doi.org/10.1016/0009-2541(94)90094-9.

Busch, J.F., Hodgin, E.B., Ahm, A.-S.-C., Husson, J.M., Macdonald, F.A., Bergmann, K.D., Higgins, J.A., Strauss, J.V., 2022. Global and local drivers of the Ediacaran Shuram carbon isotope excursion. Earth Planet. Sci. Lett. 579, 117368 https://doi.org/10.1016/j.epsl.2022.117368.

Butterfield, N.J., 2015. The Neoproterozoic. Curr. Biol. 25, R859–R863. https://doi.org/10.1016/j.cub.2015.07.021.

Calver, C.R., 2000. Isotope stratigraphy of the Ediacarian (Neoproterozoic III) of the Adelaide Rift Complex, Australia, and the overprint of water column stratification. Precambr. Res. 100, 121–150. https://doi.org/10.1016/s0301-9268(99)00072-8.

Canfield, D.E., Knoll, A.H., Poulton, S.W., Narbonne, G.M., Dunning, G.R., 2020. Carbon isotopes in clastic rocks and the Neoproterozoic carbon cycle. Am. J. Sci. 320, 97–124. https://doi.org/10.2475/02.2020.01.

Cao, M., Daines, S.J., Lenton, T.M., Cui, H., Algeo, T.J., Dahl, T.W., Shi, W., Chen, Z.-Q., Anbar, A., Zhou, Y.-Q., 2020. Comparison of Ediacaran platform and slope $\delta^{238}U$ records in South China: Implications for global-ocean oxygenation and the origin of the Shuram Excursion. Geochim. Cosmochim. Acta 287, 111–124. https://doi.org/10.1016/j.gca.2020.04.035.

Chang, B., Li, C., Liu, D., Foster, I., Tripati, A., Lloyd, M.K., Maradiaga, I., Luo, G., An, Z., She, Z., Xie, S., Tong, J., Huang, J., Algeo, T.J., Lyons, T.W., Immenhauser, A., 2020. Massive formation of early diagenetic dolomite in the Ediacaran ocean: Constraints on the "dolomite problem". Proc. Natl. Acad. Sci. 117, 14005–14014. https://doi.org/10.1073/pnas.1916673117.

Chen, B., Hu, C., Mills, B.J.W., He, T., Andersen, M.B., Chen, X., Liu, P., Lu, M., Newton, R.J., Poulton, S.W., Shields, G.A., Zhu, M., 2022. A short-lived oxidation event during the early Ediacaran and delayed oxygenation of the Proterozoic ocean. Earth Planet. Sci. Lett. 577, 117274 https://doi.org/10.1016/j.epsl.2021.117274.

Chen, Z., Zhou, C., Meyer, M., Xiang, K., Schiffbauer, J.D., Yuan, X., Xiao, S., 2013. Trace fossil evidence for Ediacaran bilaterian animals with complex behaviors. Precambr. Res. 224, 690–701. https://doi.org/10.1016/j.precamres.2012.11.004.

Cheng, M., Wang, H., Li, C., Luo, G., Huang, J., She, Z., Lei, L., Ouyang, G., Zhang, Z., Dodd, M.S., Algeo, T.J., 2022. Barite in the Ediacaran Doushantuo Formation and its implications for marine carbon cycling during the largest negative carbon isotope excursion in Earth's history. Precambr. Res. 368, 106485 https://doi.org/10.1016/j.precamres.2021.106485.

Condon, D., Zhu, M., Bowring, S., Wang, W., Yang, A., Jin, Y., 2005. U-Pb ages from the Neoproterozoic Doushantuo Formation, China. Science 308, 95–98. https://doi.org/10.1126/science.1107765.

Črne, A.E., Melezhik, V.A., Lepland, A., Fallick, A.E., Prave, A.R., Brasier, A.T., 2014. Petrography and geochemistry of carbonate rocks of the Paleoproterozoic Zaonega Formation, Russia: Documentation of ^{13}C-depleted non-primary calcite. Precambr. Res. 240, 79–93. https://doi.org/10.1016/j.precamres.2013.10.005.

Cui, H., Kaufman, A.J., Xiao, S., Zhu, M., Zhou, C., Liu, X.-M., 2015. Redox architecture of an Ediacaran ocean margin: Integrated chemostratigraphic ($\delta^{13}C$–$\delta^{34}S$–$^{87}Sr/^{86}Sr$–Ce/Ce*) correlation of the Doushantuo Formation, South China. Chem. Geol. 405, 48–62. https://doi.org/10.1016/j.chemgeo.2015.04.009.

Cui, H., Xiao, S., Zhou, C., Peng, Y., Kaufman, A.J., Plummer, R.E., 2016. Phosphogenesis associated with the Shuram Excursion: Petrographic and geochemical observations from the Ediacaran Doushantuo Formation of South China. Sed. Geol. 341, 134–146. https://doi.org/10.1016/j.sedgeo.2016.05.008.

Cui, H., Kaufman, A.J., Xiao, S., Zhou, C., Liu, X.-M., 2017. Was the Ediacaran Shuram Excursion a globally synchronized early diagenetic event? Insights from methane-derived authigenic carbonates in the uppermost Doushantuo Formation, South China. Chem. Geol. 450, 59–80. https://doi.org/10.1016/j.chemgeo.2016.12.010.

Cui, H., Kaufman, A.J., Peng, Y., Liu, X.-M., Plummer, R.E., Lee, E.I., 2018. The Neoproterozoic Hüttenberg $\delta^{13}C$ anomaly: Genesis and global implications. Precambr. Res. 313, 242–262. https://doi.org/10.1016/j.precamres.2018.05.024.

Cui, H., Orland, I.J., Denny, A., Kitajima, K., Fournelle, J.H., Baele, J.-M., de Winter, N.J., Goderis, S., Claeys, P., Valley, J.W., 2019. Ice or fire? Constraining the origin of isotopically anomalous cap carbonate cements by SIMS, Geological Society of America Abstracts with Programs. Vol. 51, No. 5, Phoenix, Arizona, USA https://doi.org/10.1130/abs/2019AM-332456.

Cui, H., Kaufman, A.J., Zou, H., Kattan, F.H., Trusler, P., Smith, J., Yu. Ivantsov, A., Rich, T.H., Al Qubsani, A., Yazedi, A., Liu, X.-M., Johnson, P., Goderis, S., Claeys, P., Vickers-Rich, P., 2020a. Primary or secondary? A dichotomy of the strontium isotope anomalies in the Ediacaran carbonates of Saudi Arabia. Precamb. Res. 343, 105720. https://doi.org/10.1016/j.precamres.2020.105720.

Cui, H., Warren, L.V., Uhlein, G.J., Okubo, J., Liu, X.-M., Plummer, R.E., Baele, J.-M., Goderis, S., Claeys, P., Li, F., 2020b. Global or regional? Constraining the origins of the middle Bambuí carbon cycle anomaly in Brazil. Precambr. Res. 348, 105861 https://doi.org/10.1016/j.precamres.2020.105861.

Cui, H., 2021. Inside out: Deep carbon linked to deep-time carbon cycle. Science Bull. 66, 1822–1824. https://doi.org/10.1016/j.scib.2021.06.001.

Cui, H., Kitajima, K., Orland, I.J., Xiao, S., Baele, J.-M., Kaufman, A.J., Denny, A., Zhou, C., Spicuzza, M.J., Fournelle, J.H., Valley, J.W., 2021. Deposition or diagenesis? Probing the Ediacaran Shuram excursion in South China by SIMS. Global Planet. Change 206, 103591. https://doi.org/10.1016/j.gloplacha.2021.103591.

Cui, H., Kaufman, A.J., Xiao, S., Zhou, C., Zhu, M., Cao, M., Loyd, S., Crockford, P., Liu, X.-M., Goderis, S., Wang, W., Guan, C., 2022. Dynamic interplay of biogeochemical C, S, and Ba cycles in response to the Shuram oxygenation event. Journal of the Geological Society, 179, jgs2021-081. https://doi.org/10.1144/jgs2021-081.

Denny, A.C., Kozdon, R., Kitajima, K., Valley, J.W., 2017. Isotopically zoned carbonate cements in Early Paleozoic sandstones of the Illinois Basin: $\delta^{18}O$ and $\delta^{13}C$ records of burial and fluid flow. Sed. Geol. 361, 93–110. https://doi.org/10.1016/j.sedgeo.2017.09.004.

Denny, A.C., Orland, I.J., Valley, J.W., 2020. Regionally correlated oxygen and carbon isotope zonation in diagenetic carbonates of the Bakken Formation. Chem. Geol. 531, 119327 https://doi.org/10.1016/j.chemgeo.2019.119327.

Derry, L.A., 2010. A burial diagenesis origin for the Ediacaran Shuram-Wonoka carbon isotope anomaly. Earth Planet. Sci. Lett. 294, 152–162. https://doi.org/10.1016/j.epsl.2010.03.022.

Des Marais, D.J., Strauss, H., Summons, R.E., Hayes, J.M., 1992. Carbon isotope evidence for the stepwise oxidation of the Proterozoic environment. Nature 359, 605–609. https://doi.org/10.1038/359605a0.

El Ali, A., Barbin, V., Calas, G., Cervelle, B., Ramseyer, K., Bouroulec, J., 1993. Mn^{2+}-activated luminescence in dolomite, calcite and magnesite: quantitative determination of manganese and site distribution by EPR and CL spectroscopy. Chem. Geol. 104, 189–202. https://doi.org/10.1016/0009-2541(93)90150-H.

Fakhraee, M., Tarhan, L.G., Planavsky, N.J., Reinhard, C.T., 2021. A largely invariant marine dissolved organic carbon reservoir across Earth's history. Proc. Natl. Acad. Sci. 118, e2103511118 https://doi.org/10.1073/pnas.2103511118.

Fantle, M.S., Barnes, B.D., Lau, K.V., 2020. The role of diagenesis in shaping the geochemistry of the marine carbonate record. Annu. Rev. Earth Planet. Sci. 48, 549–583. https://doi.org/10.1146/annurev-earth-073019-060021.

Fike, D.A., Grotzinger, J.P., Pratt, L.M., Summons, R.E., 2006. Oxidation of the Ediacaran ocean. Nature 444, 744–747. https://doi.org/10.1038/nature05345.

Frank, J.R., Carpenter, A.B., Oglesby, T.W., 1982. Cathodoluminescence and composition of calcite cement in the Taum Sauk Limestone (Upper Cambrian), southeast Missouri. J. Sediment. Res. 52, 631–638. https://doi.org/10.1306/212F7FB8-2B24-11D7-8648000102C1865D.

Furuyama, S., Kano, A., Kunimitsu, Y., Ishikawa, T., Wei, W., 2016. Diagenetic overprint to a negative carbon isotope anomaly associated with the Gaskiers glaciation of the Ediacaran Doushantuo Formation in South China. Precambr. Res. 276, 110–122. https://doi.org/10.1016/j.precamres.2016.01.004.

Furuyama, S., Kano, A., Kunimitsu, Y., Ishikawa, T., Wang, W., Liu, X.-C., 2017. Chemostratigraphy of the Ediacaran basinal setting on the Yangtze platform, South China: Oceanographic and diagenetic aspects of the carbon isotopic depth gradient. Isl. Arc 26, e12196. https://doi.org/10.1111/iar.12196.

Gao, Y., Zhang, X., Zhang, G., Chen, K., Shen, Y., 2018. Ediacaran negative C-isotopic excursions associated with phosphogenic events: Evidence from South China. Precambr. Res. 307, 218–228. https://doi.org/10.1016/j.precamres.2018.01.014.

Gao, Y., Zhang, X., Xu, Y., Fang, C., Gong, Y., Shen, Y., 2019. High primary productivity during the Ediacaran Period revealed by the covariation of paired C-isotopic records from South China. Precambrian Research, 349, 105411. https://doi.org/https://doi.org/10.1016/j.precamres.2019.105411.

Giddings, J.A., Wallace, M.W., 2009. Facies-dependent $\delta^{13}C$ variation from a Cryogenian platform margin, South Australia: Evidence for stratified Neoproterozoic oceans? Palaeogeogr. Palaeoclimatol. Palaeoecol. 271, 196–214. https://doi.org/10.1016/j.palaeo.2008.10.011.

Gillhaus, A., Habermann, D., Meijer, J., Richter, D., 2000. Cathodoluminescence spectroscopy and micro-PIXE: combined high resolution Mn-analyses in dolomites–First results. Nucl. Instrum. Methods Phys. Res., Sect. B 161, 842–845.

Gillhaus, A., Richter, D.K., Götte, T., Neuser, R.D., 2010. From tabular to rhombohedral dolomite crystals in Zechstein 2 dolostones from Scharzfeld (SW Harz/Germany): A case study with combined CL and EBSD investigations. Sed. Geol. 228, 284–291. https://doi.org/10.1016/j.sedgeo.2010.05.003.

Glenn, C.R., Prévôt-Lucas, L., Lucas, J., 2000. Marine Authigenesis: From Global To Microbial. SEPM Special Publication No. 66. SEPM (Society for Sedimentary Geology), Tullsa, Oklahoma, USA https://doi.org/10.2110/pec.00.66.

Gong, Z., Kodama, K.P., Li, Y.-X., 2017. Rock magnetic cyclostratigraphy of the Doushantuo Formation, South China and its implications for the duration of the Shuram carbon isotope excursion. Precambr. Res. 289, 62–74. https://doi.org/10.1016/j.precamres.2016.12.002.

Gong, Z., Li, M., 2020. Astrochronology of the Ediacaran Shuram carbon isotope excursion Oman. Earth Planetary Sci. Lett. 547, 116462 https://doi.org/10.1016/j.epsl.2020.116462.

Götze, J., 2012. Application of cathodoluminescence microscopy and spectroscopy in geosciences. Microsc. Microanal. 18, 1270–1284. https://doi.org/10.1017/S1431927612001122.

Grotzinger, J.P., Fike, D.A., Fischer, W.W., 2011. Enigmatic origin of the largest-known carbon isotope excursion in Earth's history. Nat. Geosci. 4, 285–292. https://doi.org/10.1038/ngeo1138.

Halverson, G.P., Hoffman, P.F., Schrag, D.P., Maloof, A.C., Rice, A.H.N., 2005. Toward a Neoproterozoic composite carbon-isotope record. Geol. Soc. Am. Bull. 117, 1181–1207. https://doi.org/10.1130/b25630.1.

Hardie, L.A., 2003. Anhydrite and gypsum. In: Middleton, G.V., Church, M.J., Coniglio, M., Hardie, L.A., Longstaffe, F.J. (Eds.), Encyclopedia of Sediments and Sedimentary Rocks. Springer, Netherlands, Dordrecht, pp. 16–19. https://doi.org/10.1007/978-1-4020-3609-5_7.

Hayes, J.M., 1993. Factors controlling ^{13}C contents of sedimentary organic compounds: Principles and evidence. Mar. Geol. 113, 111–125. https://doi.org/10.1016/0025-3227(93)90153-m.

Hayes, J.M., Strauss, H., Kaufman, A.J., 1999. The abundance of ^{13}C in marine organic matter and isotopic fractionation in the global biogeochemical cycle of carbon during the past 800 Ma. Chem. Geol. 161, 103–125. https://doi.org/10.1016/s0009-2541(99)00083-2.

Higgins, J.A., Blättler, C.L., Lundstrom, E.A., Santiago-Ramos, D.P., Akhtar, A.A., Crüger Ahm, A.S., Bialik, O., Holmden, C., Bradbury, H., Murray, S.T., Swart, P.K., 2018. Mineralogy, early marine diagenesis, and the chemistry of shallow-water carbonate sediments. Geochim. Cosmochim. Acta 220, 512–534. https://doi.org/10.1016/j.gca.2017.09.046.

Hodgin, E.B., 2020. A Reappraisal of Neoproterozoic to Early Paleozoic Terrane Provenance from the Iapetan Realm and the Tectonic Implications. Ph.D. dissertation, Harvard University, Cambridge, Massachusetts, United States, https://nrs.harvard.edu/URN-3:HUL.INSTREPOS:37365964.

Hoffman, P.F., Lamothe, K.G., 2019. Seawater-buffered diagenesis, destruction of carbon isotope excursions, and the composition of DIC in Neoproterozoic oceans. Proc. Natl. Acad. Sci. 116, 18874–18879. https://doi.org/10.1073/pnas.1909570116.

Hood, A.v.S., Wallace, M.W., 2012. Synsedimentary diagenesis in a Cryogenian reef complex: Ubiquitous marine dolomite precipitation. Sedimentary Geology, 255–256, 56–71. https://doi.org/10.1016/j.sedgeo.2012.02.004.

Hood, A.v.S., Wallace, M.W., Reed, C.P., Hoffmann, K.H., Freyer, E.E., 2015. Enigmatic carbonates of the Ombombo Subgroup, Otavi Fold Belt, Namibia: A prelude to extreme Cryogenian anoxia? Sedimentary Geology, 324, 12–31. https://doi.org/10.1016/j.sedgeo.2015.04.007.

Hood, A.v.S., Planavsky, N.J., Wallace, M.W., Wang, X., Bellefroid, E.J., Gueguen, B., Cole, D.B., 2016. Integrated geochemical-petrographic insights from component-selective δ238U of Cryogenian marine carbonates. Geology, 44, 935–938. https://doi.org/10.1130/g38533.1.

Hood, A.v.S., Wallace, M.W., 2018. Neoproterozoic marine carbonates and their paleoceanographic significance. Global and Planetary Change, 160, 28–45. https://doi.org/10.1016/j.gloplacha.2017.11.006.

Husson, J.M., Maloof, A.C., Schoene, B., 2012. A syn-depositional age for Earth's deepest $\delta^{13}C$ excursion required by isotope conglomerate tests. Terra Nova 24, 318–325. https://doi.org/10.1111/j.1365-3121.2012.01067.x.

Husson, J.M., Maloof, A.C., Schoene, B., Chen, C.Y., Higgins, J.A., 2015. Stratigraphic expression of Earth's deepest $\delta^{13}C$ excursion in the Wonoka Formation of South Australia. Am. J. Sci. 315, 1–45. https://doi.org/10.2475/01.2015.01.

Husson, J.M., Linzmeier, B.J., Kitajima, K., Ishida, A., Maloof, A.C., Schoene, B., Peters, S.E., Valley, J.W., 2020. Large isotopic variability at the micron-scale in 'Shuram' excursion carbonates from South Australia. Earth Planet. Sci. Lett. 538, 116211 https://doi.org/10.1016/j.epsl.2020.116211.

Jiang, G., Kennedy, M.J., Christie-Blick, N., 2003. Stable isotopic evidence for methane seeps in Neoproterozoic postglacial cap carbonates. Nature 426, 822–826. https://doi.org/10.1038/nature02201.

Jiang, G., Kennedy, M.J., Christie-Blick, N., Wu, H., Zhang, S., 2006. Stratigraphy, sedimentary structures, and textures of the late Neoproterozoic Doushantuo cap carbonate in South China. J. Sediment. Res. 76, 978–995. https://doi.org/10.2110/jsr.2006.086.

Jiang, G., Kaufman, A.J., Christie-Blick, N., Zhang, S., Wu, H., 2007. Carbon isotope variability across the Ediacaran Yangtze platform in South China: Implications for a large surface-to-deep ocean $\delta^{13}C$ gradient. Earth Planet. Sci. Lett. 261, 303–320. https://doi.org/10.1016/j.epsl.2007.07.009.

Jiang, G., Zhang, S., Shi, X., Wang, X., 2008. Chemocline instability and isotope variations of the Ediacaran Doushantuo basin in South China. Sci. China, Ser. D Earth Sci. 51, 1560–1569. https://doi.org/10.1007/s11430-008-0116-2.

Jiang, G., Wang, X., Shi, X., Zhang, S., Xiao, S., Dong, J., 2010. Organic carbon isotope constraints on the dissolved organic carbon (DOC) reservoir at the Cryogenian-Ediacaran transition. Earth Planet. Sci. Lett. 299, 159–168. https://doi.org/10.1016/j.epsl.2010.08.031.

Jiang, G., Shi, X., Zhang, S., Wang, Y., Xiao, S., 2011. Stratigraphy and paleogeography of the Ediacaran Doushantuo Formation (ca. 635–551Ma) in South China. Gondwana Res. 19, 831–849. https://doi.org/10.1016/j.gr.2011.01.006.

Johnston, D.T., Macdonald, F.A., Gill, B.C., Hoffman, P.F., Schrag, D.P., 2012. Uncovering the Neoproterozoic carbon cycle. Nature 483, 320–323. https://doi.org/10.1038/nature10854.

Jones, D.S., Brothers, R.W., Ahm, A.-S.-C., Slater, N., Higgins, J.A., Fike, D.A., 2020. Sea level, carbonate mineralogy, and early diagenesis controlled $\delta^{13}C$ records in Upper Ordovician carbonates. Geology 48, 194–199. https://doi.org/10.1130/g46861.1.

Karhu, J.A., 1993. Paleoproterozoic evolution of the carbon isotope ratios of sedimentary carbonates in the Fennoscandian Shield (Academic Dissertation). Geological Survey of Finland Bulletin 371. Geological Survey of Finland, Espoo, Finland, p. 87.

Karhu, J.A., Holland, H.D., 1996. Carbon isotopes and the rise of atmospheric oxygen. Geology 24, 867–870. https://doi.org/10.1130/0091-7613(1996)024<0867:ciatro>2.3.co;2.

Kastner, M., 1999. Oceanic minerals: Their origin, nature of their environment, and significance. Proc. Natl. Acad. Sci. 96, 3380–3387. https://doi.org/10.1073/pnas.96.7.3380.

Kaufman, A.J., Hayes, J.M., Knoll, A.H., Germs, G.J.B., 1991. Isotopic compositions of carbonates and organic carbon from upper Proterozoic successions in Namibia: stratigraphic variation and the effects of diagenesis and metamorphism. Precambr. Res. 49, 301–327. https://doi.org/10.1016/0301-9268(91)90039-d.

Kaufman, A.J., Knoll, A.H., Awramik, S.M., 1992. Biostratigraphic and chemostratigraphic correlation of Neoproterozoic sedimentary successions: Upper Tindir Group, northwestern Canada, as a test case. Geology 20, 181–185. https://doi.org/10.1130/0091-7613(1992)020<0181:BACCON>2.3.CO;2.

Kaufman, A.J., Knoll, A.H., Narbonne, G.M., 1997. Isotopes, ice ages, and terminal Proterozoic earth history. Proc. Natl. Acad. Sci. 94, 6600–6605. https://doi.org/10.1073/pnas.94.13.6600.

Kaufman, A.J., Jiang, G., Christie-Blick, N., Banerjee, D.M., Rai, V., 2006. Stable isotope record of the terminal Neoproterozoic Krol platform in the Lesser Himalayas of northern India. Precambr. Res. 147, 156–185. https://doi.org/10.1016/j.precamres.2006.02.007.

Kaufman, A.J., Corsetti, F.A., Varni, M.A., 2007. The effect of rising atmospheric oxygen on carbon and sulfur isotope anomalies in the Neoproterozoic Johnnie Formation, Death Valley, USA. Chem. Geol. 237, 47–63. https://doi.org/10.1016/j.chemgeo.2006.06.023.

Kaufman, A.J., Kriesfeld, L., Cui, H., Narbonne, G.M., Vickers-Rich, P., Zhou, C., Xiao, S., 2015. An authigenic origin for the middle Ediacaran Shuram excursion: The view from Namibia and South China. The Geological Society of America, Baltimore, Maryland, USA, Geological Society of America Annual Meeting, p. 451.

Knauth, L.P., Kennedy, M.J., 2009. The late Precambrian greening of the Earth. Nature 460, 728–732. https://doi.org/10.1038/nature08213.
Knoll, A.H., Hayes, J.M., Kaufman, A.J., Swett, K., Lambert, I.B., 1986. Secular variation in carbon isotope ratios from Upper Proterozoic successions of Svalbard and East Greenland. Nature 321, 832–838. https://doi.org/10.1038/321832a0.
Kozdon, R., Ushikubo, T., Kita, N.T., Spicuzza, M., Valley, J.W., 2009. Intratest oxygen isotope variability in the planktonic foraminifer *N. pachyderma*: Real vs. apparent vital effects by ion microprobe. Chem. Geol. 258, 327–337. https://doi.org/10.1016/j.chemgeo.2008.10.032.
Kreitsmann, T., Külaviir, M., Lepland, A., Paiste, K., Paiste, P., Prave, A.R., Sepp, H., Romashkin, A.E., Rychanchik, D.V., Kirsimäe, K., 2019. Hydrothermal dedolomitisation of carbonate rocks of the Paleoproterozoic Zaonega Formation, NW Russia — Implications for the preservation of primary C isotope signals. Chem. Geol. 512, 43–57. https://doi.org/10.1016/j.chemgeo.2019.03.002.
Kreitsmann, T., Lepland, A., Bau, M., Prave, A., Paiste, K., Mänd, K., Sepp, H., Martma, T., Romashkin, A.E., Kirsimäe, K., 2020. Oxygenated conditions in the aftermath of the Lomagundi-Jatuli Event: The carbon isotope and rare earth element signatures of the Paleoproterozoic Zaonega Formation Russia. Precamb. Res. 347, 105855 https://doi.org/10.1016/j.precamres.2020.105855.
Kump, L.R., Arthur, M.A., 1999. Interpreting carbon-isotope excursions: carbonates and organic matter. Chem. Geol. 161, 181–198. https://doi.org/10.1016/s0009-2541(99)00086-8.
Kump, L.R., Junium, C., Arthur, M.A., Brasier, A., Fallick, A., Melezhik, V., Lepland, A., CČrne, A.E., Luo, G., 2011. Isotopic evidence for massive oxidation of organic matter following the Great Oxidation Event. Science, 334, 1694–1696. https://doi.org/10.1126/science.1213999.
Kunimitsu, Y., Setsuda, Y., Furuyama, S., Wang, W., Kano, A., 2011. Ediacaran chemostratigraphy and paleoceanography at a shallow marine setting in northwestern Hunan Province, South China. Precambr. Res. 191, 194–208. https://doi.org/10.1016/j.precamres.2011.09.006.
Laakso, T.A., Schrag, D.P., 2020. The role of authigenic carbonate in Neoproterozoic carbon isotope excursions. Earth Planet. Sci. Lett. 549, 116534 https://doi.org/10.1016/j.epsl.2020.116534.
Lan, Z., Sano, Y., Yahagi, T., Tanaka, K., Shirai, K., Papineau, D., Sawaki, Y., Ohno, T., Abe, M., Yang, H., Liu, H., Jiang, T., Wang, T., 2019. An integrated chemostratigraphic ($\delta^{13}C$-$\delta^{18}O$-$^{87}Sr/^{86}Sr$-$\delta^{15}N$) study of the Doushantuo Formation in western Hubei Province, South China. Precambr. Res. 320, 232–252. https://doi.org/10.1016/j.precamres.2018.10.018.
Le Guerroué, E., 2006. Sedimentology and chemostratigraphy of the Ediacaran Shuram Formation, Nafun Group, Oman, Eidgenössische Technische Hochschule Zürich (ETHZ), Zürich, Switzerland, https://tel.archives-ouvertes.fr/tel-00331341.
Le Guerroué, E., Allen, P.A., Cozzi, A., 2006a. Chemostratigraphic and sedimentological framework of the largest negative carbon isotopic excursion in Earth history: The Neoproterozoic Shuram Formation (Nafun Group, Oman). Precambr. Res. 146, 68–92. https://doi.org/10.1016/j.precamres.2006.01.007.
Le Guerroué, E., Allen, P.A., Cozzi, A., 2006b. Parasequence development in the Ediacaran Shuram Formation (Nafun Group, Oman): high-resolution stratigraphic test for primary origin of negative carbon isotopic ratios. Basin Res. 18, 205–219. https://doi.org/10.1111/j.1365-2117.2006.00292.x.
Le Guerroué, E., Allen, P.A., Cozzi, A., Etienne, J.L., Fanning, M., 2006c. 50 Myr recovery from the largest negative $\delta^{13}C$ excursion in the Ediacaran ocean. Terra Nova 18, 147–153. https://doi.org/10.1111/j.1365-3121.2006.00674.x.
Lee, C., Fike, D.A., Love, G.D., Sessions, A.L., Grotzinger, J.P., Summons, R.E., Fischer, W.W., 2013. Carbon isotopes and lipid biomarkers from organic-rich facies of the Shuram Formation, Sultanate of Oman. Geobiology 11, 406–419. https://doi.org/10.1111/gbi.12045.
Lenz, C., Götze, J., 2011. Manganese-Activated Cathodoluminescence of Selected Carbonate Minerals, Micro-Raman Spectroscopy and Luminescence Studies in the Earth and Planetary Sciences (CORALS II), pp. 54.
Li, C., Love, G.D., Lyons, T.W., Fike, D.A., Sessions, A.L., Chu, X., 2010. A stratified redox model for the Ediacaran ocean. Science 328, 80–83. https://doi.org/10.1126/science.1182369.
Li, C., Hardisty, D.S., Luo, G., Huang, J., Algeo, T.J., Cheng, M., Shi, W., An, Z., Tong, J., Xie, S., Jiao, N., Lyons, T.W., 2017. Uncovering the spatial heterogeneity of Ediacaran carbon cycling. Geobiology 15, 211–224. https://doi.org/10.1111/gbi.12222.
Li, H., Zhang, S., Han, J., Zhong, T., Ding, J., Wu, H., Liu, P., Dong, J., Zhang, Z., Yang, T., Jiang, G., 2022. Astrochronologic calibration of the Shuram carbon isotope excursion with new data from South China. Global Planet. Change 209, 103749. https://doi.org/10.1016/j.gloplacha.2022.103749.
Li, Z., Cao, M., Loyd, S.J., Algeo, T.J., Zhao, H., Wang, X., Zhao, L., Chen, Z.-Q., 2020. Transient and stepwise ocean oxygenation during the late Ediacaran Shuram Excursion: Insights from carbonate $\delta^{238}U$ of northwestern Mexico. Precambr. Res. 344, 105741 https://doi.org/10.1016/j.precamres.2020.105741.
Lin, Z., Wang, Q., Feng, D., Liu, Q., Chen, D., 2011. Post-depositional origin of highly ^{13}C-depleted carbonate in the Doushantuo cap dolostone in South China: Insights from petrography and stable carbon isotopes. Sed. Geol. 242, 71–79. https://doi.org/10.1016/j.sedgeo.2011.10.009.
Ling, H.-F., Chen, X., Li, D., Wang, D., Shields-Zhou, G.A., Zhu, M., 2013. Cerium anomaly variations in Ediacaran–earliest Cambrian carbonates from the Yangtze Gorges area, South China: Implications for oxygenation of coeval shallow seawater. Precambr. Res. 225, 110–127. https://doi.org/10.1016/j.precamres.2011.10.011.
Liu, J., Li, Z., Cheng, L., Li, J., 2017. Multiphase calcite cementation and fluids evolution of a deeply buried carbonate reservoir in the Upper Ordovician Lianglitag Formation, Tahe Oilfield, Tarim Basin NW China. Geofluids 2017, 4813235. https://doi.org/10.1155/2017/4813235.
Liu, Y., Chen, W., Foley, S.F., Shen, Y., Chen, C., Li, J., Ou, X., He, D., Feng, Q., Lin, J., 2021. The largest negative carbon isotope excursions in neoproterozoic carbonates caused by recycled carbonatite volcanic ash. Science Bull. 66, 1925–1931. https://doi.org/10.1016/j.scib.2021.04.021.
Loyd, S.J., Marenco, P.J., Hagadorn, J.W., Lyons, T.W., Kaufman, A.J., Sour-Tovar, F., Corsetti, F.A., 2012. Sustained low marine sulfate concentrations from the Neoproterozoic to the Cambrian: Insights from carbonates of northwestern Mexico and eastern California. Earth Planet. Sci. Lett. 339–340, 79–94. https://doi.org/10.1016/j.epsl.2012.05.032.
Loyd, S.J., Marenco, P.J., Hagadorn, J.W., Lyons, T.W., Kaufman, A.J., Sour-Tovar, F., Corsetti, F.A., 2013. Local $\delta^{34}S$ variability in ~580Ma carbonates of northwestern Mexico and the Neoproterozoic marine sulfate reservoir. Precambr. Res. 224, 551–569. https://doi.org/10.1016/j.precamres.2012.10.007.
Lu, M., Zhu, M., Zhang, J., Shields-Zhou, G., Li, G., Zhao, F., Zhao, X., Zhao, M., 2013. The DOUNCE event at the top of the Ediacaran Doushantuo Formation, South China: Broad stratigraphic occurrence and non-diagenetic origin. Precambr. Res. 225, 86–109. https://doi.org/10.1016/j.precamres.2011.10.018.
Macdonald, F.A., Strauss, J.V., Sperling, E.A., Halverson, G.P., Narbonne, G.M., Johnston, D.T., Kunzmann, M., Schrag, D.P., Higgins, J.A., 2013. The stratigraphic relationship between the Shuram carbon isotope excursion, the oxygenation of Neoproterozoic oceans, and the first appearance of the Ediacara biota and bilaterian trace fossils in northwestern Canada. Chem. Geol. 362, 250–272. https://doi.org/10.1016/j.chemgeo.2013.05.032.
Macouin, M., Besse, J., Ader, M., Gilder, S., Yang, Z., Sun, Z., Agrinier, P., 2004. Combined paleomagnetic and isotopic data from the Doushantuo carbonates, South China: implications for the “snowball Earth” hypothesis. Earth Planet. Sci. Lett. 224, 387–398. https://doi.org/10.1016/j.epsl.2004.05.015.
Macouin, M., Ader, M., Moreau, M.-G., Poitou, C., Yang, Z., Sun, Z., 2012. Deciphering the impact of diagenesis overprint on negative $\delta^{13}C$ excursions using rock magnetism: Case study of Ediacaran carbonates, Yangjiaping section, South China. Earth Planet. Sci. Lett. 351–352, 281–294. https://doi.org/10.1016/j.epsl.2012.06.057.
Mason, R.A., 1987. Ion microprobe analysis of trace elements in calcite with an application to the cathodoluminescence zonation of limestone cements from the Lower Carboniferous of South Wales, U.K. Chem. Geol. 64, 209–224. https://doi.org/10.1016/0009-2541(87)90003-9.
McFadden, K.A., Huang, J., Chu, X., Jiang, G., Kaufman, A.J., Zhou, C., Yuan, X., Xiao, S., 2008. Pulsed oxidation and biological evolution in the Ediacaran Doushantuo Formation. Proc. Natl. Acad. Sci. 105, 3197–3202. https://doi.org/10.1073/pnas.0708336105.
McMurtry, G.M., 2009. Authigenic deposits. In: Steele, J.H., Thorpe, S.A., Turekian, K.K. (Eds.), Marine Chemistry & Geochemistry: A derivative of the Encyclopedia of Ocean Sciences, 2nd Edition. Elsevier, Oxford, pp. 325–335.
Meister, P., McKenzie, J.A., Vasconcelos, C., Bernasconi, S., Frank, M., Gutjahr, M., Schrag, D.P., 2007. Dolomite formation in the dynamic deep biosphere: results from the Peru Margin. Sedimentology 54, 1007–1032. https://doi.org/10.1111/j.1365-3091.2007.00870.x.
Melezhik, V., Fallick, A.E., Pokrovsky, B.G., 2005. Enigmatic nature of thick sedimentary carbonates depleted in ^{13}C beyond the canonical mantle value: the challenges to our understanding of the terrestrial carbon cycle. Precambr. Res. 137, 131–165. https://doi.org/10.1016/j.precamres.2005.03.010.
Melezhik, V.A., Fallick, A.E., 1996. A widespread positive $\delta^{13}C_{carb}$ anomaly at around 2.33–2.06 Ga on the Fennoscandian Shield: a paradox? Terra Nova 8, 141–157. https://doi.org/10.1111/j.1365-3121.1996.tb00738.x.
Melezhik, V.A., Pokrovsky, B.G., Fallick, A.E., Kuznetsov, A.B., Bujakaite, M.I., 2009. Constraints on $^{87}Sr/^{86}Sr$ of Late Ediacaran seawater: insight from Siberian high-Sr limestones. J. Geol. Soc. 166, 183–191. https://doi.org/10.1144/0016-76492007-171.
Melim, L.A., Westphal, H., Swart, P.K., Eberli, G.P., Munnecke, A., 2002. Questioning carbonate diagenetic paradigms: evidence from the Neogene of the Bahamas. Mar. Geol. 185, 27–53. https://doi.org/10.1016/S0025-3227(01)00289-4.
Minguez, D., Kodama, K.P., 2017. Rock magnetic chronostratigraphy of the Shuram carbon isotope excursion: Wonoka Formation, Australia. Geology 45, 567–570. https://doi.org/10.1130/g38572.1.
Moynihan, D.P., Strauss, J.V., Nelson, L.L., Padget, C.D., 2019. Upper Windermere Supergroup and the transition from rifting to continent-margin sedimentation, Nadaleen River area, northern Canadian Cordillera. Geol. Soc. Am. Bull. 131, 1673–1701. https://doi.org/10.1130/B32039.1.
Pagel, M., Barbin, V., Blanc, P., Ohnenstetter, D., 2000. Cathodoluminescence in Geosciences. Springer, Berlin, Heidelberg, XV, p. 514 pp..
Peng, Y., Jiang, G., Bao, H., Xiao, S., Kaufman, A.J., Zhou, C., Wang, J., 2015. Sulfate-driven anaerobic oxidation of methane as the origin of extremely ^{13}C-depleted calcite in the Doushantuo cap carbonates in South China. AGU Fall meeting, San Francisco, pp. B21A–B408.
Pierre, C., Blanc-Valleron, M.M., Caquineau, S., März, C., Ravelo, A.C., Takahashi, K., Alvarez Zarikian, C., 2016. Mineralogical, geochemical and isotopic characterization of authigenic carbonates from the methane-bearing sediments of the Bering Sea continental margin (IODP Expedition 323, Sites U1343–U1345). Deep Sea Res. Part II 125–126, 133–144. https://doi.org/10.1016/j.dsr2.2014.03.011.
Pokrovskii, B., Melezhik, V., Bujakaite, M., 2006. Carbon, oxygen, strontium, and sulfur isotopic compositions in late Precambrian rocks of the Patom Complex, central Siberia: Communication 1. results, isotope stratigraphy, and dating problems. Lithol. Min. Resour. 41, 450–474. https://doi.org/10.1134/s0024490206050063.
Pokrovsky, B.G., Bujakaite, M.I., 2015. Geochemistry of C, O, and Sr isotopes in the Neoproterozoic carbonates from the southwestern Patom paleobasin, southern

Middle Siberia. Lithol. Min. Resour. 50, 144–169. https://doi.org/10.1134/s0024490215010046.
Pokrovsky, B.G., Bujakaite, M.I., Kolesnikova, A.A., Petrov, O.L., Khlebnikov, M.S., 2021. C, O, and Sr Isotope Geochemistry of the Vendian Shuram-Wonoka Anomaly and Associated Metasedimentary Rocks in the Inner Part of the Patom Upland (Central Siberia). Lithol. Min. Resour. 56, 390–417. https://doi.org/10.1134/S0024490221050047.
Prave, A.R., Kirsimäe, K., Lepland, A., Fallick, A.E., Kreitsmann, T., Deines, Y.E., Romashkin, A.E., Rychanchik, D.V., Medvedev, P.V., Moussavou, M., Bakakas, K., Hodgskiss, M.S.W., 2022. The grandest of them all: the Lomagundi–Jatuli Event and Earth's oxygenation. J. Geol. Soc. 179, jgs2021-036. https://doi.org/10.1144/jgs2021-036.
Pu, J.P., Bowring, S.A., Ramezani, J., Myrow, P., Raub, T.D., Landing, E., Mills, A., Hodgin, E., Macdonald, F.A., 2016. Dodging snowballs: Geochronology of the Gaskiers glaciation and the first appearance of the Ediacaran biota. Geology 44, 955–958. https://doi.org/10.1130/g38284.1.
Rooney, A.D., Strauss, J.V., Brandon, A.D., Macdonald, F.A., 2015. A Cryogenian chronology: Two long-lasting synchronous Neoproterozoic glaciations. Geology 43, 459–462. https://doi.org/10.1130/g36511.1.
Rooney, A.D., Cantine, M.D., Bergmann, K.D., Gómez-Pérez, I., Al Baloushi, B., Boag, T. H., Busch, J.F., Sperling, E.A., Strauss, J.V., 2020. Calibrating the coevolution of Ediacaran life and environment. Proc. Natl. Acad. Sci. 117, 16824–16830. https://doi.org/10.1073/pnas.2002918117.
Rose, C.V., Fischer, W.W., Finnegan, S., Fike, D.A., 2019. Records of carbon and sulfur cycling during the Silurian Ireviken Event in Gotland, Sweden. Geochim. Cosmochim. Acta 246, 299–316. https://doi.org/10.1016/j.gca.2018.11.030.
Rothman, D.H., Hayes, J.M., Summons, R.E., 2003. Dynamics of the Neoproterozoic carbon cycle. Proc. Natl. Acad. Sci. 100, 8124–8129. https://doi.org/10.1073/pnas.0832439100.
Saltzman, M.R., Thomas, E., 2012. Carbon isotope stratigraphy. In: Gradstein, F.M., Ogg, J.G., Schmitz, M.D., Ogg, G.M. (Eds.), The Geologic Time Scale. Elsevier, Boston, USA, pp. 207–232. https://doi.org/10.1016/b978-0-444-59425-9.00011-1.
Sawaki, Y., Ohno, T., Tahata, M., Komiya, T., Hirata, T., Maruyama, S., Windley, B.F., Han, J., Shu, D., Li, Y., 2010. The Ediacaran radiogenic Sr isotope excursion in the Doushantuo Formation in the Three Gorges area, South China. Precambr. Res. 176, 46–64. https://doi.org/10.1016/j.precamres.2009.10.006.
Scheller, E.L., Grotzinger, J., Ingalls, M., 2021. Guttulatic calcite: A carbonate microtexture that reveals frigid formation conditions. Geology 50, 48–53. https://doi.org/10.1130/g49312.1.
Schindelin, J., Arganda-Carreras, I., Frise, E., Kaynig, V., Longair, M., Pietzsch, T., Preibisch, S., Rueden, C., Saalfeld, S., Schmid, B., 2012. Fiji: an open-source platform for biological-image analysis. Nat. Methods 9, 676–682. https://doi.org/10.1038/nmeth.1985.
Schmitz, M.D., 2012. Radiometric ages used in GTS2012. In: Gradstein, F.M., Ogg, J.G., Schmitz, M.D., Ogg, G.M. (Eds.), The Geologic Time Scale. Elsevier, Boston, pp. 1045–1082. https://doi.org/10.1016/b978-0-444-59425-9.15002-4.
Scholle, P.A., Arthur, M.A., 1980. Carbon isotope fluctuations in Cretaceous pelagic limestones: potential stratigraphic and petroleum exploration tool. AAPG Bull. 64, 67–87. https://doi.org/10.1306/2F91892D-16CE-11D7-8645000102C1865D.
Schrag, D.P., Higgins, J.A., Macdonald, F.A., Johnston, D.T., 2013. Authigenic carbonate and the history of the global carbon cycle. Science 339, 540–543. https://doi.org/10.1126/science.1229578.
Shi, W., Li, C., Luo, G., Huang, J., Algeo, T.J., Jin, C., Zhang, Z., Cheng, M., 2018. Sulfur isotope evidence for transient marine-shelf oxidation during the Ediacaran Shuram Excursion. Geology 46, 267–270. https://doi.org/10.1130/g39663.1.
Shields, G., 1997. A widespread positive $\delta^{13}C$ anomaly at around 2.33–2.06 Ga on the Fennoscandian Shield—Comment and Reply: Paradox lost? Terra Nova 9, 148–151. https://doi.org/10.1046/j.1365-3121.1997.d01-76.x.
Shields, G., Stille, P., Brasier, M.D., Atudorei, N.V., 1997. Stratified oceans and oxygenation of the late Precambrian environment: a post glacial geochemical record from the Neoproterozoic of W. Mongolia. Terra Nova 9, 218–222. https://doi.org/10.1111/j.1365-3121.1997.tb00016.x.
Shields, G.A., Mills, B.J.W., Zhu, M., Raub, T.D., Daines, S.J., Lenton, T.M., 2019. Unique Neoproterozoic carbon isotope excursions sustained by coupled evaporite dissolution and pyrite burial. Nat. Geosci. 12, 823–827. https://doi.org/10.1038/s41561-019-0434-3.
Śliwiński, M.G., Kitajima, K., Kozdon, R., Spicuzza, M.J., Fournelle, J.H., Denny, A., Valley, J.W., 2016a. Secondary ion mass spectrometry bias on isotope ratios in dolomite–ankerite, Part II: $\delta^{13}C$ matrix effects. Geostand. Geoanal. Res. 40, 173–184. https://doi.org/10.1111/j.1751-908X.2015.00380.x.
Śliwiński, M.G., Kozdon, R., Kitajima, K., Valley, J.W., Denny, A., 2016b. Microanalysis of carbonate cement $\delta^{18}O$ in a CO_2-storage system seal: insights into the diagenetic history of the Eau Claire Formation (Upper Cambrian) Illinois Basin. AAPG Bulletin 1003–1031. https://doi.org/10.1306/02031615065.
Śliwiński, M.G., Kitajima, K., Kozdon, R., Spicuzza, M.J., Denny, A., Valley, J.W., 2017. In situ $\delta^{13}C$ and $\delta^{18}O$ microanalysis by SIMS: A method for characterizing the carbonate components of natural and engineered CO2-reservoirs. Int. J. Greenhouse Gas Control 57, 116–133. https://doi.org/10.1016/j.ijggc.2016.12.013.
Sommer, S.E., 1972. Cathodoluminescence of carbonates, 1. Characterization of cathodoluminescence from carbonate solid solutions. Chem. Geol. 9, 257–273. https://doi.org/10.1016/0009-2541(72)90064-2.
Sui, Y., Huang, C., Zhang, R., Wang, Z., Ogg, J., 2019. Astronomical time scale for the middle-upper Doushantuo Formation of Ediacaran in South China: Implications for the duration of the Shuram/Wonoka negative $\delta^{13}C$ excursion. Palaeogeogr. Palaeoclimatol. Palaeoecol. 532, 109273 https://doi.org/10.1016/j.palaeo.2019.109273.
Summons, R.E., Hayes, J.M., 1992. Principles of Molecular and Isotopic Biogeochemistry. In: Schopf, J.W., Klein, C. (Eds.), The Proterozoic Biosphere: A Multidisciplinary Study. Cambridge University Press, Cambridge, pp. 83–93.
Tahata, M., Ueno, Y., Ishikawa, T., Sawaki, Y., Murakami, K., Han, J., Shu, D., Li, Y., Guo, J., Yoshida, N., Komiya, T., 2013. Carbon and oxygen isotope chemostratigraphies of the Yangtze platform, South China: Decoding temperature and environmental changes through the Ediacaran. Gondwana Res. 23, 333–353. https://doi.org/10.1016/j.gr.2012.04.005.
Talbot, M., Kelts, K., 1986. Primary and diagenetic carbonates in the anoxic sediments of Lake Bosumtwi, Ghana. Geology 14, 912–916. https://doi.org/10.1130/0091-7613(1986)14<912:padcit>2.0.co;2.
Tang, Q., Cui, H., Zhang, F., 2022. Neoproterozoic Earth-life system. Precambr. Res. 368, 106486 https://doi.org/10.1016/j.precamres.2021.106486.
Tucker, M.E., 1982. Precambrian dolomites: petrographic and isotopic evidence that they differ from Phanerozoic dolomites. Geology 10, 7–12. https://doi.org/10.1130/0091-7613(1982)10<7:PDPAIE>2.0.CO;2.
Valley, J.W., Kita, N.T., 2009. *In situ* oxygen isotope geochemistry by ion microprobe. In: Fayek, M. (Ed.), Secondary Ion Mass Spectrometry in the Earth Sciences – Gleaning the Big Picture from a Small Spot. Mineralogical Association of Canada Short Course 41, Toronto, pp. 19–63.
Veizer, J., Holser, W.T., Wilgus, C.K., 1980. Correlation of $^{13}C/^{12}C$ and $^{34}S/^{32}S$ secular variations. Geochim. Cosmochim. Acta 44, 579–587. https://doi.org/10.1016/0016-7037(80)90250-1.
Wallmann, K., Aloisi, G., 2012. The Global Carbon Cycle: Geological Processes. In: Knoll, A.H., Canfield, D.E., Konhauser, K.O. (Eds.), Fundamentals of Geobiology. Blackwell Publishing Ltd, Hoboken, New Jersey, USA, pp. 20–35. https://doi.org/10.1002/9781118280874.ch3.
Wang, J., Jiang, G., Xiao, S., Li, Q., Wei, Q., 2008. Carbon isotope evidence for widespread methane seeps in the ca. 635 Ma Doushantuo cap carbonate in south China. Geology 36, 347–350. https://doi.org/10.1130/g24513a.1.
Wang, W., Zhou, C., Yuan, X., Chen, Z., Xiao, S., 2012. A pronounced negative $\delta^{13}C$ excursion in an Ediacaran succession of western Yangtze Platform: A possible equivalent to the Shuram event and its implication for chemostratigraphic correlation in South China. Gondwana Res. 22, 1091–1101. https://doi.org/10.1016/j.gr.2012.02.017.
Wang, W., Guan, C., Zhou, C., Peng, Y., Pratt, L.M., Chen, X., Chen, L., Chen, Z., Yuan, X., Xiao, S., 2017a. Integrated carbon, sulfur, and nitrogen isotope chemostratigraphy of the Ediacaran Lantian Formation in South China: Spatial gradient, ocean redox oscillation, and fossil distribution. Geobiology 15, 552–571. https://doi.org/10.1111/gbi.12226.
Wang, W., Guan, C., Hu, Y., Cui, H., Muscente, A.D., Chen, L., Zhou, C., 2020. Spatial and temporal evolution of Ediacaran carbon and sulfur cycles in the Lower Yangtze Block, South China. Palaeogeogr. Palaeoclimatol. Palaeoecol. 537, 109417 https://doi.org/10.1016/j.palaeo.2019.109417.
Wang, X., Shi, X., Jiang, G., Tang, D., 2014. Organic carbon isotope gradient and ocean stratification across the late Ediacaran-Early Cambrian Yangtze Platform. Sci. China Earth Sci. 57, 919–929. https://doi.org/10.1007/s11430-013-4732-0.
Wang, X., Jiang, G., Shi, X., Xiao, S., 2016. Paired carbonate and organic carbon isotope variations of the Ediacaran Doushantuo Formation from an upper slope section at Siduping, South China. Precambr. Res. 273, 53–66. https://doi.org/10.1016/j.precamres.2015.12.010.
Wang, Z., Wang, J., Kouketsu, Y., Bodnar, R.J., Gill, B.C., Xiao, S., 2017b. Raman geothermometry of carbonaceous material in the basal Ediacaran Doushantuo cap dolostone: The thermal history of extremely negative $\delta^{13}C$ signatures in the aftermath of the terminal Cryogenian snowball Earth glaciation. Precambr. Res. 298, 174–186. https://doi.org/10.1016/j.precamres.2017.06.013.
Warren, J.K., 2016. Interpreting Evaporite Textures. In: Warren, J.K. (Ed.), Evaporites: A Geological Compendium. Springer International Publishing, Cham, pp. 1–83. https://doi.org/10.1007/978-3-319-13512-0_1.
Wei, W., Frei, R., Gilleaudeau, G.J., Li, D., Wei, G.-Y., Chen, X., Ling, H.-F., 2018. Oxygenation variations in the atmosphere and shallow seawaters of the Yangtze Platform during the Ediacaran Period: Clues from Cr-isotope and Ce-anomaly in carbonates. Precambr. Res. 313, 78–90. https://doi.org/10.1016/j.precamres.2018.05.009.
Wood, R.A., Poulton, S.W., Prave, A.R., Hoffmann, K.H., Clarkson, M.O., Guilbaud, R., Lyne, J.W., Tostevin, R., Bowyer, F., Penny, A.M., Curtis, A., Kasemann, S.A., 2015. Dynamic redox conditions control late Ediacaran metazoan ecosystems in the Nama Group, Namibia. Precambr. Res. 261, 252–271. https://doi.org/10.1016/j.precamres.2015.02.004.
Xiao, S., McFadden, K.A., Peek, S., Kaufman, A.J., Zhou, C., Jiang, G., Hu, J., 2012. Integrated chemostratigraphy of the Doushantuo Formation at the northern Xiaofenghe section (Yangtze Gorges, South China) and its implication for Ediacaran stratigraphic correlation and ocean redox models. Precambr. Res. 192–195, 125–141. https://doi.org/10.1016/j.precamres.2011.10.021.
Xiao, S., Narbonne, G.M., Zhou, C., Laflamme, M., Grazhdankin, D.V., Moczydłowska-Vidal, M., Cui, H., 2016. Toward an Ediacaran time scale: Problems, protocols, and prospects. Episodes, 39, 540–555. https://doi.org/10.18814/epiiugs/2016/v39i4/103886.
Xiao, S., Cui, H., Kang, J., McFadden, K.A., Kaufman, A.J., Kitajima, K., Fournelle, J.H., Schwid, M., Nolan, M., Baele, J.-M., Valley, J.W., 2020. Using SIMS to decode noisy stratigraphic $\delta^{13}C$ variations in Ediacaran carbonates. Precambr. Res. 343, 105686 https://doi.org/10.1016/j.precamres.2020.105686.
Xiao, S., Narbonne, G.M., 2020. The Ediacaran Period. In: Gradstein, F.M., Ogg, J.G., Schmitz, M.D., Ogg, G.M. (Eds.), Geologic Time Scale 2020. Elsevier, pp. 521–561. https://doi.org/10.1016/B978-0-12-824360-2.00018-8.

Yang, C., Rooney, A.D., Condon, D.J., Li, X.-H., Grazhdankin, D.V., Bowyer, F.T., Hu, C., Macdonald, F.A., Zhu, M., 2021. The tempo of Ediacaran evolution. Science. Advances 7, eabi9643. https://doi.org/10.1126/sciadv.abi9643.

Zhang, F., Xiao, S., Romaniello, S.J., Hardisty, D., Li, C., Melezhik, V., Pokrovsky, B., Cheng, M., Shi, W., Lenton, T.M., Anbar, A.D., 2019. Global marine redox changes drove the rise and fall of the Ediacara biota. Geobiology 17, 594–610. https://doi.org/10.1111/gbi.12359.

Zhang, Z., Zhu, G., Wu, G., Li, T., Feng, X., Jing, Y., 2022. Carbon isotopic chemostratigraphy of the Ediacaran-Cambrian successions in the northwestern Tarim Craton, NW China: Correlations with Gondwana supercontinent. Global Planet. Change 208, 103702. https://doi.org/10.1016/j.gloplacha.2021.103702.

Zhao, M., Planavsky, N., Oehlert, A.M., Wei, G., Gong, Z., 2020. Simulating meteoric and mixing zone carbonate diagenesis with a two-dimensional reactive transport model. Am. J. Sci. 320, 599–636. https://doi.org/10.2475/09.2020.02.

Zhou, C., Xiao, S., 2007. Ediacaran $\delta^{13}C$ chemostratigraphy of South China. Chem. Geol. 237, 89–108. https://doi.org/10.1016/j.chemgeo.2006.06.021.

Zhou, C., Jiang, S., Xiao, S., Chen, Z., Yuan, X., 2012. Rare earth elements and carbon isotope geochemistry of the Doushantuo Formation in South China: Implication for middle Ediacaran shallow marine redox conditions. Chin. Sci. Bull. 57, 1998–2006. https://doi.org/10.1007/s11434-012-5082-6.

Zhou, C., Guan, C., Cui, H., Ouyang, Q., Wang, W., 2016. Methane-derived authigenic carbonate from the lower Doushantuo Formation of South China: Implications for seawater sulfate concentration and global carbon cycle in the early Ediacaran ocean. Palaeogeogr. Palaeoclimatol. Palaeoecol. 461, 145–155. https://doi.org/10.1016/j.palaeo.2016.08.017.

Zhou, C., Xiao, S., Wang, W., Guan, C., Ouyang, Q., Chen, Z., 2017. The stratigraphic complexity of the middle Ediacaran carbon isotopic record in the Yangtze Gorges area, South China, and its implications for the age and chemostratigraphic significance of the Shuram excursion. Precambr. Res. 288, 23–38. https://doi.org/10.1016/j.precamres.2016.11.007.

Zhu, M., Strauss, H., Shields, G.A., 2007a. From snowball earth to the Cambrian bioradiation: calibration of Ediacaran-Cambrian earth history in South China. Palaeogeogr. Palaeoclimatol. Palaeoecol. 254, 1–6. https://doi.org/10.1016/j.palaeo.2007.03.026.

Zhu, M., Zhang, J., Yang, A., 2007b. Integrated Ediacaran (Sinian) chronostratigraphy of South China. Palaeogeogr. Palaeoclimatol. Palaeoecol. 254, 7–61. https://doi.org/10.1016/j.palaeo.2007.03.025.

Zhu, M., Lu, M., Zhang, J., Zhao, F., Li, G., Yang, A., Zhao, X., Zhao, M., 2013. Carbon isotope chemostratigraphy and sedimentary facies evolution of the Ediacaran Doushantuo Formation in western Hubei, South China. Precamb. Res. 225, 7–28. https://doi.org/10.1016/j.precamres.2011.07.019.

Zhu, M., Zhang, J., Yang, A., Li, G., Zhao, F., Lu, M., Yin, Z., Miao, L., Hu, C., 2022. Chapter 5 Neoproterozoic stratigraphy, depositional environments & hydrocarbon source-reservoir-seal bed assemblage in South China. In: Sun, S., Wang, T.-G. (Eds.), Meso-Neoproterozoic Geology and Petroleum Resources. Springer & Science Press, pp. In press.